Development and application of advanced Hyperspectral and Multispectral Imaging Systems for non-invasive diagnostic and surgical interventions

Marta Marradi

A thesis submitted for the degree of

Doctor of Philosophy

of

European Laboratory for Non-Linear Spectroscopy

and

Department of Physics and Astronomy

University of Florence

XXXVII Cycle

Abstract

This thesis presents the development and application of two advanced optical diagnostic tools, each designed for distinct but complementary purposes in the field of medical imaging and diagnostics. The first research line introduces a novel hyperspectral imaging device, HyperProbe1, which leverages rapid spectral scanning through a combination of supercontinuum laser illumination and acousto-optic tunable filter technology. HyperProbe1 is capable of sequentially scanning up to 79 wavelengths within the 510 to 900 nm range, achieving high spectral and spatial resolution within a short time frame of under five minutes for a full scan. This device has been utilized to perform a preliminary analysis on fresh surgical glioma samples of varying severity. The findings indicate that HyperProbe1 can effectively differentiate between lower-grade and higher-grade gliomas by quantifying chromophore concentrations, such as hemoglobin and cytochrome-c-oxidase, as well as lipid content. Notably, differences in lipid content and cytochrome-c-oxidase concentrations were observed between low grade and high grade gliomas, suggesting potential metabolic and structural differences that could be leveraged for tumor classification. Furthermore, HyperProbe1 demonstrates potential for rapid, non-destructive histological analysis, providing a faster alternative to traditional histopathological methods. This technology also holds promise for future applications in *in situ* surgical settings and as a neuronavigational tool in brain surgery, offering a real-time, optical approach to enhance surgical outcomes and patient prognosis.

The second research line focuses on the development of the MultiSmart multispectral imaging device, designed for non-invasive monitoring and characterization of chronic skin ulcers. MultiSmart utilizes a combination of Light Emitting Diodes and a Complementary Metal-Oxide-Semiconductor camera to capture tissue images across selected visible to near-infrared spectral bands, targeting key wavelengths that reveal physiological changes related to oxygenation and hemodynamics. The device's calibration, performed with liquid optical phantoms, enables the creation of look-up tables for quantitative analysis of blood volume fraction and oxygen saturation in tissue images. Preliminary results have

demonstrated the device's capability to detect variations in blood volume fraction and saturation levels, identifying areas of abnormal blood accumulation and deoxygenated regions, thereby assessing wound severity and healing progression. Future enhancements to the MultiSmart system aim to include real-time data processing and the detection of additional biomarkers, expanding its diagnostic capabilities. These developments could significantly improve its utility in clinical settings for monitoring and treating skin ulcers.

Together, these research lines underscore the potential of advanced hyperspectral and multispectral imaging technologies to revolutionize medical diagnostics by providing rapid, accurate, and non-invasive tools for tissue characterization and monitoring. They represent significant steps toward the integration of optical imaging technologies in clinical practice, with broad implications for patient care and treatment outcomes.

Contents

Chapter 1: Introduction to Hyperspectral and Multispectral Imaging 1

1.1 Current state of the art 2

1.2 Aim of the thesis 4

1.3 Outline of the thesis 5

1.4 Background 6

1.4.1 Light absorption 6

1.4.2 Light Scattering 8

1.4.2.1 The Modified Beer-Lambert Law 9

1.4.3 Light reflection and refraction 11

1.4.4 Fluorescence 12

Chapter 2: High density Hyperspectral Imaging 14

2.1 Overview of cerebral gliomas, glioblastomas and current examination methods 14

2.2 Human brain optical spectroscopy and imaging 16

2.2.1 Near-infrared spectroscopy for brain monitoring 17

2.2.1.1 Continuous-Wave NIRS 17

2.2.1.2 Frequency-Domain NIRS 18

2.2.1.3 Time-Domain NIRS 18

2.2.2 Diffuse Optical Tomography 19

2.2.3 Hyperspectral Imaging 20

2.3 Operation principles of hyperspectral imaging systems 22

2.3.1 Spectral scanning mode 22

2.3.2 Spatial scanning mode 23

2.3.3 Snapshot mode 23

2.4 *HyperProbe1*: a novel HSI system designed for the analysis of glioma biopsies 24

2.4.1 Description of HyperProbe1 25

2.4.2 Spectral and power characterization 27

2.4.2.1 Improving power output stability using amplitude stabilizers 31

2.4.3 Imaging characterization 33

2.4.3.1 Spatial resolution 33

2.4.3.2 Image contrast and SNR 35

2.4.3.3 Field of view 37

2.4.3.4 Assessment of image aberrations and distortions 38
2.4.4 Temporal resolution of HyperProbe1 38
2.4.5 Summary of the main technical characteristics of HyperProbe1 39
2.4.6 Hyperspectral data acquisition via GUI 40
2.5 Analysis of glioma biopsies with HyperProbe 41
2.5.1 Description of the specimen 42
2.5.2 Manipulation of the specimen and data acquisition protocol 43
2.6 Data processing and spectral unmixing 44
2.6.1 Data processing for reflectance hyperspectral data 45
2.6.2 Spectral unmixing analysis 45
2.7 Results of the analysis of glioma biopsies 47
2.7.1 Qualitative and comparative evaluation of the HyperProbe1 data 47
2.7.2 Quantitative biochemical analysis of the HyperProbe1 data with spectral unmixing 52
2.8 Conclusion and summary of the HyperProbe project 56
Chapter 3: Multispectral Imaging 60
3.1 Multispectral imaging for chronic skin ulcers 60
3.2 MultiSmart: a novel MSI system for chronic skin ulcer monitoring 64
3.2.1 Description of MultiSmart 65
3.2.2 Selection of wavelengths for wound healing monitoring and spectral - power characterization 66
3.2.3 Imaging characterization 68
3.2.3.1 Field of view 69
3.2.3.2 Spatial resolution 69
3.2.3.3 Image contrast and SNR 70
3.2.4 Acquisition times of MultiSmart 71
3.2.5 Summary of the main technical characteristics of MultiSmart 72
3.3 Calibration of MultiSmart with liquid blood optical phantoms 72
3.3.1 Description of the optical liquid phantoms and data collection 73
3.3.2 Data processing for the phantom datasets 76
3.3.3 Construction of Look Up Tables 77
3.4 Analysis and study of *in-vivo* chronic ulcers and skin lesions 78
3.4.1 Acquisition and image processing of patient datasets 78
3.4.2 Development of a script for the analysis of skin lesions using the LUTs 79
3.5 Results of the analysis of skin lesions using MultiSmart 81

3.6 Conclusions and summary of the MultiSmart project 83
References ..... **Errore. Il segnalibro non è definito.**
Chapter 4: Conclusions and future outcomes 86
Appendix 88
References 91

List of Acronyms

5-ALA - 5-Aminolevulinic Acid

ABI - Ankle-Brachial Index

AOTF - Acousto-Optic Tunable Filter

BVF - Blood Volume Fraction

CCO - Cytochrome-c-oxidase

CNS - Central Nervous System

CMOS - Complementary Metal-Oxide Semiconductor

CW-NIRS - Continuous-Wave Near-Infrared Spectroscopy

diffCCO - Differential Cytochrome-c-oxidase

DOT - Diffuse Optical Tomography

FD-NIRS - Frequency-Domain Near-Infrared Spectroscopy

FGS - Fluorescence-Guided Surgery

FOV - Field of View

FWHM - Full-Width at Half Maximum

GBM - Glioblastoma Multiforme

GUI - Graphical User Interface

H&E - Hematoxylin and Eosin

HbO2 - Oxyhemoglobin

HbT - Total Hemoglobin (sum of Oxyhemoglobin and Deoxyhemoglobin)

HHb - Deoxygenated Hemoglobin

HGG - Higher-Grade Glioma

HSI - Hyperspectral Imaging

IDH - Isocitrate Dehydrogenase

IL - Intralipid

LED - Light Emitting Diode

LGG - Lower-Grade Glioma

LUT - Look-Up Table

MBLL - Modified Beer-Lambert Law

MLP - Multi-Layer Perceptron

MSI - Multispectral Imaging

NADH - Nicotinamide Adenine Dinucleotide (Reduced Form)

NIR - Near-Infrared

NIRS - Near-Infrared Spectroscopy

OCT - Optical Coherence Tomography

PBS - Phosphate-Buffered Saline

QE - Quantum Efficiency

RGB - Red-Green-Blue (color model)

RMSE - Root Mean Square Error

ROI - Region of Interest

sCMOS - Scientific Complementary Metal-Oxide Semiconductor

SCL - Supercontinuum Laser

SFDI - Spatial Frequency Domain Imaging

sO2 - Saturation (Oxygen Saturation)

SNR - Signal-to-Noise Ratio

TcPO2 - Transcutaneous Oxygen Partial Pressure

TD-NIRS - Time-Domain Near-Infrared Spectroscopy

VI - Virtual Interface

WHO - World Health Organization

Chapter 1: Introduction to Hyperspectral and Multispectral Imaging

Hyperspectral and multispectral imaging are advanced optical technologies that capture and analyze information from across the electromagnetic spectrum. Unlike traditional imaging methods, which capture images in three broad spectral bands (red, green, and blue), hyperspectral and multispectral imaging divide the spectrum into many more narrow wavelength bands, providing detailed spectral information for each pixel in an image. This capability enables the identification and characterization of materials, objects, and processes that are not discernible with conventional imaging techniques. Hyperspectral Imaging (HSI) involves capturing images across a large number of narrow, contiguous spectral bands. The resulting data contains spatial and spectral information for each pixel. This allows for the detailed analysis of the spectral properties of the objects in the scene, facilitating the identification of materials based on their spectral signatures. On the other hand, Multispectral Imaging (MSI) captures images in a smaller number of broader spectral bands compared to HSI. While MSI does not provide the same level of spectral detail as HSI, it offers a balance between spectral resolution and data volume, making it suitable for a wide range of applications.

HSI and MSI have a wide range of applications, including agriculture [1,2], environmental monitoring, mineralogy, geology [3–7], surveillance and security [8], art and cultural heritage [9,10], food quality control [11], and most importantly, medical imaging [12], which will be the primary focus of this thesis.

Current market studies indicate emerging demands for biomedical diagnostics [13]. Both HSI and MSI offer significant advantages in the medical field by providing detailed spectral information that enhances the detection, diagnosis, and monitoring of various conditions. HSI, with its high spectral resolution, is particularly valuable for applications requiring precise tissue characterization, while MSI, with its broader bands, offers practical solutions for real-time imaging and less complex diagnostic needs. These technologies are paving the way for more accurate, non-invasive medical diagnostics and improved patient care. For this reason, it is

anticipated that they will significantly contribute to noninvasive disease diagnosis and monitoring, the identification and quantitative analysis of cancer biomarkers, image-guided minimally invasive surgery, targeted drug delivery and tracking, and pharmaceutical drug dosage assessment [12]. In fact, many diseases are still challenging to diagnose and could benefit from HSI and MSI, but further research, development and validation are required [13].

In this work, two different lines of technological development and application are presented, as part of a broader thesis project: (1) the development of a HSI system for the rapid biochemical analysis of fresh brain tumor (glioma) biopsies and (2) the development of a MSI system for chronic skin ulcer monitoring. The development of a HSI system for the analysis of glioma biopsies and the subsequent application of a MSI system for chronic skin ulcer monitoring both embody the strategic utilization of spectral data to address critical healthcare challenges. HSI, with its extensive range of spectral bands, enables the detailed differentiation among various grades of glioma by capturing subtle biochemical and structural differences in the tissue samples. This detailed spectral information is crucial for precise tumor characterization and subsequent treatment planning [12]. On the other hand, MSI offers a practical and efficient solution for the continuous monitoring of chronic skin ulcers, facilitating timely interventions and better management of wound healing processes [14]. The connection between these lines lies in their shared goal of improving clinical outcomes through potentially non-invasive, real-time imaging modalities that enhance the diagnostic and monitoring capabilities in their respective applications, which is the final aim of the project. Both systems exemplify how spectral imaging can be tailored to meet specific clinical needs, demonstrating the versatility and transformative potential of these technologies in diverse medical fields.

1.1 Current state of the art

Surgical intervention is pivotal for treating malignant brain tumors, as complete resection significantly enhances patient prognosis. During surgery, tissue samples are rapidly analyzed intraoperatively to provide immediate feedback to the surgeon, a process taking about 30-45 minutes [15]. This quick assessment helps to confirm the presence of tumor tissue and guides further resection efforts. However, full

pathological evaluations, which can take several days or weeks, offer more detailed insights but are impractical intraoperatively due to time constraints [15]. The rapid intraoperative analysis of fresh sections is essential for making real-time decisions, although its turnaround time limits the feasibility of repeated biopsies within a single surgery [15]. In this context, the scientific community is working on the development of alternative approaches, such as HSI, that can potentially provide faster and more precise results. This imaging technology is becoming a valuable tool for both the *ex-vivo* [16–18] and *in-vivo* classification of brain tumors, as well as for use as an intraoperative image-guided technique [15,18–21]. Recent advancements in HSI technology for this field have focused on enhancing spatial resolution, spectral range, and data processing algorithms to improve the diagnostic accuracy and clinical applicability of the technique. Researchers have developed sophisticated methods, such as machine learning algorithms and deep learning approaches, to analyze the vast amount of data generated by HSI, enabling the automated classification of tumor tissues with high sensitivity and specificity [17,18,20–22]. Integrating HSI with artificial intelligence further refines tumor detection and classification, minimizing the reliance on time-consuming histopathological processes and enhancing the likelihood of achieving a precise tumor identification and classification, thereby improving patient survival rates and reducing recurrence.

Imaging techniques also play a crucial role in evaluating wound healing. While the biopsy of wound tissues remains the gold standard for assessing tissue morphological changes, it involves invasive procedures [23]. Typically, this analysis includes staining tissue with hematoxylin and eosin and examining it under a light microscope [23]. Despite its accuracy, the biopsy process is both invasive and time-consuming [23]. This invasiveness has driven the advancement and adoption of noninvasive optical imaging techniques as alternatives for wound assessment. In this context, MSI has gained significant attention as a practical and efficient tool for this field. One of the key advantages of MSI in skin ulcer monitoring is its ability to non-invasively assess the wound bed and surrounding tissues, providing valuable information that can guide treatment decisions and track healing progress over time. Clinical studies have shown that MSI can effectively differentiate between viable and non-viable tissues, track the saturation levels and blood content, and monitor

the effects of therapeutic interventions, thus improving patient outcomes [24–28]. Recent developments in MSI technology have focused on improving the spectral and spatial resolution, enhancing image acquisition speed, and developing portable and user-friendly devices that can be easily integrated into clinical workflows. Advanced image processing algorithms [24,25] and machine learning techniques [26] have been employed to analyze MSI data, providing automated and quantitative assessments of wound characteristics. Despite its potential, the widespread adoption of MSI in clinical practice faces several challenges. These include the need for standardized imaging protocols, difficulties in interpreting spectral data, the high cost and large size of imaging devices, and significant issues with motion errors during image acquisition. Motion artifacts are particularly problematic in *in-vivo* imaging, as patients often struggle to remain still during the acquisition process. To overcome these obstacles, efforts are being made to develop standardized guidelines, user-friendly software interfaces, cost-effective imaging solutions, and advanced image alignment software [29].

1.2 Aim of the thesis

The present work has two main objectives: (1) the development of a HSI system for the quantitative *ex-vivo* biochemical analysis of fresh glioma biopsies, and (2) the creation of a compact and portable MSI device for the *in-vivo* quantitative monitoring of chronic skin ulcers.

The first novel system aims to differentiate the severity of gliomas by quantifying the concentrations of key biomarkers, such as oxyhemoglobin (HbO_2), deoxyhemoglobin (HHb), cytochrome-c-oxidase (CCO), and lipids, without the need for tissue fixation, staining, or compromising tissue integrity. The steps undertaken in this work include:

- assembling the HSI system by coupling and aligning the selected hardware components and analyzing their technical performance;
- developing software for the interconnection of components and data collection;
- collecting datasets of glioma biopsies;

- creating algorithms for data processing, and qualitative/quantitative analysis.

The second device is designed to non-invasively and quantitatively monitor tissue oxygenation levels and blood concentration within the analyzed lesions. The development process follows this pipeline:

- assembling the hardware components and evaluating their optical and technical performance;
- calibrating the system using liquid optical phantoms based on fresh human blood;
- constructing lookup tables, using the blood phantom data, for the quantitative assessment of blood content and oxygen saturation;
- collecting datasets from patients affected by chronic skin lesions;
- developing a cross-check algorithm to analyze skin ulcer images using the lookup tables.

1.3 Outline of the thesis

The thesis is structured in three main chapters: Chapter 1 introduces the objective of this work, the state of the art in the relevant research areas and fundamental background notions necessary for understanding the subsequent chapters.

Chapter 2 focuses on the HSI project. It begins by addressing the challenges of brain tumors and the various optical imaging techniques used to assess them, with an emphasis on the functioning of HSI devices. The chapter then provides a detailed description of the novel HSI device and its technical performance. The final section presents the collected datasets, the analysis, and discusses the results.

Chapter 3 is dedicated to the MSI project. It starts by introducing the topic of chronic skin ulcers and proceeds with a description of the MSI device. The chapter then details the system's calibration process, including the liquid phantom experiments and the construction of lookup tables. It also explains the data collection, processing, and analysis of images from patients with chronic skin ulcers using a cross-check algorithm specifically developed to quantitatively correlate the

images with the lookup tables. The chapter concludes with a discussion of the obtained results.

Finally, Chapter 4 gives an overall summary of the most important results obtained for both the presented research lines and describes the future outcomes.

1.4 Background

The physics of biomedical optics revolves around how light interacts with biological tissues through absorption, scattering, reflection, refraction, and fluorescence. Understanding the nature of these interactions enables us to utilize them in a wide range of diagnostic and therapeutic technologies, enhancing our capacity to diagnose, monitor, and treat diseases more effectively. This chapter synthesizes the aforementioned concepts to provide a clearer understanding of the work presented in this thesis. Additionally, it also explains the basics of the Modified Beer-Lambert Law (MBLL), necessary for the HSI project.

1.4.1 Light absorption

Absorption in biological tissues occurs when the energy of photons is transferred to the tissue's molecules, leading to various photophysical and photochemical processes. The molecule is excited from the ground state to an excited one and the extent to which a medium absorbs light at a specific wavelength λ is determined by its absorption coefficient $\mu_a(\lambda)$. In summary, the absorption coefficient is a parameter that quantifies how much light (or other electromagnetic radiation) is absorbed per unit distance in a medium (cm^{-1}) [30]. It is a measure of the probability of absorption events occurring as light travels through a material. In the case of a medium consisting of several absorbers (chromophores), such as biological tissues, the total absorption coefficient is the sum of the individual absorption coefficients of each chromophore present in the medium [30]. Each chromophore has a characteristic absorption coefficient, as it depends on the wavelength of the incident light. Mathematically, it can be expressed as:

$$\mu_a(\lambda) = \sum_i \varepsilon_i(\lambda) C_i \tag{1.1}$$

where $\mu_a(\lambda)$ is the total absorption coefficient at wavelength λ, $\varepsilon_i(\lambda)$ is the molar absorption coefficient of the i-th chromophore at wavelength λ (formerly and still widely known as the 'extinction coefficient', expressed as M^{-1} cm^{-1}) and C_i is the concentration of the i-th chromophore in the medium [30]. This relationship assumes that the contributions of each chromophore to the total absorption are additive and independent of each other.

It is found empirically that the intensity $I(\lambda)$ of a collimated beam of light travelling through a medium of thickness l and with molar concentration C of the absorbing species varies in accord with the Beer–Lambert law [30]:

$$I(\lambda) = I_0(\lambda)10^{-\varepsilon(\lambda)Cl} \tag{1.2}$$

where I_0 is the intensity of the incident beam. To simplify 1.2, the absorbance A of the medium is introduced as [30]:

$$A = log\frac{I_0}{I} \tag{1.3}$$

By doing so, the Beer-Lambert Law becomes [30]:

$$A(\lambda) = \varepsilon(\lambda)Cl \tag{1.4}$$

In the case of multiple chromophores inside the medium, the additive property can be applied to the absorbance A under certain conditions: in a homogeneous solution, the Beer-Lambert Law states that the total absorbance A of a mixture is the sum of the absorbances of each individual component at a given wavelength λ:

$$A = \sum_i A_i = \sum_i \varepsilon_i(\lambda)C_i l \tag{1.5}$$

In biological tissues, the situation is more complex due to the heterogeneous and scattering nature of the tissues. However, the additive property can still be applied to a reasonable approximation under certain conditions:

- Homogeneous assumption: if the tissue can be approximated as a homogeneously mixed medium of different chromophores, the absorbance can be considered as the sum of the absorbances of the individual chromophores. This is often the basis for various spectroscopic techniques used in biomedical optics [30].
- Wavelength-specific absorption: the absorbance at a specific wavelength can be considered as the sum of the contributions from each chromophore, as long as the interactions between the chromophores do not significantly alter their individual absorption properties [30].
- Minimal scattering effects: the additive property is most accurate in situations where scattering effects are minimal or can be corrected [31]. Scattering in tissues (explained in **Sec. 1.4.2**) complicates the path length *l* and the effective absorption, which can deviate from the simple summation model [31]. Typically, light scattering in biological tissues is indeed significant, making the straightforward application of the Beer-Lambert Law more complex. The MBLL introduces a scattering term to account for this and will be described in **Sec. 1.4.2.1**.

In conclusion, while the additive property of absorbance can be applied to biological tissues, it requires careful consideration of the tissue's scattering properties and heterogeneity. With appropriate corrections and assumptions, it remains a useful tool for understanding and quantifying the interactions of light with biological tissues in various biomedical optical applications.

1.4.2 Light Scattering

Light scattering is a fundamental phenomenon that occurs when light waves encounter particles and are forced to deviate from their original trajectory. This interaction is crucial for understanding various natural and technological processes, including optical measurements and imaging techniques. The scattering of light can be broadly categorized into elastic and inelastic scattering, which differ based on whether the energy of the incident light is conserved [32].

In elastic scattering, the energy (and therefore the wavelength) of the scattered light remains the same as that of the incident light. This type of scattering includes Rayleigh scattering and Mie scattering, which are described by different theories based on the size of the scattering particles relative to the wavelength of the light [32]. Rayleigh scattering occurs when the particles causing the scattering are much smaller than the wavelength of the incident light. This type of scattering is characterized by its strong wavelength dependence, with the intensity I of scattered light being inversely proportional to the fourth power of the wavelength, mathematically expressed as $I \propto 1/\lambda^4$. Conversely, Mie scattering occurs when the scattering particles are comparable in size to the wavelength of the incident light. Unlike Rayleigh scattering, Mie scattering does not have a strong wavelength dependence, and the intensity of scattered light is more uniform across different wavelengths. This theory is used to describe scattering by larger particles, such as dust, water droplets, and aerosols.

In inelastic scattering, the energy of the scattered light is different from that of the incident light. This means that there is an exchange of energy between the light and the scattering medium [32].

In general, macroscopic media (including biological tissues) can be considered as composed of a random distribution of a multitude of scattering particles of various sizes and refractive indices. These particles interact with incoming light photons in a complex manner. When a light photon enters such a medium, it does not merely travel in a straight line. Instead, it undergoes a series of scattering events, where each interaction causes the photon to change direction. This series of deviations from its initial path due to sequential scattering events is not accounted for in the classical Beer-Lambert Law, as explained in the previous section. Therefore, the law is modified by incorporating correction factors that address these deviations, resulting in the MBLL (**Sec. 1.4.2.1**).

1.4.2.1 The Modified Beer-Lambert Law

As mentioned in the previous paragraphs, the MBLL takes into account several factors that can affect the accuracy of the classical Beer-Lambert Law. These modifications are necessary because real-world scenarios often involve deviations

due to chemical, physical, or instrumental reasons. The main factors considered in the MBLL include:

- Non-idealities in the absorption process: the presence of interactions between molecules, particularly at high concentrations, can cause deviations from the linearity predicted by the classical Beer-Lambert Law [33].
- Scattering and reflection losses: as mentioned in **Sec. 1.4.2**, light scattering and reflections (described in **Sec. 1.4.3**) can lead to additional losses that are not accounted for in the classical law [33].

Mathematically, the MBLL can be expressed as [34]:

$$log\frac{I(\lambda)}{I_0(\lambda)} = -\left[\sum_i C_i\mu_a^i(\lambda) + s\mu_s(\lambda)\right]\cdot l + U \tag{1.6}$$

In 1.6, $I_0(\lambda)$ represent the intensity of the incident light and $I(\lambda)$ the intensity of the light collected by the detector, meanwhile μ_a and μ_s correspond to the absorption and scattering coefficients, respectively. The subscript i identifies the molecules that are contained in the tissue, for example water, fat and hemoglobin, while C_i indicates their respective concentrations. The parameter s signifies the proportion of scattering in the overall dissipation of light energy, and l is the depth to which the light penetrates. U encompasses other physical factors affecting the dissipation of incoming light energy, such as autofluorescence or additional optical signals detected by the cameras, like ambient illumination.

When monitoring optical changes over time, it can be assumed that the factors contributing to U remain relatively stable, such as ambient illumination, which is often consistent [34]. This assumption holds because these effects typically fluctuate less significantly than the overall absorption [34], and can be utilized to cancel out or reduce the extent of the factor U of 1.6 by subtracting two detected spectra I_1 and I_2:

$$log\frac{I_2(\lambda)}{I_1(\lambda)} = -\left[\sum_i \delta C_i\mu_a^i(\lambda) + \delta(s\mu_s(\lambda))\right]\cdot l + \delta U \tag{1.7}$$

1.7 can be used to compare real measured spectra with those predicted with the MBLL. Typically, standard least-squares algorithms are employed to minimize the discrepancy between the two spectra, thereby extracting the molecular concentrations of the species and the scattering properties of the tissue [34].

1.4.3 Light reflection and refraction

Refraction and reflection describe the behavior of light when it encounters a distinct boundary between two different media, each characterized by its own refractive index n. The refractive index of a medium is a measure of how much the speed of light is reduced within that medium compared to its speed in vacuum. When a ray of light approaches this interface at an angle, part of the light can be reflected back into the original medium, and the remaining part is transmitted into the second medium, changing direction in the process [35].

Reflection occurs according to the principle that the angle of incidence (the angle between the incoming ray and a perpendicular to the surface at the point of incidence) equals the angle of reflection (the angle between the reflected ray and the same perpendicular) [35]. This principle is derived from the law of reflection, which states that the incident ray, the reflected ray, and the normal to the surface all lie in the same plane (**Fig. 1.1**).

Refraction is governed by Snell's Law, which relates the angles of incidence and refraction to the refractive indices of the two media. Mathematically, Snell's Law is expressed as:

$$n_1 sin\theta_1 = n_2 sin\theta_2 \quad (1.8)$$

where n_1 and n_2 are the refractive indices of the first and second media, respectively, and θ_1 and θ_2 are the angles of incidence and refraction [35]. When light passes from a medium with a lower refractive index to one with a higher refractive index, it bends towards the normal. Conversely, when it passes from a higher to a lower refractive index medium, it bends away from the normal (**Fig. 1.1**).

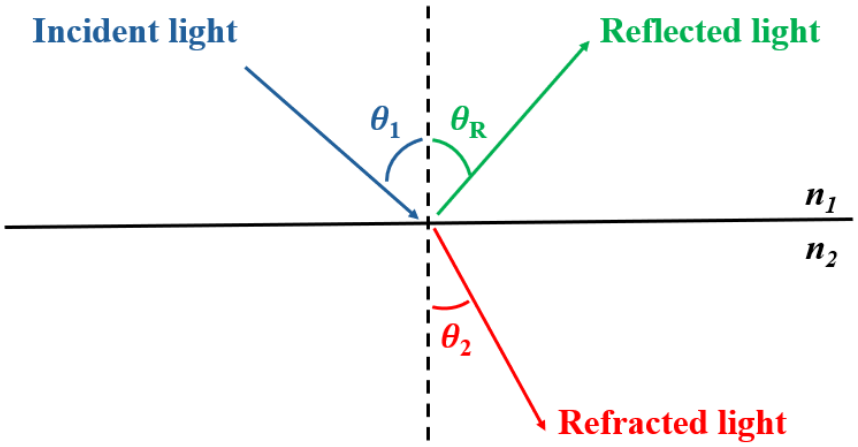

Fig. 1.1: Scheme of an incident light beam interacting with an interface dividing two mediums with different refractive indexes. The ray can either be reflected, in which case the angle of incidence θ_1 is equal to the angle of the reflected beam θ_R, or refracted with an angle θ_2 different from θ_1.

The phenomena of reflection and refraction are crucial for a variety of optical applications and technologies. Lenses, for instance, use refraction to focus light and form images in devices ranging from simple magnifying glasses to complex camera systems and microscopes. Similarly, the design of optical fibers relies on total internal reflection, a special case where light is completely reflected at the boundary, allowing efficient transmission of light over long distances with minimal loss.

1.4.4 Fluorescence

When a molecule absorbs a photon, it transitions from its ground state to an excited state. The excited state is highly unstable, therefore the molecule quickly relaxes to a lower energy state through various non-radiative processes, but can additionally manifest radiative deactivation pathways such as fluorescence. By doing so, the molecule, called fluorophore, returns to the ground state by emitting a photon. The emitted light always has a longer wavelength (lower energy) than the absorbed light due to the energy lost during the non-radiative relaxation process, and the shift in wavelength from absorption to emission is known as the Stokes shift [30]. The entire process occurs on a timescale of nanoseconds to microseconds. The efficiency of fluorescence emission is characterized by the quantum yield, which is the ratio of the number of photons emitted to the number of photons absorbed. This yield can

be affected by various factors, including the molecular structure, the environment of the fluorophore, and the presence of quenching agents [30].

Chapter 2: High density Hyperspectral Imaging

This chapter introduces and summarizes "gold-standard" and state-of-the-art methods currently employed in the detection and analysis of cerebral gliomas and glioblastomas. It also explores how these examinations can be improved using innovative approaches such as optical spectroscopy and imaging techniques, which are currently being developed and refined for human brain studies. A particular focus is placed on Hyperspectral Imaging (HSI), with an in-depth presentation of a transportable, high-density, spectral-scanning based HSI setup named HyperProbe1. The HyperProbe1 system enables *in situ*, rapid biochemical analysis and mapping of fresh surgical tissue samples immediately after excision, without the need for fixing, staining, or compromising tissue integrity. This chapter demonstrates a proof-of-concept for HyperProbe1's capabilities in quantitative biochemical mapping of surgical biopsies, highlighting its potential to revolutionize current post-surgical histopathological practices through non-destructive, *in situ* screening of fresh tissue samples within minutes of excision. Sections and figures of the journal article in [16] by L. Giannoni, M. Marradi et al have been modified and adapted to form parts of this chapter, with reprint permission under CC BY 4.0 License.

2.1 Overview of cerebral gliomas, glioblastomas and current examination methods

Gliomas are a broad category of brain and spinal cord tumors originating from glial cells (supportive cells in the nervous system) and are the most prevalent type of primary brain tumors. Among these, high-grade gliomas are particularly severe, with patients typically having a median survival of only 12–18 months despite receiving aggressive treatment involving extensive surgery, chemotherapy, and radiation therapy [36]. The treatment of these malignancies is further complicated by a remarkably high recurrence rate, with approximately 90% of cases recurring within two years of the initial diagnosis [36]. These tumors often recur within a median period of 6.7 months, necessitating regular imaging and ongoing management [36]. Glioblastomas (GBM), also known as *glioblastoma multiforme*, are

the most aggressive form of glioma. They are known for their rapid growth and tendency to infiltrate nearby brain tissue. Gliomas and glioblastomas represent significant challenges in neuro-oncology due to their complex behavior and resistance to conventional therapies. Advancements in molecular diagnostics and treatment strategies continue to be crucial in improving outcomes for patients affected by these aggressive brain tumors.

Histopathological examination of excised tissue remains the “gold standard” for post-surgical oncological evaluations [37], specifically in assessing critical parameters such as tumor type, grading, and classification in cases like glioma and glioblastoma resections [38–40]. Typically, after a surgical resection, fresh biopsy samples are sent to a histopathology lab, where they are preserved, sectioned, and stained, with hematoxylin and eosin (H&E) staining being particularly common [39]. These samples are then microscopically examined to determine their structural and molecular properties [39]. Despite its widespread use, modern histopathological analysis has several significant limitations. The most notable is the lengthy sample preparation process, which can delay results for several days to weeks post-surgery. Additionally, the subjective nature of histopathologists' interpretations can introduce variability, lacking a more quantitative and systematic approach to processing imaging results [41].

The latest categorizing system for tumors of the Central Nervous System (CNS) is provided by the World Health Organization (WHO) Classification of Tumors of the CNS. The WHO Classification is a comprehensive system used globally for the diagnosis and categorization of brain and spinal cord tumors. This classification integrates histological and molecular features to provide a detailed and standardized diagnosis. The latest edition, known as WHO CNS5, published in 2021 [42], includes significant updates and reflects the latest advancements in understanding CNS tumors. It uses molecular markers to classify tumors into subtypes that have different prognostic and therapeutic implications, making it a valuable tool for clinicians and researchers in the field of neuro-oncology [43]. The features of the WHO Grading are reported in Table 2.1:

WHO	Features of Grading
Grade 1	Low proliferative potential and can be cured with surgical resection.
Grade 2	Usually have diffuse infiltrative and low proliferative potential, with low chance of recurrence rate. May have the risk of progression to high grade.
Grade 3	Malignant histologic features, with high recurrence rate and usually need chemotherapy/radiotherapy.
Grade 4	Highly malignant tumors which are necrotic and have the capability of fast recurrence. Most of them show diffuse spreading in the CNS.

Table 2.1: Characterization of CNS tumors according to the WHO grading [44].

In order to aid pathologists and neurosurgeons with the management of CNS tumors, post-operative prognosis and treatment planning could greatly benefit from a novel approach that provides faster and more reliable information on tissue biopsies. Ideally, this would involve *in situ* screening immediately after surgery, yielding quantitative results within minutes to hours.

2.2 Human brain optical spectroscopy and imaging

Dr. Frans Jöbsis was a pioneering scientist who demonstrated that noninvasive cerebral monitoring was possible in humans using near-infrared (NIR) light. In the late 1970s, Jöbsis discovered that NIR light could penetrate biological tissues, including the skull and brain, enabling the measurement of brain oxygenation and blood flow [45]. A tool originally designed for monitoring brain perfusion and oxygenation has given rise to an entire field of study, aimed at exploring fundamental aspects of brain metabolism, blood flow, perfusion, pressure, water concentration, light scattering, and overall brain physiology, among other areas [46].

In this paragraph, the main optical spectroscopy and imaging methods relevant to CNS tumor studies will be presented, with a primary focus on three significant techniques: near-infrared spectroscopy (NIRS), diffuse optical tomography (DOT), and HSI, with particular emphasis on the latter. These techniques hold significant

promise for histological screenings of CNS tumors due to their ability to provide real-time feedback, detailed molecular information, and a comprehensive understanding of the tumor environment. This potential can lead to better diagnosis, treatment planning, and monitoring. Optical brain imaging techniques can distinguish between malignant and benign tissues, identify tumor margins with high precision, and detect molecular changes associated with different tumor types [47,48]. Current diagnostic methods rely on traditional histological analyses that require tissue samples and extensive processing. In contrast, the mentioned optical methods can assess the tissue *in situ*, offering significant advantages in terms of speed, patient comfort, and the ability to monitor changes over time [16,47,48].

Optical brain imaging techniques, like HSI, leverage the significant benefits of using various spectral bands to examine biological tissues. This method aims to gather crucial physiological data. Key advantages of this approach include (1) its high sensitivity to changes in brain function and (2) the ability to identify specific optical signatures associated with fundamental brain molecules and substances, thereby creating what is referred to as intrinsic contrast [49,50].

2.2.1 Near-infrared spectroscopy for brain monitoring

NIRS is an advanced optical imaging technique that has gained prominence for its ability to non-invasively monitor cerebral hemodynamics and tissue oxygenation. NIRS provides a unique window into the brain's metabolic and vascular activities, offering critical insights in both clinical and research settings. This technology is especially valuable for its portability, cost-effectiveness, and capacity for real-time monitoring, making it suitable for a wide range of applications. The main NIRS modalities include Continuous-Wave NIRS (CW-NIRS), Frequency-Domain NIRS (FD-NIRS), and Time-Domain NIRS (TD-NIRS), each offering varying degrees of spatial resolution, depth sensitivity, and accuracy.

2.2.1.1 Continuous-Wave NIRS

Continuous-Wave Near-Infrared Spectroscopy (CW-NIRS) is a non-invasive optical technique used to measure tissue oxygenation and hemodynamics. It employs continuous NIR light to monitor changes in the absorption by oxygenated and deoxygenated hemoglobin, allowing for real-time assessment of cerebral

oxygenation and blood flow. This technique utilizes a steady, continuous light source, usually laser diodes or light-emitting diodes (LEDs) [46,51], for the measurement of changes of the aforementioned species in the tissue [46]. The temporal changes of light intensity detected at the tissue surface can be directly linked to the concentration of these tissue chromophores inside the brain [46]. The affordability and compactness of CW-NIRS instruments make them especially suitable for functional brain studies, where significant hemodynamic responses are induced by neuronal activation [46]. Although the fundamental principles of CW-NIRS monitoring have remained consistent for several years, recent advancements in optics and microelectronics have led to the development of high-density CW-NIRS systems that enhance image quality, resolution, localization, specificity, as well as wearable devices that enable physiological monitoring in natural settings [51].

2.2.1.2 Frequency-Domain NIRS

Frequency-Domain Near-Infrared Spectroscopy (FD-NIRS) is an advanced optical technique used to measure tissue oxygenation, hemodynamics, and other physiological parameters. Unlike CW-NIRS, which uses continuous light, FD-NIRS employs intensity-modulated light at specific frequencies to provide additional information about the optical properties of tissues [52]. The light sources employ high frequency modulations (typically in the MHz range). This modulation allows for the measurement of both the amplitude and the phase shift of the detected light. By analyzing the phase shift and amplitude attenuation of the modulated light, FD-NIRS can determine the absorption and scattering coefficients of the tissue. This provides more detailed information compared to CW-NIRS [52]. Concentrations of chromophores (such as oxygenated and deoxygenated hemoglobin) can be inferred more accurately and with absolute quantification by separating absorption and scattering effects, along to information about the depth of the tissue being measured, enhancing its ability to localize signals in specific brain regions [52].

2.2.1.3 Time-Domain NIRS

Time-Domain Near-Infrared Spectroscopy (TD-NIRS) is an optical technique that works by measuring the time it takes for short pulses of NIR light to travel through tissue. This method provides detailed information about the tissue's absorption and scattering properties, which can be used to assess absolute cerebral oxygenation and

blood flow very accurately and with high precision [31]. By using pulsed light and by measuring the time of flight, scattering and absorption characteristics of the tissue can be determined [31]. Additionally, by analyzing the time distribution of the detected photons, TD-NIRS can provide information about different tissue depths, offering better spatial resolution and localization [31]. Another positive feature is that it can allow the independent measurement of the absorption and scattering coefficients of the tissue, enhancing the accuracy of chromophore concentration estimates (e.g., oxygenated and deoxygenated hemoglobin) [31].

2.2.2 Diffuse Optical Tomography

Diffuse Optical Tomography (DOT) operates by projecting NIR light into the brain through an array of sources and detecting the scattered light through an array of detectors to sample the entire head of a subject and reconstruct three-dimensional images of the brain's functional and structural state [53,54]. Advanced algorithms process the detected signals to reconstruct 3D images. These images reflect the concentration and distribution of chromophores, such as oxy-hemoglobin and deoxy-hemoglobin, providing insights into brain oxygenation and blood volume [53,54]. Recent technological and methodological advancements have significantly enhanced the capabilities of DOT: with the High-Density DOT, by increasing the density of sources and detectors, the spatial resolution and quality of the reconstructed images are remarkably improved [55].

2.2.3 Fluorescence-Guided Surgery

Focusing on malignant tissue removal, fluorescence-guided surgery (FGS) has become a widely adopted technique for improving the surgical resection of brain tumors, offering surgeons enhanced visualization of tumor margins [56,57]. This approach relies on the use of fluorescent dyes, such as 5-aminolevulinic acid (5-ALA), which are metabolized into fluorescent compounds that preferentially accumulate in tumor tissues [56,57]. Under specific wavelengths of light, these compounds emit fluorescence, enabling surgeons to distinguish malignant tissue from healthy brain tissue in real time. Clinical studies have shown that FGS can significantly improve the extent of tumor resection, reduce the likelihood of residual cancerous tissue, and ultimately enhance patient outcomes. Despite its promise, the technique has certain limitations, primarily due to its dependence on

exogenous contrast agents. These agents carry potential risks, including allergic reactions, liver disfunction, chronic kidney disease and other side effects, and may exhibit limited specificity in distinguishing certain tumor subtypes [57]. Furthermore, the intensity and distribution of fluorescence can vary depending on tumor heterogeneity and metabolic activity, which may pose challenges in certain clinical scenarios [57]. Finally, the costs of most of the existing fluorophores are quite high [57].

2.2.4 Raman Imaging

Raman spectroscopy represents another innovative technique that has gained attention for intraoperative brain tumor identification [58,59]. By analyzing molecular vibrations induced by light scattering, Raman spectroscopy provides highly specific biochemical information about tissue composition. This specificity makes it a powerful tool for differentiating cancerous tissue from healthy brain tissue based on their molecular signatures [58,59]. However, Raman spectroscopy faces several challenges that limit its widespread use during surgery. The technique requires significant time for signal acquisition and for the collection of maps, which may be impractical in the fast-paced environment of the operating room [59]. Additionally, interpreting Raman spectra can be complex, particularly in heterogeneous tissues, requiring advanced data analysis algorithms and expert knowledge [59]. Despite these challenges, research into Raman spectroscopy continues, with ongoing advancements aimed at improving its speed and usability for clinical applications.

2.2.5 Hyperspectral Imaging

HSI is an advanced technique that captures and processes information from across the electromagnetic spectrum, providing detailed spectral data for each pixel of an image. This kind of data is obtained through the collection of three-dimensional spatial and spectral information in 3D ‘datacubes’ or ‘hypercubes’, e.g., of the form: $I(x,y,\lambda)$ [60]. An example is reported in Figure 2.1. By doing so, for each pixel of the image, a corresponding spectrum (λ) of reflected, transmitted and/or fluorescent light can be extracted [60].

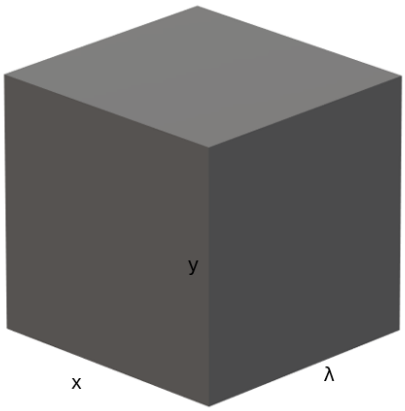

Figure 2.1: Data from hyperspectral imaging can be represented as a hyperspectral cube with coordinates x, y, λ.

In the context of human brain monitoring, hyperspectral imaging offers unique capabilities to analyze brain tissue composition, function, and pathology status with high spectral resolution [12]. HSI utilizes a wide range of wavelengths (typically from ultraviolet to NIR) with narrow spectral bands [12]. This enables detailed characterization of tissue properties based on the absorption and scattering of light, thus allowing tissue differentiation: by analyzing spectral signatures, HSI can differentiate between various types of brain tissue (e.g., gray matter, white matter, lesions) and quantify biomolecules such as oxygenated and deoxygenated hemoglobin, water, lipids, and cytochromes [60,61]. The latter feature allows HSI to detect abnormalities and lesions inside the brain tissue that may indicate diseases such as tumors, strokes, or neurodegenerative disorders [12,60,61]. The ability to map tissue characteristics at a microscopic level can aid in early diagnosis and treatment planning [60,61]. It is also used for functional brain imaging by assessing hemodynamic responses (changes in blood oxygenation and volume) associated with neuronal activity [12]. This makes HSI valuable in cognitive neuroscience research. Although primarily used in research settings, advancements are being made towards developing non-invasive and real-time applications of HSI for clinical use, such as intraoperative guidance [60,61], which is also the final goal of this research project [61].

2.3 Operation principles of hyperspectral imaging systems

Depending on the design of the hyperspectral imaging system, the hypercube data can be collected using different modalities. The three main acquisition modes are spectral scanning, spatial scanning, and snapshot imaging [62]. The present paragraph aims to summarize these concepts.

2.3.1 Spectral scanning mode

With the spectral scanning modality, the entire field of view (FOV) of the target is imaged sequentially at different wavelengths by selecting specific spectral bands one at a time, resulting in the collection of one image for each selected wavelength [62]. The final hypercube is reconstructed by stacking all the images along the spectral dimension [62]. A scheme of this modality is shown in Figure 2.2. Spectral scanning modality can be achieved either by filtering the excitation side (which means filtering the light source) or filtering the emission side (emitted/reflected light) before reaching the detector. Devices such as acousto-optic tunable filters (AOTFs) or liquid crystal tunable filters (LCTFs) are advantageous for this purpose due to their speed, compared to traditional mechanical filtering solutions, like filter wheels [62]. Additionally, AOTFs and LCTFs offer the benefits of using a higher number of spectral bands and achieving higher spectral resolution. However, these advanced technologies come with higher costs with respect to mechanical filtering options [62].

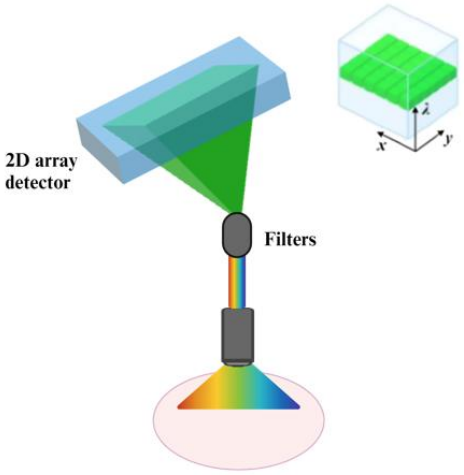

Fig. 2.2: Scheme of the spectral scanning acquisition mode. In this particular configuration the emission side is filtered. The alternative version features the same scheme but with filtering applied to the excitation side instead of the emission side.

2.3.2 Spatial scanning mode

The spatial scanning modality collects the entire spectrum (λ) for one spatial coordinate (x,y) at a time, offering the highest level of spectral resolution, but significantly adding to the total acquisition time in order to map the entire FOV. It can be achieved using two scanning approaches: the whiskbroom and the pushbroom scanning modes (Figure 2.3). Whiskbroom instruments scan both spatial and spectral dimensions simultaneously by collecting the complete spectrum for each pixel, one point at a time. The hypercube is then reconstructed at every spatial coordinate (x, y) [62]. On the other hand, pushbroom devices scan the spectral data for an array of pixels to reconstruct the hyperspectral dataset line by line. Both scanning modes involve the use of moving mirrors, gratings, or other optical components to distribute the light into a spatial-spectral plane and are not able to display in real-time the entire FOV of the image [12,62]. Additionally, they can often require a complex and precise synchronization of moving parts. For this reason, they are usually suitable only for controlled environments where the scene does not change rapidly [12].

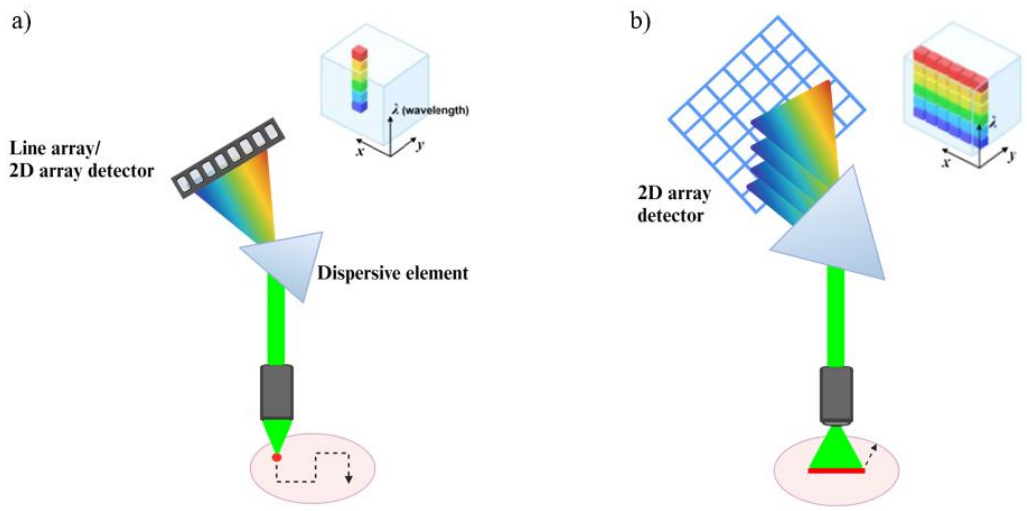

Fig. 2.3: Schemes showing the a) whiskbroom and b) pushbroom scanning modalities.

2.3.3 Snapshot mode

Snapshot imagers can capture the entire hyperspectral data cube in a single snapshot without the need for scanning (Figure 2.4) [62,63]. Consequently, the speed of these instruments is significantly higher, thus enabling real-time dynamic observations

and making it a perfect match for fields such as cellular tissue imaging [64]. In order to reach lower acquisition times, snapshot devices utilize advanced sensor designs and a higher number of total available detector elements [63]. Of course, higher speeds require some trade-off in spatial and spectral resolution [62,63]. In addition to more complex sensor design and lower spatial/spectral quality, the handling of a great volume of data, its processing and the need of highly complex hardware can be more challenging [62,64].

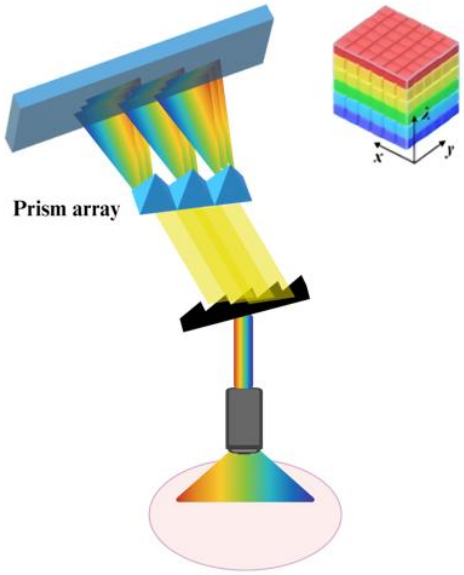

Fig. 2.4: Scheme of a HIS system based on snapshot acquisition modality.

2.4 *HyperProbe1*: a novel HSI system designed for the analysis of glioma biopsies

The *HyperProbe1* is a laboratory-scaled HSI system designed for the spectral analysis of fresh *ex vivo* samples of glioma from surgical biopsies [61]. The aim of the device is to allow a flexible use of wavelengths in the visible and NIR range, enabling the selection of different types and numbers of spectral bands, in addition to the use of innovative solutions for illumination, spectral separation, detection of light and image reconstruction. The success of HyperProbe1 in providing quantitative biochemical analysis and mapping of surgical biopsies can pave the way to a novel, fast and greatly enhanced methodology to perform *in situ* histopathological screening right after surgery, without the need for any manipulation or degradation of the samples. It is the first version of a HSI imaging

system that is currently under development to achieve the final goal of delivering an innovative and compact device, that can allow precise *in vivo* and real time surgery guidance for brain tumor resection. The concept, design, technical characteristics and results of HyperProbe1 are going to be presented in the following paragraphs.

2.4.1 Description of HyperProbe1

HyperProbe1 is a custom-built HSI system based on spectral scanning acquisition modality [16]. As mentioned previously in **Sec. 2.3.1**, in order to collect the entire hypercube of the FOV of the sample, the images are acquired sequentially by rapidly selecting each spectral band, one at a time [60]. Afterwards, the spectral images are stacked together to reconstruct the final 3D hypercube. The schematics of the entire system are reported in Figure 2.5, and in Table 2.2 is reported a comprehensive list of all the components.

The illumination side of HyperProbe1 is composed of a supercontinuum laser (SCL) by NKT Photonics, model SuperK FIANIUM FIR20. The latter generates coherent light with a broadband illumination in the range of 400-2400 nm (at a maximum total power of 6.5 W). The light produced by the SCL is then filtered by a set of acousto-optic tunable filters (AOTF; NKT Photonics, SELECT VIS-nIR), which allows to filter selectively any spectral band in the range of 500 – 900 nm. This model reaches a minimum bandwidth (full width at half maximum; FWHM) of 3.5 nm in the visible range and a maximum bandwidth of 7 nm in the NIR range. The AOTF device is connected through an alignment instrument, called SuperK CONNECT (NKT Photonics), to an optical fiber of 1 mm core diameter. Due to some instability issues of the illumination side, the fiber is coupled with a pair of laser amplitude stabilizers, placed in series (Thorlabs, NEL02A/M and NEL03A/M), which are able to cancel intensity noise and maintain illumination stability over time within 0.05% of a selected output power. Two amplitude stabilizers are needed in order to cover the entire spectral range between 500 and 900 nm. The latter elements are followed by a laser speckle reducer (Optotune, LSR-3005-6D-NIR) and an achromatic doublet lens that diverges the beam to ensure an illumination spot of 2-3 cm^2 on the target. On the imaging side, a scientific complementary metal-oxide semiconductor (sCMOS) camera can be found

(Hamamatsu, ORCA-Flash 3.0, model C11440-22CU). The camera is characterized by a sensor size of 2048 x 2048 pixels, with pixel size of 6.5 µm, 82% peak quantum efficiency (at 620 nm), and maximum readout rate of 40 fps. It is coupled with a 15x reflective objective (Thorlabs, LMM-15X-P01) and an infinity-corrected, conjugated tube lens (Thorlabs, TTL200-B), to generate a FOV of the target of about 0.9 x 0.9 mm^2. For easy transportation, the illumination side is mounted on a wheeled rack, meanwhile the illumination probe and imaging side can be installed on a small breadboard for improved stability.

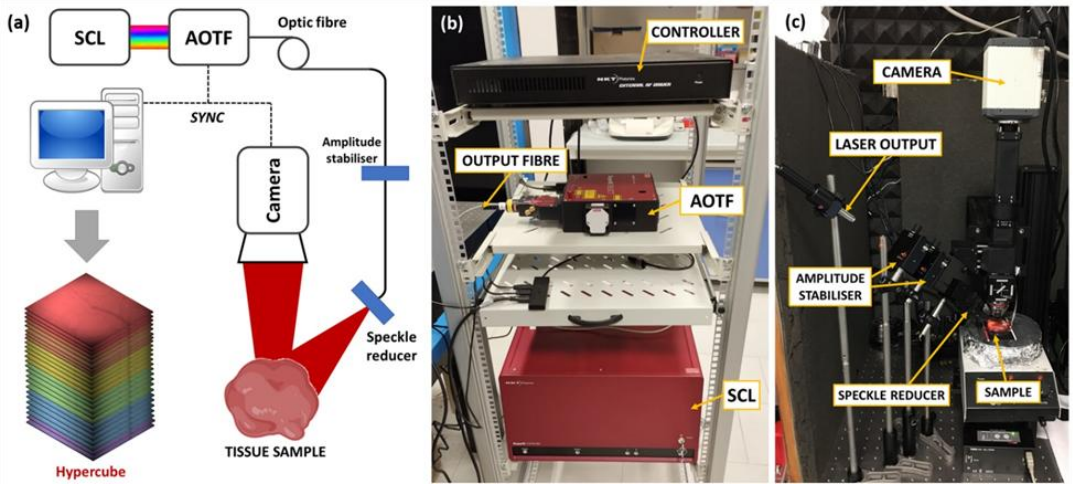

Fig. 2.5: (a) General scheme of HyperProbe1; (b) Photograph of the illumination side of HyperProbe1: SCL source, the AOTF and the controlling devices (drivers); (c) Picture of the imaging and detection side of HyperProbe1, representing the laser output, the amplitude stabilizers, the speckle reducer and the camera.

Component	Manufacturer and model	Key specifics
SCL	NKT Photonics, SuperK FIANIUM FIR20	Broadband illumination (400-2400 nm); Maximum total power of 6.5 W;
AOTF	NKT Photonics, SELECT VIS-nIR	Broadband selection (510-900 nm); Spectral resolution of 3.5-7 nm (FWHM);
Camera	Hamamatsu, ORCA-Flash 3.0 (C11440-22CU)	4.2-MP (2048 x 2048) CMOS sensor; 6.5-µm pixel size; QE up to 82% (Visible and NIR); Maximum frame rate of 40 fps;
Amplitude stabilizers	Thorlabs; NEL02A/M + NEL03A/M	Amplitude stabilization within ±0.05%;
Speckle reducer	Optotune; LSR-3005-6D-NIR	Transmission up to 98%;
Optical fibers	NKT Photonics	Broadband coverage (400-2000 nm); High power throughput (up to 500 mW); 1-mm core diameter;
Objective	Thorlabs, LMM15X-P01	15x reflective objective; FOV of 0.9 x 0.9 mm^2;
CMOS: Complementary metal-oxide semiconductor; FWHM = Full-width at half maximum; QE = Quantum efficiency; NIR = Near-infrared; FOV = Field of view.		

Table 2.2: List of components of HyperProbe1 and their specifications.

2.4.2 Spectral and power characterization

A comprehensive technical characterization of the illumination side of HyperProbe1 has been conducted, focusing on its power emission and its spectral performance. An overview of the spectral output of the system, showing spectral bands from 500 to 900 nm with a step of 20 nm, is shown in Figure 2.6. Each spectrum was measured separately, using a portable spectrometer (FLAME-T-VIS-NIR-ES, Ocean Optics), located directly at the output of the optical fiber.

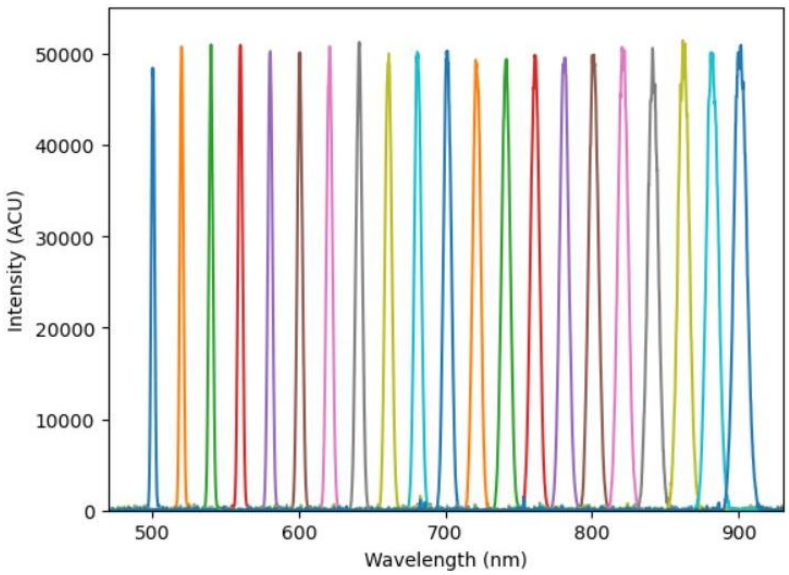

Fig. 2.6: Spectral output of the HyperProbe1 system, for 21, evenly-sampled wavelength bands from 500 nm to 900 nm, at 20-nm steps.

All the 21 sampled bands have been characterized by performing a gaussian fitting of their spectra, in order to estimate the FWHM of the band. The results are shown in Table 2.3:

Spectral band (nm)	Wavelength centroid (nm)	FWHM (nm)
500	500	3
520	520	3
540	540	3
560	560	3
580	581	3
600	601	4
620	621	4
640	641	5
660	661	5
680	681	5
700	701	6
720	721	6
740	741	7
760	761	7
780	781	7
800	801	7
820	821	8
840	842	8
860	862	9
880	882	9
900	901	10

Table 2.3: Spectral band, wavelength centroid and FWHM, resulting from the Gaussian fit, for each sampled spectral band.

In particular, spectral resolution of each spectral band of the HyperProbe1 system is inferred from the FWHMs of the gaussian fitting functions of the bands. It is demonstrated that the HyperProbe1 system is capable of achieving a spectral resolution of about 3 - 6 nm in the visible range and of approximately 6 - 10 nm in the NIR range.

The power emission of HyperProbe1 has also been characterized. To select a specific power value, the power percentage of the SCL or the AOTF device, or both, can be adjusted using the NKT Photonics CONTROL software. Emission values from the illumination side of HyperProbe1 were measured with a power meter

(PM100D coupled with sensor S120C, Thorlabs) directly at the optical fiber output, with both the SCL and the AOTF set to 100% of power. The results are reported in Table 2.4:

Wavelength (nm)	**Power (mW)**
500	2.0
550	2.4
600	3.9
650	5.4
700	9.1
750	9.3
800	10
850	9.8
900	5.6

Table 2.4: Power characterization of 9 sampled spectral bands, from 500 to 900 nm with a 50 nm step.

From the table reported above, it is easily noticed that the output power of the illumination side is not constant, presenting a peak at around 800 nm. This represents an issue, since maintaining a constant output power on the target's surface is crucial as it allows for the use of a fixed integration time for the camera across all spectral bands. Additionally, the power variation across the entire spectral range is too high for the amplitude stabilizers to function properly and must be leveled out before reaching them. To address these problems, a power calibration curve was constructed using the following approach: the AOTF percentage was adjusted to select only one fixed output power value (mW) that remains consistent across all selected spectral bands. The AOTF percentages that ensured the same output power value (mW) for each wavelength were recorded to create the calibration curve. These measurements were taken manually using the power meter, with the SCL power percentage maintained constantly at 100% for every wavelength. The final output power provided using the power calibration curve is around 2 mW at the optical fiber's output and ranges from 100 to 500 μW per band on the surface of the target, as shown in Figure 2.7 (it is lower due to the presence of the laser speckle reducer and the amplitude stabilizers).

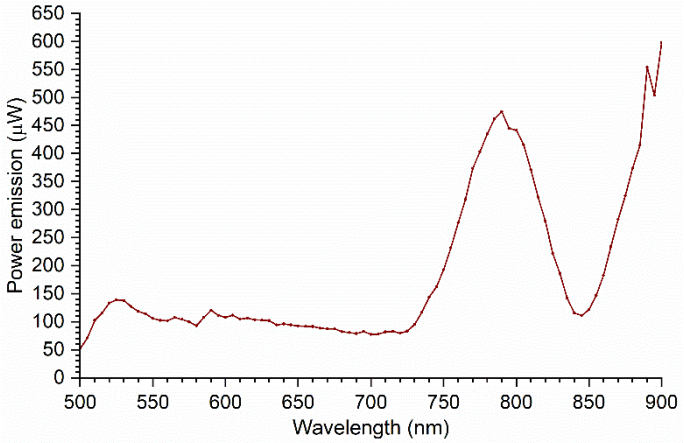

Fig. 2.7: Power output of each spectral band of the HyperProbe1 system achieved using the calibration curve and the amplitude stabilizers. These measurements were acquired using the previously mentioned power meter, with the laser set to continuous mode. In this mode, the laser automatically sweeps across the 500–900 nm range at a predefined interval. For this experiment, a step size of 5 nm was selected. The curve shows variations in power emission across the spectrum, with two noticeable peaks: one occurring around 800 nm and another towards 900 nm. A smaller, less pronounced fluctuation is observed near the 500–550 nm region.

This method, coupled with the use of the two amplitude stabilizers, enables to utilize a fixed integration time for the camera across the spectral range during the collection of an entire hypercube (ideal integration times can go from 5 to 30 ms depending on the target). This constancy also ensures a sufficient signal-to-noise ratio (SNR). Typical acquisition times for a complete hypercube (79 bands) can range from 1 to 5 minutes, for biological targets. A further discussion of the temporal resolution is provided in **Sec. 2.4.4**.

2.4.2.1 Improving power output stability using amplitude stabilizers

As previously mentioned, a power calibration curve is essential to ensure consistent output power on the target's surface. However, this alone was insufficient due to inherent stability issues on the illumination side. Throughout this project, various options were considered, and the most effective solution proved to be the use of laser amplitude stabilizers. These stabilizers were chosen for their efficiency, rapid response, and ease of integration into the HyperProbe system. Laser amplitude stabilizers, also called noise eaters, are devices designed to maintain a consistent output intensity from a laser, counteracting fluctuations that can arise due to various factors such as power supply variations, environmental changes, or intrinsic laser

noise [29]. Two amplitude stabilizers were initially tested individually: the Thorlabs NEL02A/M, which operates in the 425 - 650 nm range, and the Thorlabs NEL03A/M, which covers the 650 - 1050 nm range. These devices were evaluated using a white reference standard (Labsphere, Spectralon® 5"), which guarantees a reflectance >99% over a range from 400 to 1500 nm. Multiple hypercubes of the Spectralon were acquired every 10-15 minutes over the course of an hour, using the power calibration curve mentioned in the previous paragraph. A region of interest (ROI) was selected to calculate the average intensity count across the spectral range (as shown in Figure 2.8):

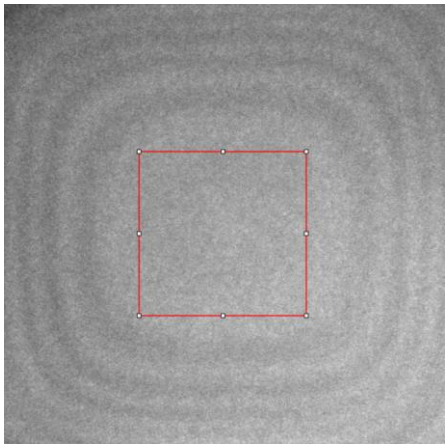

Fig. 2.8: Selection of a ROI (red square) at the center of each image of the hypercubes collected for the Spectralon. The average intensity counts for each image are then calculated and reported in function of λ. It is possible to average on the entire ROI due to the homogeneity of the target.

Without noise eaters, the intensity counts decreased over time. Using the amplitude stabilizers individually provided only partial stabilization, as neither covered the entire spectral range. Based on these results, we combined both stabilizers to further optimize their performance. The Noise Eaters were coupled through a two-step process. The first step involved a rough alignment, during which the output beam of the first Noise Eater was centered onto the input window of the second Noise Eater. In the second step, fine alignment was performed by monitoring the output power of the second Noise Eater using a Thorlabs power meter. The Noise Eaters were carefully adjusted through slight shifts and tilts until the output power reached a satisfactory level. The results of the tests are reported in Figure 2.9:

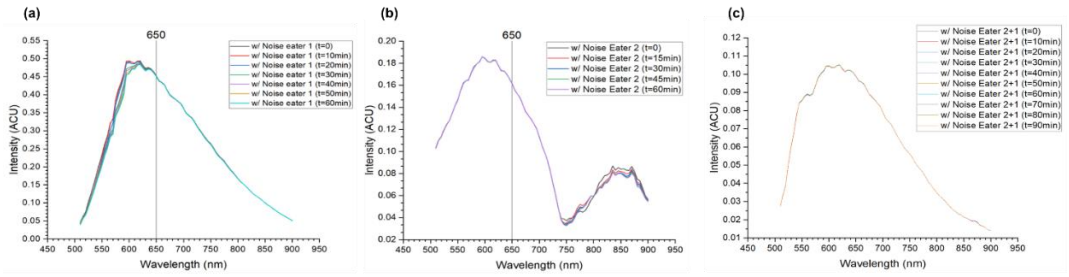

Fig. 2.9: (a) effects of the NEL03A/M alone, which covers the 650-1050 nm range. As expected, the region below 650 nm remains very noisy. The average intensity at 600 nm is calculated as 0.01 ± 0.5, including the standard deviation. (b) Effects of the NEL02A/M, which operates only in the 425-650 nm range, showing no impact on the spectrum beyond this range. The average intensity at 850 nm is calculated as 0.083 ± 0.004. (c) The final output, stabilized over time, achieved by coupling both noise eaters together. The average intensity at 600 nm is 0.905 ± 0.005, while at 850 nm it is 0.0122 ± 0.0002. This demonstrates that the standard deviation decreases significantly when the noise eaters are used in combination, ensuring a temporally stable output. The number of individual experiments performed was 7 for test (a), 5 for test (b), and 9 for test (c). The number of experiments was determined by the operator based on the amount of data required for each Noise Eater, primarily influenced by their stabilization efficiency.

2.4.3 Imaging characterization

The imaging capabilities of the HyperProbe1 system are thoroughly examined in the following paragraphs, with a particular focus on evaluating and quantifying its image quality and performance. Specifically, the assessment covers: (1) the spatial resolution of the HyperProbe1; (2) the system's image contrast and signal-to-noise ratio (SNR), also by analyzing the impact of the laser speckle reducer (LSR) on overall image quality; (3) the field of view (FOV); and (4) the potential presence of imaging aberrations, including focusing errors and other optical distortions.

2.4.3.1 Spatial resolution

The spatial resolution of HyperProbe1 was evaluated for each individual spectral band using a positive resolution test target, the USAF 1951 (Thorlabs R1L1S1P). In general, this resolution target consists of groups and elements featuring black lines of varying thicknesses and spacings. Each element within these groups represents a specific spatial resolution value, measured in lines per millimeter (lp/mm). The spatial resolution of the imaging system is determined by the smallest element of the USAF 1951 target that the system can clearly resolve. The USAF

1951 target was illuminated with 9 sample spectral bands. The results are reported in Figure 2.10:

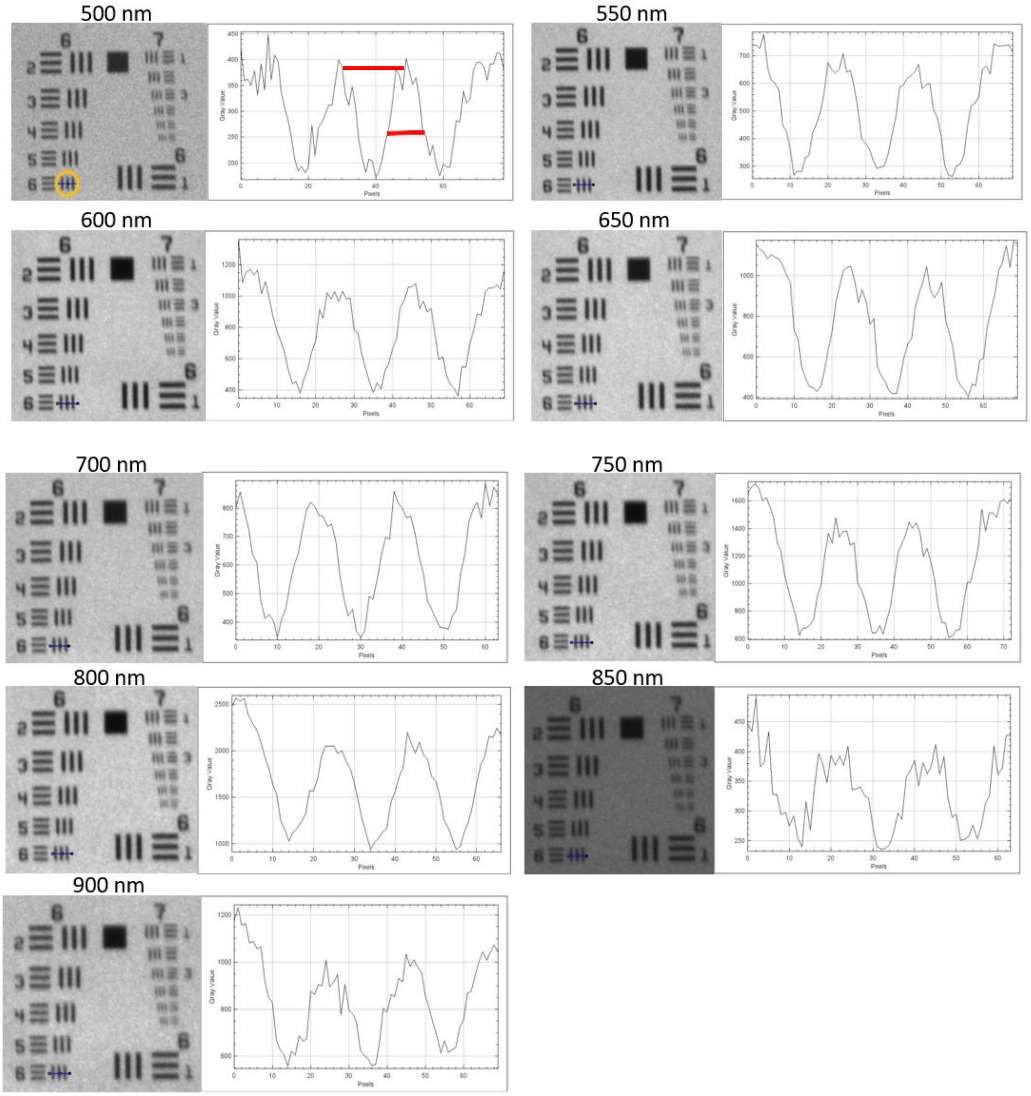

Fig. 2.10: The USAF 1951 target illuminated with 9 sample spectral bands (the wavelength is reported above each image). The smallest element of the target that the system can clearly resolve is the one circled in yellow (group 6, element 6) in the first reported image (collected at 500 nm). This is also confirmed by the analysis of the line profile of the cross-section view of the element (intensity vs pixels laying over the three lines of Group 6 Element 6, indicated with the small blue line), reported next to the image of the target, which is a typical method used to understand if the element can be clearly resolved. An element is considered clearly resolved when the FWHM of the peak is comparable to or smaller than the distance between adjacent peaks (as shown with the red lines reported in the Figure at 500 nm).

Across all these imaging assessments, HyperProbe1 consistently demonstrated a spatial resolution of 114 line pairs per millimeter (lp/mm), which corresponds to a

smallest resolvable detail of 4.38 μm. This shows that the system provides high spatial resolution that is maintained approximately stable across the whole spectral range, and which is suitable for the microscopic analysis of brain biopsies.

2.4.3.2 Image contrast and SNR

An assessment of image contrast (C) and signal-to-noise ratio (SNR) has been conducted for each spectral image obtained from 9 sample spectral bands using the HyperProbe1 system. These measurements were performed on images of the same calibrated target, acquired with and without the use of the LSR, in order to evaluate its effect on the performance of the system.

Contrast (C) quantitatively measures how distinct or well-defined the boundaries are between objects or regions within an image. Higher contrast means that there is a greater difference in brightness or color between adjacent pixels or regions, leading to sharper edges and clearer visibility of details. Conversely, lower contrast results in a more uniform appearance where distinctions between objects or details are less pronounced. In mathematical terms, image contrast C can be expressed as:

$$C = \frac{\Delta \mathrm{I}}{\langle \mathrm{I} \rangle} \tag{2.9}$$

in which ΔI is the variation in the detected light intensity in the ROI with respect to the background, while $\langle I \rangle$ is the average intensity of the background [30]. In brain optical imaging, image contrast is generated by the presence of different types of tissue, such as vasculature and surrounding cortical grey matter, that are characterized by different absorption values usually caused by changes in the hemoglobin content.

SNR in imaging refers to a quantitative measure of the level of desired signal (such as the brightness or intensity of an object of interest) compared to the level of background noise (unwanted random fluctuations or interference) present in an image. It assesses the clarity and fidelity of the signal relative to the amount of noise that may degrade the image quality and can be expressed as:

$$SNR = \frac{\langle \mathrm{I} \rangle}{\sigma_I} \tag{2.10}$$

where σ_I is the standard deviation of the background intensity.

Image contrast C and SNR are calculated in specific ROIs for each of the 9 sample spectral images using the same calibrated target, with and without the use of the LSR. Two square ROIs are selected: a ROI located entirely on a darker region, such as on the ticks in the calibrated target, and a ROI located on a brighter region corresponding to the white background of the calibrated target. An example of the image of the target and the selected ROIs is reported in Figure 2.11:

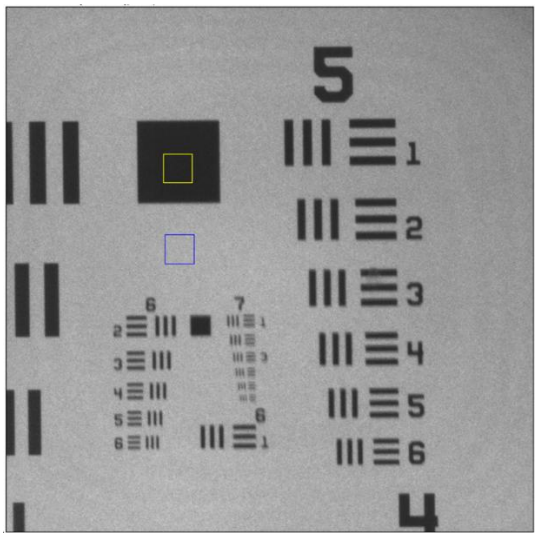

Fig. 2.11: Image of the calibrated target collected at 550 nm with the activated LSR. The yellow squared ROI corresponds to the dark region, meanwhile the blue squared ROI is the selected bright region.

The results of the analysis for every sampled spectral band are reported in Table 2.5:

Wavelength (nm)	**Contrast, LSR on**	**Contrast, LSR off**	**SNR, LSR on**	**SNR, LSR off**
500	0.7	0.7	15	12
550	0.8	0.8	18	13
600	0.9	0.9	21	13
650	0.9	0.9	20	12
700	0.8	0.8	18	12
750	0.9	0.9	20	12
800	0.9	0.9	23	11
850	0.7	0.7	15	12
900	0.8	0.9	20	12

Table 2.5: Contrast and SNR values and comparison with and without the use of the LSR.

The results show that the use of the LSR does not impact the contrast performance but significantly improves the values of SNR over the entire spectrum, with an increase in the average SNR of about 55.99% (18.89 against 12.11).

2.4.3.3 Field of view

The field of view (FOV) of an image represents how much of the scene in front of the lens is captured in the image itself. The FOV strictly depends on the focal length of the lens, the objective and the size of the camera's sensor. The FOV of the HyperProbe1 was measured using a calibrated target, depicting a grid with a 100 µm pitch. The target was illuminated with the 550 nm spectral band. The result is reported in Figure 2.12:

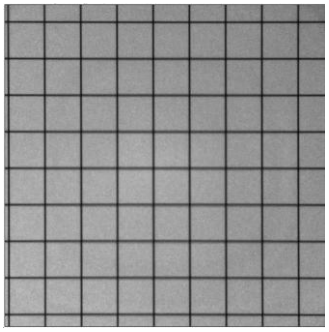

Fig. 2.12: Image of the 100 µm pitch target (the side of each square is 100 µm long), collected at 550 nm.

In the figure above, about 9 squares can be counted for both height and length of the image, meaning that the FOV is equal to 900 x 900 μm^2, which is an ideal value for the analysis of biopsies. Given that the sensor format is 2048 x 2048 pixels, the area of each pixel is equal to 900/2048 = 0,44 μm^2. Furthermore, since the effective area of the sensor of the sCMOS camera is equal to 13.312 mm^2, and that the magnification can be calculated from the following equation:

$$M = \frac{h_i}{h_0} \tag{2.11}$$

(where h_0 is the size of the target or the desired FOV and h_i is the size of the image on the sensor area of the camera), the resulting experimental magnification calculated with the equation reported above is 13.312/0.9 = 14.79, in accordance with magnifying power of the reflective objective (15x).

2.4.3.4 Assessment of image aberrations and distortions

Image aberrations and distortions are imperfections that occur in images captured by optical systems. These issues can arise due to the limitations in lens design, manufacturing defects, or specific physical properties of light. Some common types of aberrations and distortions are focusing errors, chromatic aberrations or other imaging artifacts. For this assessment, two distinct types of targets (Thorlabs R1L1S1P) are utilized: a target composed of 10 concentric circles with radii ranging from 100 μm to 1 mm, in 100 μm increments, designed to detect focusing errors, and a target consisting of two grids of 20 x 20 arrays, one with a 50 μm pitch and the other with a 10 μm pitch, which are employed to identify image aberrations or distortions across various scales. *These targets were chosen because they are effective for revealing visual distortions, such as warping, misalignment, or focus errors, which can easily be identified by comparing the captured images to the original structure of the targets. In fact, the evaluation of image quality in this case is qualitative rather than quantitative, as it is based on a direct visual inspection of the images obtained using calibrated targets.* Both types of targets were illuminated using the 550 nm spectral band in output from the illumination side and imaged with the imaging side of HyperProbe1. The results are reported in Figure 2.13:

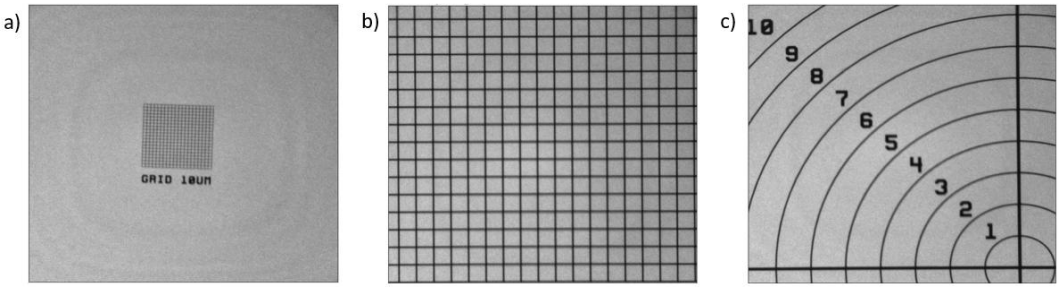

Fig. 2.13: a) 20 x 20 grid target with 10 μm pitch; b) grid target with 50 μm pitch; c) target made of 100-μm wide concentric circles.

The grid tests confirm that the imaging side of HyperProbe1 does not produce significant image aberrations or distortions.

2.4.4 Temporal resolution of HyperProbe1

The temporal resolution of HyperProbe1 was determined by evaluating the system's hypercube acquisition rate, defined as the number of hypercubes captured per second (hypercube/s). This rate is influenced by two main factors: the spectral

switching rate between wavelength bands and the camera's integration time for each frame.

The spectral switching rate for adjacent bands with a 5-nm separation, via AOTF, was specified by the filter manufacturer to be approximately 10-20 µs. In contrast, the integration time for the HyperProbe1 is also dependent on the system's power output, which is necessary to gather sufficient photons to maintain a high SNR. Based on the power output detailed in **Sec. 2.4.2**, the minimum integration time for the camera was estimated to be 1 ms when using a white calibration standard (Labsphere, Spectralon® 5"). The maximum integration time, determined during the application of HyperProbe1 on fresh surgical cerebral tissue biopsies, was calculated to be maximum 50 ms. Given the substantial difference between the spectral switching time and the integration time (three orders of magnitude), the hypercube rate of HyperProbe1 is primarily governed by the camera's integration time. Consequently, for the 79 available spectral bands, the system's hypercube rate ranges from a minimum of approximately 0.25 hypercubes/s (one hypercube every 4 seconds) to a maximum of approximately 12.66 hypercubes/s.

2.4.5 Summary of the main technical characteristics of HyperProbe1

An outline of the technical characteristics and features of HyperProbe1 is reported in Table 2.6:

Characteristics	**Illumination side**
Illumination mode:	Spectral scanning
Available spectral range:	510-900 nm
Minimum sampling step size:	5 nm
Maximum number of spectral bands:	79 (visible and NIR)
Spectral resolution (FWHM):	3.5 nm (visible), 7 nm (NIR)
Average output power per spectral band:	~200 µW (visible), ~450 µW (NIR)
Power stability over time:	± 0.05%
Characteristics	**Imaging side**
Type of detector:	sCMOS
Sensor format:	2048 x 2048 pixels
Pixel size:	6.5 µm
Spatial resolution:	4.38 µm
FOV:	0.9 x 0.9 mm^2
Frame rate:	40 fps (at full format)
Sensitivity (QE):	82% at 620 nm
Typical acquisition time (per spectral frame):	5 to 30 ms
Typical acquisition time (per hypercube):	1 to 5 min
NIR = Near-infrared; FWHM = Full-width at half maximum; CMOS: Complementary metal-oxide semiconductor; FOV = Field of view; QE = Quantum efficiency.	

Table 2.6: Technical characteristics and features of HyperProbe1.

2.4.6 Hyperspectral data acquisition via GUI

The file of the calibration curve described in **Sec. 2.4.2** is used within a virtual interface (VI) created by Dr. Luca Giannoni using the software NI LabVIEW 2022, specifically developed to utilize the sCMOS camera, the SCL and the AOTF all together with its calibration curve. The development of the VI was necessary because the NKT CONTROL software does not allow to change the operating power percentage of the AOTF or of the SCL during the acquisition of the entire spectral range. Therefore, another software that admits the use of the calibration curve is needed. The VI also enables the synchronization of the illumination side with the CMOS camera and automatically saves the images with a .dat extension. A picture of the Graphical User Interface (GUI) developed with the VI has been reported in Figure 2.14. The GUI allows to select a specific exposure time (ms) for the camera, the desired number of hypercubes to collect and other parameters such

as the starting wavelength and the step size. It also allows the selection of the path of the calibration curve file, and the folder where the images need to be saved. Furthermore, it shows the hypercube that is being acquired, the wavelength that is being emitted in real-time and the image that has just been collected.

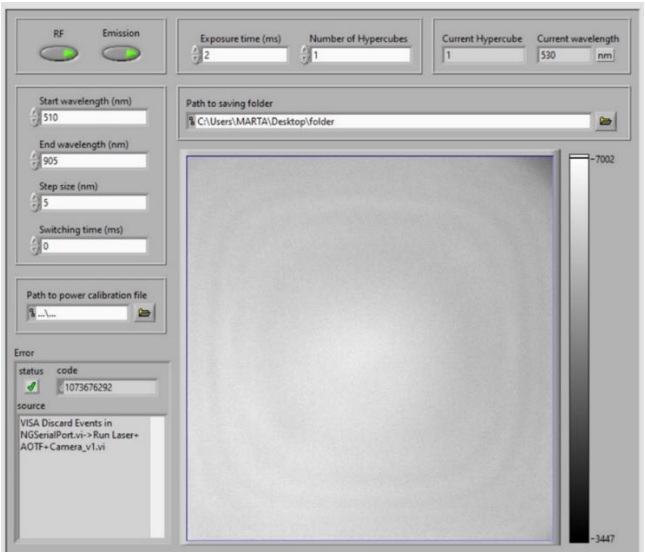

Fig. 2.14: A screenshot of the LabVIEW-based GUI software used to operate HyperProbe1 is shown. This software allows the user to select the desired starting wavelength, final wavelength, step size, and switching time between wavelengths. It also enables selection of the camera's integration time and the number of hypercubes to acquire sequentially. Additionally, it provides a live preview of the spectral images collected at each spectral band.

2.5 Analysis of glioma biopsies with HyperProbe

The present study employs HyperProbe1 to analyze fresh surgical biopsies of glioma tissue, aiming to validate its efficacy in characterizing tumor compositions and pathological features. Authorization for the study (Studio ID: 23672 - 23672_BIO) was granted by the Ethical Committee of the Area Vasta Centro Toscana, under Italian law and regulations. Informed consent was collected from each patient involved in the study. The brain tissue samples, sourced from routine neurosurgeries at the Azienda Ospedaliero-Universitaria Careggi in Florence, offer a good dataset for this evaluation. By imaging and analyzing 11 samples, this research ensures statistical reliability and explores specimen variability, comparing the findings with traditional histopathological methods classified by WHO (World Health Organization) gradings [42]. The following paragraphs provide a discussion about the specimens, their manipulation and the data acquisition protocol.

2.5.1 Description of the specimen

HyperProbe1 was utilized to image a collection of fresh glioma tissue biopsies (stored in a phosphate-buffered saline solution), aiming to validate its ability to extract quantitative data regarding the composition of the samples and to identify pathological characteristics comparable to those determined through traditional histopathological analysis. The brain tissue samples used in this study (as illustrated in Figure 2.15) were acquired from patients undergoing routine neurosurgical procedures for brain tumor removal at the Azienda Ospedaliero-Universitaria Careggi (University Hospital of Florence) in Florence.

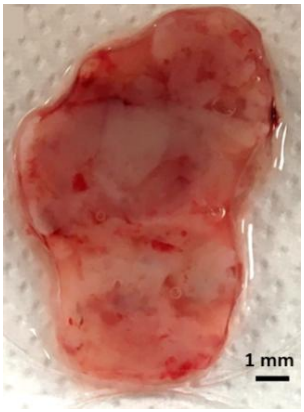

Fig. 2.15: Example of a sample of excised glioma tissue obtained from the surgical biopsies.

A total of 11 samples were imaged and analyzed using HyperProbe1, ensuring statistical robustness and allowing for an investigation of specimen variability. All the specimens were analyzed after a maximum of 1 hour after resection in the surgery room. These samples included portions of tissue typically sent for histopathological examination to determine tumor type based on WHO gradings [42].

The classification information for all samples utilized in the present study is summarized in Table 2.7, offering a broad characterization of various glioma types:

Sample identifier	2021 WHO grading	Additional info
S1	4	
S2	4	
S3	3	Discarded due to fragmented size
S4 (FOV1)	4	Two separate FOVs were acquired on the same sample
S4 (FOV2)	4	Two separate FOVs were acquired on the same sample
S5	4	Labelled with fluorescein
S6	2	Discarded due to presence of light interference
S7	2	Possibly shifting to higher grade (III)
S8	3	Labelled with fluorescein, presence of coagulated tissue
S9	4	Labelled with fluorescein, but negative
S10	2	Labelled with fluorescein
S11	4	Labelled with fluorescein, but negative

Table 2.7: Classification of the tissue samples investigated with HyperProbe1. It is important to note that labelling with fluorescein does not interfere with reflectance data acquisition since its maximum absorption corresponds to approximately 485 nm. Its absorption is almost negligible in the region between 510 nm (beginning of the emission spectrum of HyperProbe1) and 525 nm. As a result, the contribution of fluorescein to the HSI data is negligible and does not significantly affect the spectral analysis or interpretation of the results.

2.5.2 Manipulation of the specimen and data acquisition protocol

As mentioned in the previous table, two samples were discarded from the analysis: sample S3 was a biopsy composed of very small fragments of brain tissue (2-3 mm each at most) and, due to their dimensions, the acquired spectra appeared very flat (a large influence of partial volume effect is hypothesized). Additionally, for small samples, edges may contribute disproportionately to the spectral data, as they may reflect or scatter light differently compared to the interior of the tissue; meanwhile, sample S6 presented ambiguous patterns due to potential light interference at some wavelengths. In addition, for sample S4, due to its slightly larger dimensions than the rest of the biopsies (5-6 cm), it was decided to acquire two separate FOVs on the same tissue to further analyze variability within subjects. Finally, samples S8, S9 and S10 were marked with fluorescein during the surgery, albeit S9 was confirmed during operation to be negative to fluorescent emission.

For the HSI data acquisition, a portion of the glioma samples (average size of 2-3 cm) was preemptively washed in phosphate-buffered saline (PBS) to eliminate blood (blood distribution in the tissue may not be uniform, leading to localized variations in the spectral response and making it harder to interpret the results consistently) and other unwanted residuals, then imaged on its surface with HyperProbe1 at full capacity (79 wavelength bands at 5-nm steps between 510 and 900 nm) within 1 hour after excision. It was decided to start the acquisition from 510 nm instead of 500 nm because the latter spectral band did not provide a sufficient SNR due to low power emission. A thin glass coverslip (glass is transparent to visible light and NIR radiation, so it does not interfere in any way with the collected data) was placed over each sample to flatten its top surface for uniform focusing of the FOV, whilst a dark absorbing material was placed at the bottom to avoid any potential reflection of the light back into the tissue. The acquisition of a single hypercube for every sample was typically less than 5 minutes, a short enough duration to ensure that the tissue had not deteriorated nor oxidized during the imaging. Reference hypercubes were also collected after every acquisition of the specimens' hypercubes, using a white calibration standard (Labsphere, Spectralon® 5"). Additionally, dark hypercubes were registered with the illumination side turned off, to account for dark noise produced by the sCMOS camera.

2.6 Data processing and spectral unmixing

In the analysis of hyperspectral data acquired from brain glioma biopsies, data processing plays a crucial role in extracting meaningful information from the complex spectral datasets. The pipeline involves several stages, including preprocessing to correct for noise and artifacts and normalization to ensure consistency across samples [16]. Following these initial steps, thanks to the collaboration with the team of the Technical University of Munich - TranslaTUM, a spectral unmixing analysis is performed to decompose the hyperspectral signals into their constituent components [16], allowing for a detailed examination of the biochemical and structural composition of the glioma tissues. This approach not only enhances the accuracy of the diagnostic information retrieved but also enables

the identification of specific pathological features that may not be discernible through traditional imaging techniques.

2.6.1 Data processing for reflectance hyperspectral data

Reflectance hypercubes $R(x,y,\lambda)$ for each sample were reconstructed by normalizing the hyperspectral data of the reflected light intensity $I(x,y,\lambda)$ acquired with HyperProbe1 with reference hypercubes $W(x,y,\lambda)$ obtained using a white calibration standard (Labsphere, Spectralon® 5"), after dark counts subtraction $D(x,y,\lambda)$ and by weighting the latter two datasets for the ratios of their corresponding integration times t of the camera used during the acquisition. The formula for the reconstruction of the reflectance hypercubes is the following:

$$R(x,y,\lambda) = \frac{I(x,y,\lambda) - \frac{t_I}{t_D} D(x,y,\lambda)}{\frac{t_I}{t_W} W(x,y,\lambda) - \frac{t_I}{t_D} D(x,y,\lambda)} \tag{2.12}$$

where t_I, t_D and t_W are the camera integration times for each frame of the intensity, dark and white hypercubes, respectively.

2.6.2 Spectral unmixing analysis

The present thesis work featured a research period at the TranslaTUM research group, Technical University of Munich, Germany. The objective was to collaborate with Dr. Ezhov and Prof. Rueckert on developing a rapid spectral unmixing technique based on the modified Beer-Lambert law (MBLL). This innovative approach aims to differentiate the molecular composition of glioma biopsies effectively, enhancing the understanding of the pathological characteristics present in the samples, as described in Ezhov et al [34,65]. This method seeks to address the computational time constraints of current approaches by introducing a data-driven technique that substantially accelerates the inference of biochemical composition [34]. The core of the approach lies in predicting concentration changes based on spectral variations, leveraging the MBLL (Eq. 1.7), and applying a traditional least squares minimization to align the observed changes with the actual reflectance spectrum. During optimization, the resulting concentration differences, along with the corresponding absorbance changes, are used to generate training samples for a neural network. A multi-layer perceptron (MLP) network was employed for training, with the input being a one-dimensional vector representing attenuation

differences and the output being the predicted molecular concentration shifts. For the nonlinear least-squares optimization involved in MBLL (including scattering), the SciPy library's publicly available solver was utilized [34,65]. Finally, the results derived from the least-squares minimization process were treated as the ground truth to validate the trained neural networks [34].

As reported in Ezhov et al., [34] it takes ca. 0.7 ms for the network to infer biochemical composition for 10^5 spectra on NVIDIA GeForce MX450 with 2048 MiB.

In this study, the pathological differences were quantified with respect to sample S1, using the average spectral reflectance of the central area of the sample as baseline spectrum.

The inferred compositions for two different scenarios were then compared: (1) by fitting the whole measured wavelength range (from 510 nm to 900 nm), and (2) by fitting only the NIR portion of the available spectrum (in this case, from 740 nm to 900 nm). For the latter, the expected major absorbing chromophores are oxygenated (HbO_2) and deoxygenated (HHb) hemoglobin, the oxidized (oxCCO) and reduced (redCCO) forms of cytochrome-c-oxidase (CCO), as well as water and lipids [31,62,66]. The spectral signatures of the chromophores targeted by the analysis are depicted in Figure 2.16.

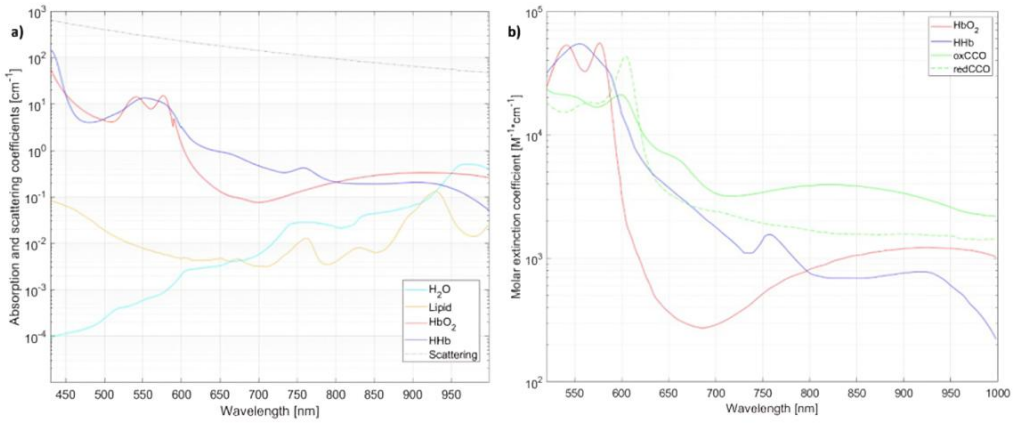

Fig. 2.16: a) Absorption coefficients for HbO_2, HHb, lipids and water, and scattering coefficient of generic brain tissue in the visible and NIR range (150 g/L concentration of Hb in blood and blood volume content in generic brain tissue equal to 5% are assumed) [26,33]; b) molar extinction coefficients of HbO_2, HHb, oxCCO and redCCO in the visible and NIR range [26,32].

In the visible range, the presence of additional chromophores was assumed, specifically the oxidized and reduced forms of cytochrome-B (Cyt-B) and cytochrome-C (Cyt-C), due to their involvement in the metabolic processes [66]. The inferred compositions, in the forms of either concentrations or volumetric contents, are in units [mM/cm] and [cm^{-1}], respectively, as unitary pathlength (1 cm) were used in the experiments. It was previously seen that a quasi-constant pathlength only effectively scales the concentrations, at least in the NIR range [34], and is therefore sufficient for the preliminary task of attempting to distinguish biopsies of different tumour gradings.

2.7 Results of the analysis of glioma biopsies

A qualitative assessment has been performed for a comparative analysis of HyperProbe1 data, with the aim to discern patterns or anomalies within the tissue samples [16]. On the quantitative side, a detailed spectral analysis was conducted using spectral unmixing techniques [16], providing insights on the biochemical changes occurring in the tissue The following paragraphs comprehensively describe both analyses.

2.7.1 Qualitative and comparative evaluation of the HyperProbe1 data

Preliminary qualitative evaluation of the data collected with HyperProbe1 on the cerebral *ex vivo* tissue was performed, to assess both heterogeneity in the spectra within the same sample, as well as spectral variability between all the biopsies. For intercomparison across the various samples described in Table 2.6, each processed reflectance hypercube $R(x, y, \lambda)_n$, for n = S1…S11, was averaged spatially over its entire FOV, in order to obtain a single averaged reflectance spectrum for each biopsy, and the standard deviation of the average was calculated. All these reflectance spectra, along to their standard deviations, are shown altogether in Figure 2.17:

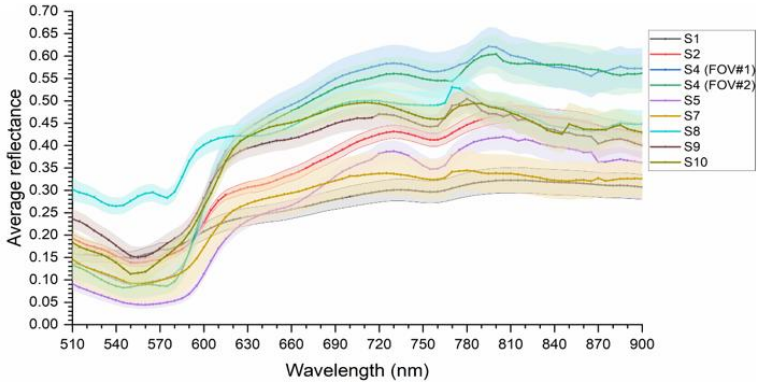

Fig. 2.17: Intercomparison of averaged reflectance spectra over the entire imaged FOVs of each biopsy sample. The coloured shadows represent the standard deviations, associated with the average reflectance.

Overall, the average reflectance spectra between samples share similar trends, reporting low reflectance in the visible range (where absorption from hemoglobin is at its highest, as per **Fig. 2.16a**), which then tends to increase gradually towards the NIR range beyond 600 nm, where scattering becomes predominant. However, significant variability in both magnitudes of the spectra in the same regions and in their local features are also present, differentiating the signatures of the various samples.

A number of different regions of interest (ROI) were selected on the reflectance hypercubes $R(x,y,\lambda)$ to calculate average reflectance spectra, including different sizes and portions of the FOV reporting identifiable visual features, such as blood clusters. This was done to investigate potential spatial changes in the reflectance spectra across the FOV of the samples. Figure 2.18a shows an example of a single, processed reflectance spectral image (as described in **Sec. 2.6.1**) collected with HyperProbe1 for an arbitrary high-grade (WHO grade 4) sample S2, at the bandwidth centred at 560 nm, whereas Figure 2.18b depicts the corresponding average reflectance spectra. Additionally, for a more direct comparison between the spectral signatures of the biopsies reconstructed with HyperProbe1 and the pure optical signatures of the chromophores of interest reported in **Fig. 2.16**, attenuation spectra $A(x,y,\lambda)$, associated with the contribution of optical absorption and scattering in the tissues, were then calculated from the reflectance spectra $R(x,y,\lambda)$ in the same ROIs of the samples, using the formula: $A(x,y,\lambda) =$

$-\log_{10}(R(x,y,\lambda))$. Figure 2.18c reports the average attenuation spectra of the same high-grade sample S2 and the previously selected ROIs.

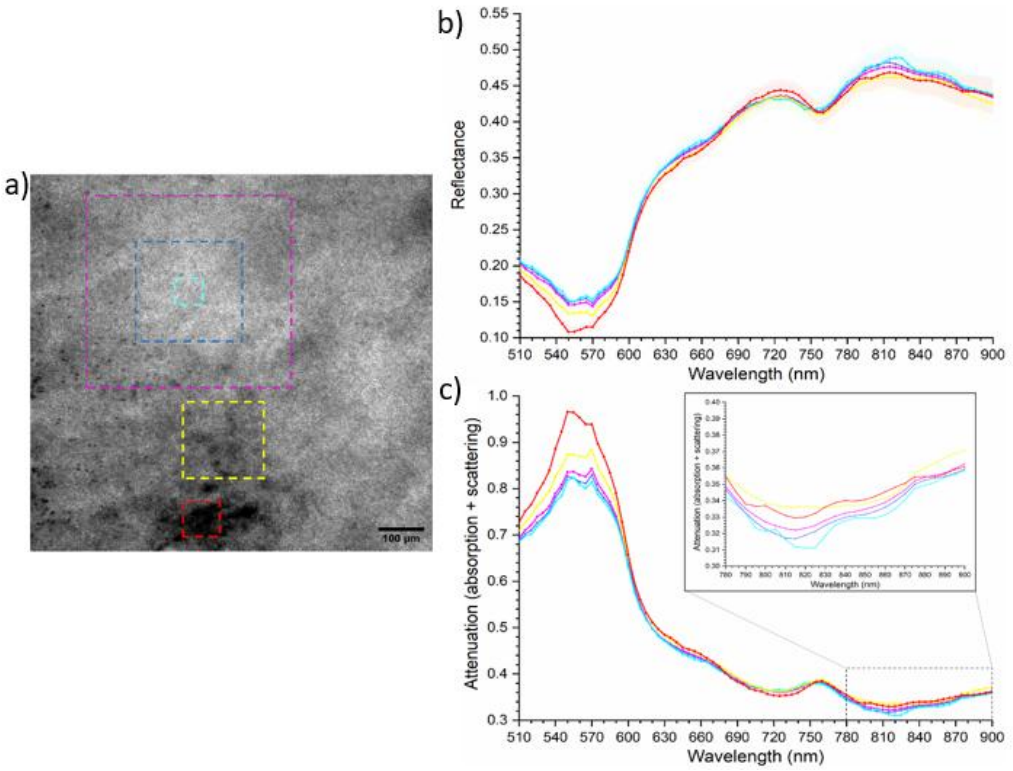

Fig. 2.18: a) Processed spectral image from HyperProbe1, at 560 nm, of high-grade (WHO grade IV) biopsy sample S2, with highlighted, selected ROIs in the FOV in which average reflectance spectra were calculated; (b) Example of average reflectance spectra in the corresponding ROIs of the biopsy sample S2; (c) Example of average attenuation spectra in different ROIs of biopsy sample S2, with the portion within the NIR range 780-900 nm enlarged.

The comparison of the reflectance spectra for each sample on different ROIs highlights significant (from 0.0017 to 0.0378 average root mean square deviation (RSMD) for the reflectance curves across all samples) differences in their shapes and trends, as visible for the model case of S2 in **Fig. 2.18**, for two specific spectral ranges: (1) between 510 and 660 nm, and (2) between 780 and 880 nm. In contrast, outside of these ranges, the remainder of the spectral signatures displays homogeneous distribution of the optical properties of the *ex vivo* samples across the entire FOVs. The largest differences (0.0378 of average RSMD across samples) are reported for the ROIs where accumulation of blood is clearly visible. For the first mentioned range (510-600 nm), such result could be correlated to the presence and

strong influence of the visible peaks of hemoglobin absorption (**Fig. 2.16a**). The influence of the absorption of hemoglobin could also be connected to the reported differences in the spectra for the second mentioned range (780-880 nm), which is characterized by a broad peak of absorption from HbO_2. However, differences were identified in the biopsy samples also for ROIs not including visible blood clusters: this could then be connected to local differences in the concentrations of CCO, as the identified range overlaps with the NIR absorption peak of the latter (**Fig. 2.16b**), as well as for the increasing weight of the absorption of water and lipids towards the end of the NIR range (**Fig. 2.16a**).

Regarding the attenuation data, in the range 510-600 nm the attenuation spectra of the brain tissue samples correlate with the combined profiles of the absorption spectra of HbO_2 and HHb, with noticeable peaks at around 545-555 nm and at 575 nm. Another peak is also identified in all samples at around 755-760 nm, overlapping the equivalent one from the absorption spectra of HHb. In all samples, attenuation in the range 510-600 nm is reported to increase gradually when moving from ROIs with no visible accumulations of blood towards ROIs that includes the latter primarily to completely (as visible for the case of S2 in **Fig. 2.18c**. The latter figure highlights and enhances the visualization of the attenuation spectra from S2 in the range between 780 and 900 nm, where differences are reported for all the ROIs regardless of the presence of any discernible spatial features or differences in contrast. This phenomenon is reported largely across all the analyzed samples of surgical biopsies. In particular, localized peaks of attenuation corresponding to about 840 nm are identified in a number of ROIs in the samples, where the optical absorption of oxCCO is also at its highest. The reported discrepancies among concentric ROIs of different sizes in relatively homogenous areas of the *ex vivo* tissue could be linked to either local variation in the abovementioned chromophore, as suggested by the overlapping of the peaks, or to partial volume effects connected to changes in the optical pathlength travelled by the lights within the sampled regions.

For a further in-depth analysis of the biopsy data, the abovementioned reflectance spectra have been averaged according to their 2021 WHO grading: lower grade glioma (LGG) samples (WHO grade 2 and 3) were grouped together and the mean

of their average reflectance spectra across the whole FOVs was compared against the same mean for all the higher grade glioma (HGG) samples (WHO grade 4), as reported in Figure 2.19. The decision for this grouping is according to the most recent (2021) WHO grading [42] and current state-of-the-art in histopathological practice [67], where gliomas are grouped molecularly based on their isocitrate dehydrogenase (IDH) and 1p/19q status, so that grade 4 glioblastomas (IDH-wildtype) are defined as higher grade and clearly separated from the biologically and clinically more benign IDH-mutant, and 1p/19q-codeleted, lower grade gliomas (defined as WHO grades 2 and 3). Differences in the means between LGG and HGG samples are indeed visible, regarding both local spectral trends as well as magnitude. However, statistical analysis via Mann-Whitney U-Test was performed on the grouped means, obtaining p-values for each measured wavelength all equal or higher than 0.26 (as reported in **Fig. 2.19**), which indicates that there is no single independent wavelength that can distinguish tumor grading (thus supporting the hypothesis of performing spectral unmixing).

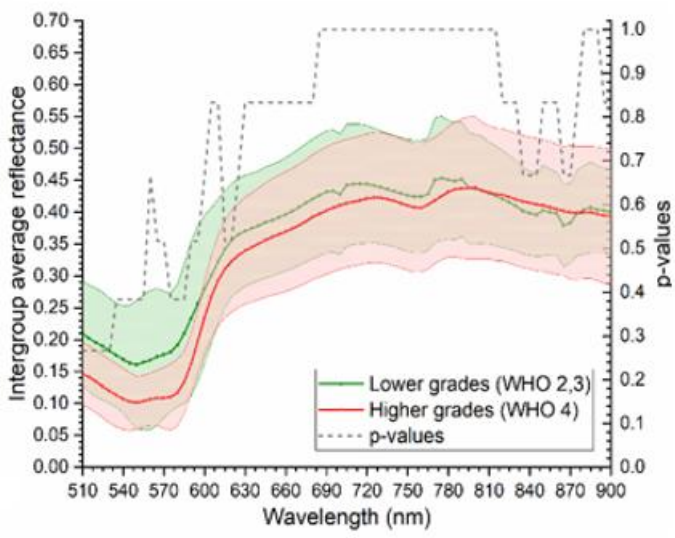

Fig. 2.19: Comparison between average reflectance spectra grouping LGG (WHO 2, 3) against HGG samples (WHO 4), with resulting p-values from statistical analysis on differences between each wavelength.

2.7.2 Quantitative biochemical analysis of the HyperProbe1 data with spectral unmixing

As mentioned in **Sec. 2.6.2**, the inferred compositions of the expected chromophores from the spectral unmixing algorithm in all the biopsy sample have been compared for two different fitting scenarios: in the whole range from 510 nm to 900 nm, and in the NIR portion of the spectrum from 740 nm to 900 nm. For the first scenario, satisfactory spectral fits were obtained, matching the measured attenuation: an example is depicted in Figure 2.20a and Figure 2.20b, for HGG sample S4 in FOV#1 (WHO grade 4) and LGG sample S10 (WHO grade 2), showing also the reconstructed quantitative maps for the total concentration of hemoglobin (HbT), given as the sum of HbO_2 and HHb, as well as for the concentration of differential CCO (diffCCO), given as the difference between the concentrations of oxCCO and redCCO [62,66].

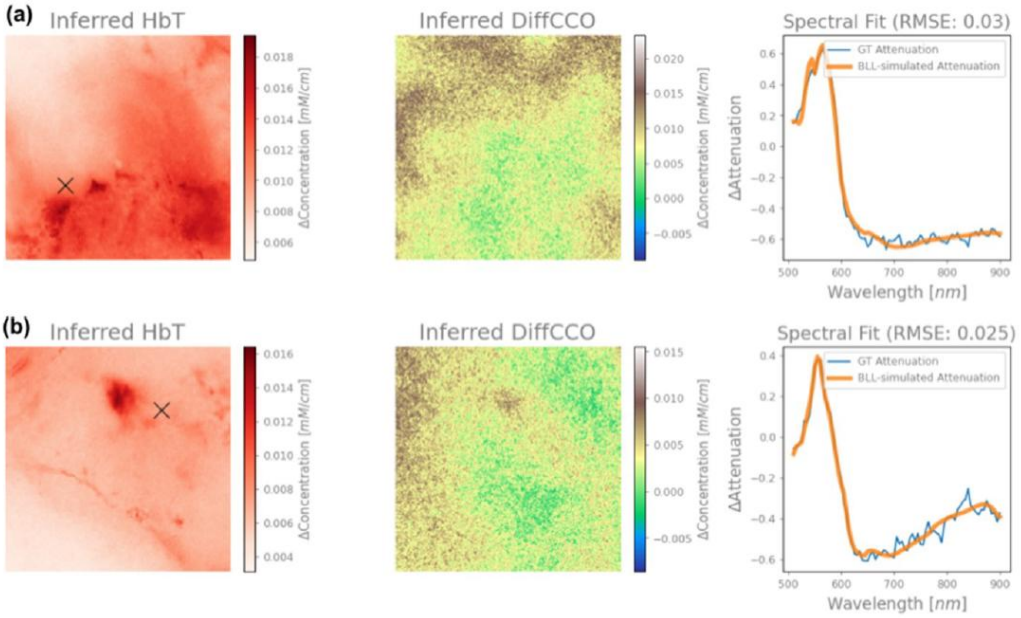

Fig. 2.20: Inferred HbT and diffCCO concentration maps of HGG S4 FOV#1 (a) and LGG S10 (b) samples fitting the whole measured wavelength spectrum (510-900 nm), whilst a model fitting of the observed attenuation for the marked pixel in the HbT image is shown in the third column for both biopsies.

Blood clusters are resolved with high resolution, due to the hemoglobin peaks in the 500-600 nm range and the expected high concentration and absorbance of hemoglobin (compared to the other known chromophores). Similar well-matching spectral fits via the MBLL are found across all patients, as the root mean square

error (RMSE) means across all pixels and across all patients are reported to be in the range 0.017 to 0.039, which is of similar magnitude to the exemplary RMSEs reported in the **Fig. 2.20**.

A preliminary attempt to classify the biopsy samples from the inferred hyperspectral results was also performed. As shown in Figure 2.21a and 2.21b reported below, it has been found that predicted lipids content allows to separate LGG (grade 2 and 3) biopsies from HGG biopsies (grade 4).

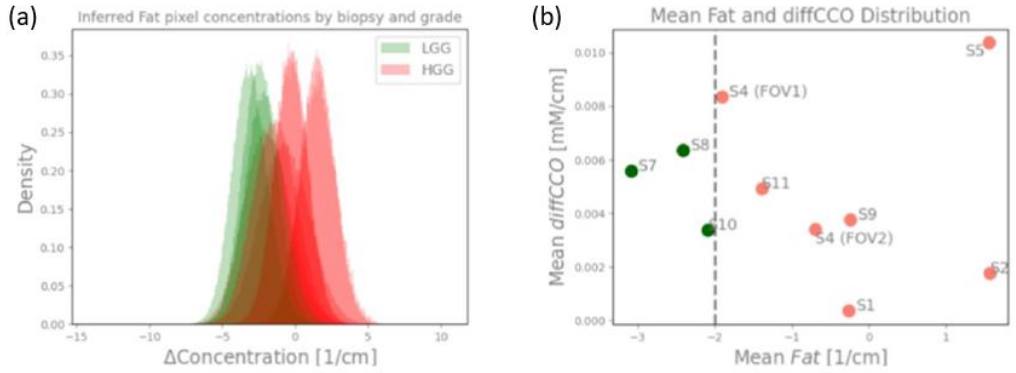

Fig. 2.21: a) Histogram showing probability density distribution of inferred lipid volumetric content of each pixel across different LGG (displayed in green) and HGG (displayed in red) grade samples; b) distribution means of the lipid content (reported on x-axis) and diffCCO concentrations (reported on y-axis) suggest that lipid mean content could be able to distinguish grading of all samples, whereas no apparent separation is visible for the inferred mean diffCCO concentrations.

Even though significant overlap is observed between the different distributions (with an overlap coefficient of 49.96% assuming normal distributions), a general trend of higher differential lipids content in HGG biopsies can be noticed, with a mean of -0.466 cm^{-1}. Conversely, the LGG samples were found to have a mean lipid content of -2.53 cm^{-1}. Conversely, CCO or hemoglobin (established biomarkers for cellular metabolism and hemodynamics, respectively [62]) were found to be unable to separate gradings of glioma samples in the whole range 510-900 nm (as shown in **Fig. 2.21b**, for CCO). The overlap coefficient between LGG and HGG samples was found to be considerably larger, with 81.2% and 84.6% for inferred diffCCO and HbO_2 concentrations, and statistical differences in grading were not observed. On a final note, as seen on **Fig. 2.21b**, by considering both variables (lipid content and diffCCO concentration) on the 2D distribution plot, an oblique line could even

better separate the two glioma grades. A larger sample size will be required to test such more complex hypotheses further.

In the second scenario, compositions within the biopsy samples were estimated using exclusively the NIR range between 740 nm and 900 nm, which was chosen to target chromophores that are known for their characteristic absorption profiles in such range, particularly oxCCO and redCCO (as seen in **Fig. 2.16**). Indeed, MBLL has been commonly employed in this specific NIR range to infer differences in metabolic activity using CCO as a biomarker [62,66]. As shown in Figure 2.22, the observed signal was again fitted qualitatively well: the inter-biopsy mean RMSE errors are found to be in the range 0.0151 to 0.296, i.e., the spectral fits of all biopsies can be expected to be similar as for the previous scenario, albeit being slightly worse due to the expected reduction in SNR at the latter end of the measured spectrum, where scattering of light becomes predominant.

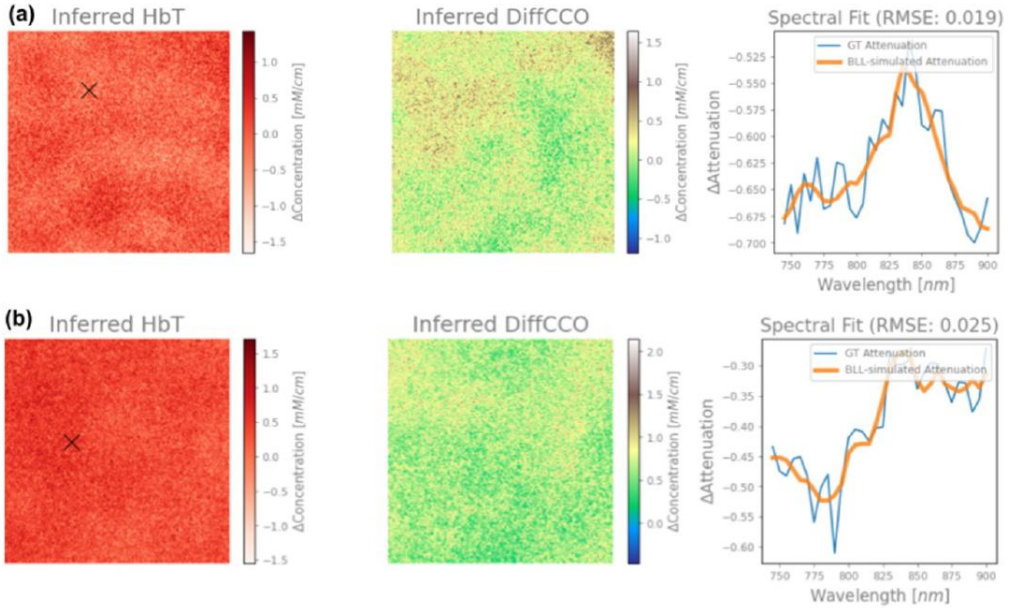

Fig. 2.22: Inferred HbT and diffCCO concentration maps of HGG S4 FOV#1 (a) and LGG S10 (b) samples fitting exclusively the NIR range (740-900 nm), whilst a model fitting of the observed attenuation for the marked pixel in the HbT image is shown in the third column for both biopsies.

Notable loss in the resolution of various blood clusters can be observed, which was also expected due to the exclusion of the 510-600 nm range with larger hemoglobin absorption peaks. Interestingly, there are significant differences in the inferred

molecular concentrations across biopsies of LGG and HGG that do not match the ones highlighted by the spectral analysis on the whole wavelength range: e.g., in this scenario, the inferred lipid contents were not able to distinguish between the different grades of the samples. An overlap coefficient of 77.1% was reported and no statistical differences in the concentration means for lipids were found. However, average concentrations differences of metabolic diffCCO between LGG and HGG samples were observed, with HGG samples showing lower diffCCO mean concentrations, as seen in Figure 2.23:

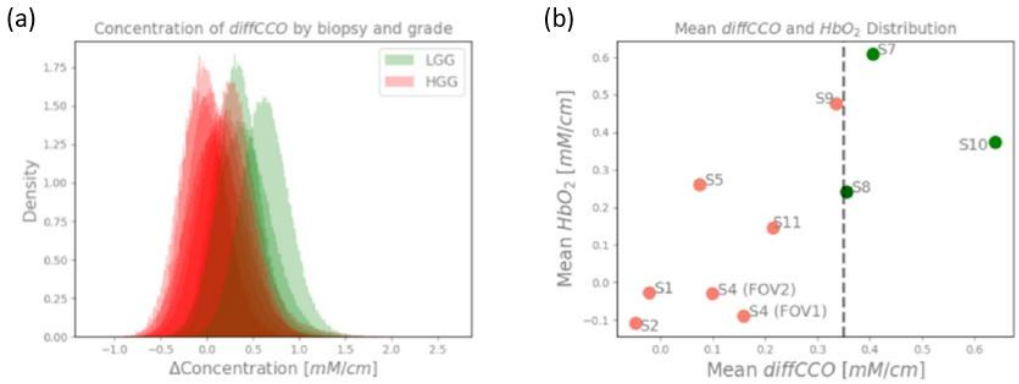

Fig. 2.23: a) Histogram showing probability density distribution of inferred diffCCO concentrations of each pixel across different LGG (displayed in green) and HGG (displayed in red) grade samples; (b) Distribution means of diffCCO and HbO_2 concentrations suggest that these parameters could be able together to distinguish lower and higher-grade samples of glioma tissue, with diffCCO being the most accurate, across all the investigated samples.

Furthermore, as depicted in **Fig. 2.23b**, an approximately linear correlation in the 2D domain between the mean differences in concentration of diffCCO and those of HbO_2 is shown: together with a reduced diffCCO mean concentration, HGG samples also present a correlated reduction in the mean concentration of HbO_2, with the combination of the two biomarkers enhancing the possibility of separating samples grading more effectively. However, it has been observed that the HGG sample S9 displays diffCCO characteristics close to LGG samples (**Fig. 2.23b**): an explanation might be that there could be different (possibly concurrent) reasons for this low distinguishability. Even though it has not been demonstrated that HGG samples can show characteristics of LGG samples, the opposite (i.e., high grade-typical histological characteristics in low grade lesions) has recently been reported

by Motomura et al [68]. Thus, in general, we suggest that it might be possible that lower grade lesions could display characteristics of higher grade lesions, although further investigation on this would be needed.

On a final note, a further analysis demonstrated that both oxCCO and redCCO individually are seemingly not able to distinguish biopsy grading, as overlap coefficients of 84.6% and 73.3% were found, and no statistically significant differences were present. This is shown in Figure 2.24 plotting probability density distributions of each pixel across all biopsies, divided between LGG and HGG.

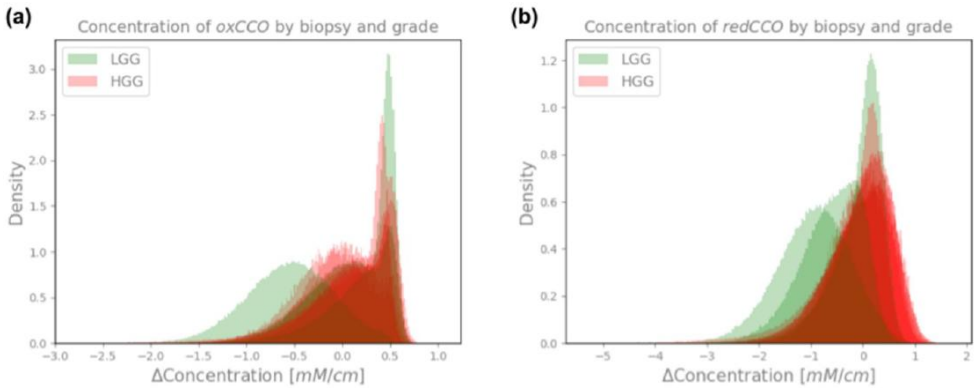

Fig. 2.24: Histogram showing probability density distribution of inferred oxCCO (a) and redCCO (b) concentrations of each pixel across different LGG (displayed in green) and HGG (displayed in red) grade samples. Neither the inferred oxCCO and redCCO density distributions using the NIR range (740-900 nm) suggest being able to differentiate tumor grading.

2.8 Conclusion and summary of the HyperProbe project

A novel, transportable HSI device has been presented, based on fast spectral scanning via a combination of SCL illumination and AOTF filtering. At full operational performances, HyperProbe1 can scan sequentially up to 79 wavelengths between 510 and 900 nm, with 5-nm sampling and high spectral resolution (3.5-7 nm of bandwidth), as well as acquire corresponding spectral images on a 0.9 x 0.9 cm^2 FOV at high spatial resolution (4.38 μm), in less than 5 minutes. Furthermore, we also provided a preliminary assessment of the data acquired and analyzed with HyperProbe1 on a number (n = 11) of fresh surgical samples of glioma from patients at different WHO gradings, including both lower grade (WHO grades 2 and 3) and higher grades (WHO grade 4) tumors. The initial findings demonstrated the capability of the device to reconstruct quantitative maps of the distribution of the

concentrations of various chromophores of interest, in particular hemoglobin and CCO (both established biomarkers for tissue hemodynamics and metabolism, respectively), as well as lipid volumetric content. Differences in the inferred contributions of these biomolecules between LGG and HGG biopsies have been analyzed, suggesting a way to distinguish between the two, and thus potentially providing the basis for a HSI-based methodology for tumor classification. The present study has also highlighted significant differences between mean lipid contents across samples that could potentially be used to distinguish tumor grading, when fitting over the entire work range (510-900 nm). In particular, HGGs presented higher mean lipid content than LGGs: a plausible biological interpretation of this could be connected to a substantial lipid storage for lipid metabolism in higher grade gliomas, a known characteristic feature of GBM [69,70].

Similarly, this work has additionally demonstrated that the analyzed HGGs presented inferior concentrations of diffCCO compared to LGGs, when fitting the data exclusively in the NIR range (740-900 nm): this may suggest a potential metabolic path with NIR light to distinguish lower and higher grade samples. This finding may also emphasize the potential role of diffCCO in providing metabolic differences that lies beyond its critical use in NIR spectroscopy (NIRS) applications [66]. The exact mechanisms by which these concentration differences in diffCCO arise remain uncertain: as changes in the concentration of diffCCO are directly proportional to variations in the metabolic activity of the tissue, one would expect an influence of enhanced hypermetabolism in tumors at higher grades. However, HGGs (such as GBMs) are characterized by the unique presence of necrotic tissue as the core part of the lesion, with the hypermetabolic region occurring only at the borders [71,72]. Such central necrotic areas, composed almost entirely of dead -i.e., ametabolic- cells could explain the overall reduced mean concentration of diffCCO in HGG compared to LGG, which instead do not present necrosis. Furthermore, the results showed a direct correlation between the reduction of diffCCO in HGG with a corresponding decrease in HbO_2, which could also be connected to the hypoxic microenvironment that is specific to this type of brain tumor [73,74]. From a biological perspective, HGGs, such as GBMs, are known to be triggered and driven in their proliferation by hypoxic microenvironments within the cerebral tissue [73,74]. Such

phenomenon could explain the reduced mean concentration of HbO_2, which is a biomarker for oxygenation of the brain, and its correlation with the diffCCO, since a direct association between oxygen delivery and its metabolic consumption has been strongly established [75]. Future investigations on a larger and enriched cohort of biopsy samples of various types will be needed to further confirm all these results on a more robust statistical basis. In particular, comparisons with control samples composed of healthy cerebral tissue will also be strongly required for increasing the accuracy and reliability of any prediction.

Summing up, the goal of HyperProbe1 is to provide a first proof-of-concept application to rapid and quantitative digital histology of *ex vivo* tissue from excised surgical biopsies, focusing on cerebral glioma, by reconstructing quantitative maps of the distributions of chromophores of interest in the tissue via fast spectral unmixing algorithms. In this perspective, it has been demonstrated that HyperProbe1 can collect and analyze full-range HSI data of light reflectance from surgical biopsies in less than 1 hour after their excision (including preparation of the sample and setting up of the measurements), a significantly much faster time than traditional H&E histopathological screening, which normally takes several days up to few weeks. Such result qualifies HyperProbe1 for an envisioned, future utilization providing *in situ*, streamlined, and non-destructive screening of fresh tissue samples, ideally within or just next to the operating theatre. This application could considerably benefit the outcome of the surgical treatment and provide an all-optical advancement to current post-surgical histopathological practice.

The versatility of HyperProbe1 could also pave the way for potential applications of the instrumentation to virtually any types of surgical and non-surgical biopsy (or other *ex vivo* tissues), as well as even move beyond digital histopathology. In this perspective, HyperProbe1 can also be envisioned as an investigative, high-performance HSI device for preclinical *in vivo* applications: it could be used to explore and tailor features of HSI (such as type and number of wavelengths) that could be translated into clinical settings by specifically engineering more compact, cost-effective and user-friendly medical devices. Within the framework of the HyperProbe project and consortium [61], the goal is indeed the translation of this technology for its use as a new neuronavigational tool during brain surgery, such as

in glioma resection. Such a device would aim at providing an innovative approach to guided neurosurgery, by transforming current practice towards an all-optical, real-time, quantitative and accurate imaging approach, that could significantly help neurosurgeons, enhance the efficacy of the treatment, and ultimately improve life expectancy of the patients.

Chapter 3: Multispectral Imaging

This chapter addresses the issue of chronic skin ulcers and describes in detail the technical features of an innovative multispectral imaging (MSI) device, called MultiSmart. This device is designed to monitor chronic skin lesions *in vivo* using quantitative parameters, enabling more precise monitoring and early diagnosis. The aim of MultiSmart is to reduce amputation rates and achieve successful healing outcomes through improved diagnostic accuracy and continuous assessment of wound status.

The portable MSI device has been designed to be used in a quick, non-invasive manner, with simple and easy-friendly functionality, at a cost-effective value. The first step towards an extraction of quantitative data is the calibration of the system. For this task, liquid optical phantoms composed of known concentrations of water, intralipid (IL), human blood and oxygen have been used. Liquid optical phantoms are widely used for the calibration procedures of novel spectroscopic systems thanks to their easy fabrication, availability of materials, and their ability to mimic the properties of biological tissues [76]. Data obtained from the analysis of the optical phantoms are then utilized to construct look-up tables (LUTs), which gather all possible reflectance values with the corresponding concentrations of blood and oxygen. Afterwards, the development of a cross-check algorithm is described, with the aim to find the LUT reflectance value that is closest to each pixel in the patient's reflectance image. An example of the final results obtained on chronic ulcers of two patients is shown in the final paragraph. Sections and figures of the journal article in [77] by M. Marradi et al have been modified and adapted to form parts of this chapter, with reprint permission under CC BY 4.0 License.

3.1 Multispectral imaging for chronic skin ulcers

Chronic skin ulcers are a significant medical issue characterized by lesions that show no tendency to heal after three or more months. These ulcers are commonly associated with symptoms such as pain, swelling, foul odor, bleeding, discharge, and reduced mobility, which lead to substantial emotional and physical distress for patients. In the most severe cases, chronic non-healing wounds can result in severe outcomes, including limb amputation and premature death. The increasing

percentage of elderly individuals and the prevalence of conditions like obesity and diabetes suggest that the burden of chronic ulcers will continue to rise in the near future [77]. Chronic skin ulcers can result from various underlying conditions, including venous insufficiency, arterial insufficiency, diabetes mellitus, and pressure injuries. Venous ulcers, which are caused by chronic venous insufficiency, are the most common type of leg ulcer, accounting for approximately 70% of cases [78]. Diabetic foot ulcers are another major type, affecting up to 25% of diabetic patients during their lifetime [79]. Pressure ulcers, often referred to as bedsores, are caused by prolonged pressure on the skin, typically affecting individuals with limited mobility.

The management of chronic wounds incurs substantial costs due to the need for frequent medical consultations, advanced dressings, and sometimes surgical interventions. In Europe, the estimated healthcare annual cost for treating chronic wounds is estimated to be billions of euros [80]. Additionally, the indirect costs related to chronic ulcers include loss of productivity due to prolonged recovery periods, absenteeism, and early retirement. Patients often require long-term care, which can lead to significant economic losses both for the individuals and the broader economy. The burden of caregiving also places economic pressure on families and caregivers. Addressing these burdens requires a comprehensive approach that includes early detection, advanced treatment options, and robust support for affected individuals and their caregivers. New preventive and monitoring technologies are needed, but the innovation in new therapies and diagnostic tools is impaired due to the lack of knowledge regarding the biological processes of wound healing and to the uncoordinated approach by medical staff [81]. For an early detection of the tissue health status and successful treatment guidance, a solution may be the design of an innovative, non-invasive healing monitoring system, based on multispectral imaging (MSI).

MSI is an emerging imaging technology that uses light in the visible and NIR portion of the spectrum. When biological tissues are invested by light, the latter undergoes multiple scattering and is absorbed for the most part by hemoglobin, water, fat, and melanin, thanks to which quantitative/qualitative information regarding the tissue pathology can be extracted and inferred [82]. MSI works similarly

to HSI (explained in Chapter 2), except that a limited number of wavelength bands are sampled (typically up to ten). This number is lower than the one used for HSI, giving the advantage of a less complex and more cost-effective instrumentation. MSI may be used as a diagnostic tool in biomedical imaging thanks to its monitoring capabilities for chromophores contained in the blood, including oxyhemoglobin and deoxyhemoglobin. These important chromophores provide information about the local degree of oxygenation, perfusion, and the microcirculatory status of the analyzed tissue region [82]. Currently, there are other existing methods used for the evaluation of these characteristic parameters in the wound: ankle-brachial index (ABI), Doppler ultrasound, and transcutaneous oxygen partial pressure (TcPO2). Unfortunately, these techniques are not applicable for all kinds of patients and present some limitations. For example, ABI is not indicated for patients with diabetes, renal failure, and advanced age; in addition to this, it provides indirect information on arterial dysfunction and is unable to localize the disease [83]. Doppler ultrasound is an old-fashioned technique, no longer routinely used in modern clinics and that should be combined with other imaging tools [83]. Lastly, the reliability of TcPO2 is strongly debated: this technique measures the local oxygen released from the capillaries through the skin, reflecting the metabolic state of the lower limb. Its use is restricted because the procedure is lengthy (taking about 45 minutes to evaluate a wound) and the results provided are inaccurate, with low reproducibility and accuracy [84].

Other competitive optical technologies in wound healing monitoring, such as thermal imaging, optical coherence tomography (OCT), spatial frequency domain imaging (SFDI), fluorescence imaging and NIRS, offer unique advantages and limitations; for example, thermal imaging has been widely used in wound healing monitoring due to its ability to non-invasively assess skin temperature variations, which are indicative of underlying blood flow and inflammation [85]. This technique is particularly useful in detecting early signs of infection or ischemia in wounds, as elevated temperatures often correspond to inflammation, while cooler areas may indicate reduced perfusion [85]. Despite its simplicity and portability, thermal imaging lacks specificity in differentiating between various tissue types and cannot provide

direct biochemical information about the wound bed, making it a complementary rather than standalone technique.

OCT has gained increasing attention in wound healing research due to its ability to provide non-invasive, high-resolution, cross-sectional images of tissue microstructure. One of the primary strengths of OCT lies in its capacity to monitor epithelialization [86], a critical phase in wound healing where new epithelial cells form to cover the wound surface. The technique allows clinicians and researchers to track the progression of epithelialization in real time [86], offering valuable insights into the effectiveness of therapeutic interventions. Furthermore, OCT has proven highly effective in evaluating scar formation, as it can detect alterations in dermal and subdermal layers associated with fibrotic processes [86]. These capabilities make OCT a powerful tool for assessing wound morphology and guiding clinical decision-making. In addition to monitoring epithelialization and scarring, OCT has been used to evaluate wound bed characteristics such as tissue hydration and the integrity of wound edges [87]. It is particularly useful in chronic wound management, where it can help differentiate between healing and non-healing wounds by identifying structural abnormalities. OCT has also been employed to assess tissue responses to treatments, such as the effects of advanced dressings, negative pressure wound therapy, and skin grafts, providing a quantitative basis for optimizing therapeutic strategies [86]. Despite these advantages, OCT has notable limitations, as it does not directly provide biochemical information, such as oxygenation levels or molecular composition, which are often key indicators of wound viability. To address these gaps, OCT is frequently combined with complementary techniques, such as near-infrared spectroscopy NIRS, which measures oxygenation levels in tissue, making it particularly useful for assessing perfusion and vascular health in the wound bed [88]. Advances in NIRS technology have led to the development of portable and user-friendly devices that provide real-time feedback to clinicians [88].

SFDI is another emerging technology that quantifies tissue optical properties such as absorption and scattering coefficients over a large FOV. This technique enables the assessment of tissue oxygenation and hemoglobin content [89], making it particularly relevant for wound healing studies. However, SFDI systems are often bulky and complex, which limits their integration into clinical workflows [89].

Finally, fluorescence imaging is widely employed in wound care for its ability to highlight specific biochemical markers using fluorophores. Techniques such as autofluorescence imaging can assess the metabolic state of tissues by capturing signals from endogenous fluorophores like NADH and FAD [90], or from bacterial loads that may hinder the healing process [91]. Exogenous contrast agents are also utilized to enable targeted imaging of specific structures or molecules [92]. Although fluorescence imaging provides excellent sensitivity and specificity, it is limited by the need for external agents, potential photobleaching, and restricted depth penetration [93]. These limitations make it less ideal for assessing deep wounds.

By comparing these competitive technologies, MSI stands out for its ability to non-invasively capture both spectral and spatial information, allowing for a detailed analysis of wound bed characteristics such as blood volume fraction (BVF), oxygenation levels, and tissue viability. MSI provides a balanced combination of biochemical and morphological insights without requiring exogenous agents or invasive procedures. However, MSI also faces challenges, such as standardization of imaging protocols and motion artifacts, which need to be addressed to enhance its clinical utility.

In an attempt to find a solution to these issues and to tackle the challenges associated with chronic skin ulcers, this study introduces the use of a novel and advanced MSI device. The proposed system aims to enhance the accuracy of monitoring and early diagnosis, thereby reducing the rates of amputation and improving healing outcomes.

3.2 MultiSmart: a novel MSI system for chronic skin ulcer monitoring

In this work, a novel, compact and transportable MSI device, called MultiSmart, based on spectral scanning and diffuse reflectance imaging is going to be presented. The apparatus is composed of light emitting diodes (LEDs) as light sources and a CMOS camera, making it a very compact, manageable, user-friendly, and cost-effective system. The wavelengths of the LED sources, that are located in the visible-NIR portion of the spectrum, have been specifically selected to target and monitor alterations of oxygenation and hemodynamics that can provide biomarkers of monitoring wound healing in chronic ulcers [77]. The calibration of the MSI system

is going to be illustrated, discussing the calibration procedure and the results obtained on patients affected by chronic skin ulcers, in order to assess its efficacy and accuracy.

3.2.1 Description of MultiSmart

The MultiSmart device utilizes LEDs (LUXEON CZ Color Line) as its light sources, operating within the visible to NIR spectrum [77]. LED technology offers several benefits, including high energy efficiency, long lifespan, cost-effectiveness, and instant activation with no warm-up period required [94]. The system features a monochrome CMOS camera (MED ace 2.3 MP 164 mono, Basler) coupled to an objective (Lens C23-1224-5M-P, Basler), which generate a FOV of approximately 15 cm x 25 cm at about 10 cm from the target [77]. In monochrome camera-based systems, each LED is sequentially illuminated, and the camera captures the reflectance image produced by each individual LED. This process creates n-band multispectral images, where n represents the number of LEDs used [94]. In the case of this MSI device, nine LEDs are specifically selected to monitor changes in oxygenation and hemodynamics, providing biomarkers essential for tracking wound healing in chronic ulcers.

The combination of LEDs and a CMOS camera makes the device compact, portable, user-friendly, non-invasive, and capable of rapid and efficient image acquisition. Additionally, the MSI device incorporates polarized filters, one for each LED and another placed in front of the CMOS camera, positioned at a 90° angle relative to the others. This optical arrangement eliminates reflections from the light source caused by specular reflection (linearly polarized light) and ensures that only diffusely reflected light (non-polarized light) reaches the camera. The schematics of the system are reported in Figure 3.1, in addition to the features of the camera reported in Table 3.1:

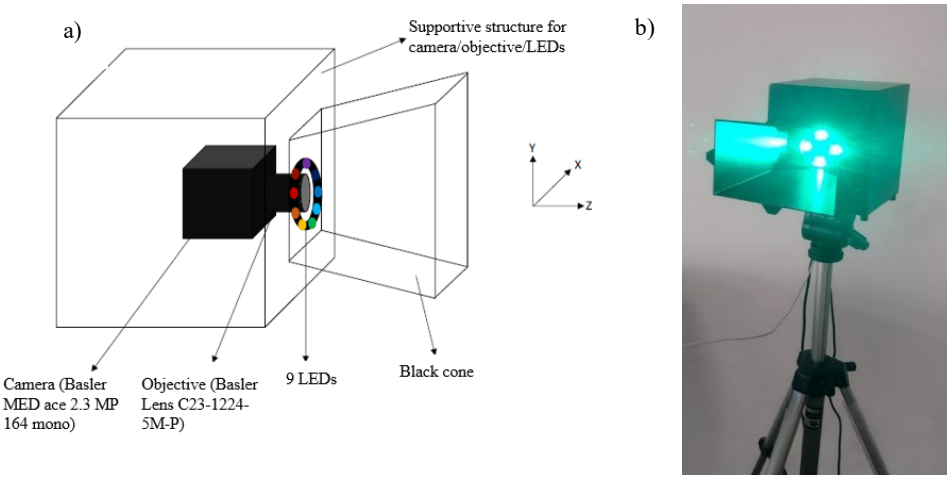

Fig. 3.1: Schematics of the MultiSmart. The main components are reported in a): the camera and its objective, along with the wheel of the nine LEDs and the black cone used to shield against ambient light. All the parts are held together by a black supportive structure. b) Picture of the MultiSmart. The CMOS monochrome camera is positioned at the center, meanwhile the LEDs are mounted around it. The LEDs are covered by polarizing film to exclude specular reflection from the diffuse reflectance images.

CMOS Camera: Basler MED ace 2.3 MP 164 mono	
Pixel area	5.86 µm x 5.86 µm
Resolution	1920 px x 1200 px 2.3 MP
Frames per second	164 fps
Sensor area	11.33 mm x 7.13 mm
Working range	Visible

Table 3.1: Features of the monochrome CMOS camera.

The MultiSmart apparatus can be mounted on a tripod (as shown in **Fig. 3.1b**) or used in a handheld mode, with a handle positioned on the back of the supportive structure for a more flexible use.

3.2.2 Selection of wavelengths for wound healing monitoring and spectral - power characterization

A comprehensive technical study of the spectral characteristics of MultiSmart has been conducted, focusing on the central wavelength emission of each LED, its FWHM and the output power. The spectral data has been acquired using a portable spectrometer (FLAME-T-VIS-NIR-ES, Ocean Optics), meanwhile the power

measurements have been registered using a power meter (PM100D coupled with sensor S120C, Thorlabs). The results are reported in Table 3.2 and Figure. 3.2:

LED	**λ (nm)**	**Standard Error on λ**	**FWHM**	**Standard Error on FWHM**	**Minimum power (mW)**	**Maximum power (mW)**
Violet	424.21	0.05	19.0	0.1	400	458
Royal Blue	451.0	0.2	16.4	0.4	360	432
Blue	485.0	0.2	25.4	0.4	25	34
Cyan	502.0	0.1	28.6	0.3	60	82
Green	524.0	0.3	24.0	0.7	80	119
Amber	598.0	0.2	14.0	0.4	10	16
Orange Red	622.0	0.2	14.1	0.4	25	37
Deep Red	661.0	0.2	12.6	0.4	190	260
Far Red	746.0	0.3	34.6	0.8	150	240

Table 3.2: Wavelengths (λ) of the LEDs and associated standard error, along with the FWHM of each spectral band and its standard error. Minimum and maximum power (mW) reached for each LED.

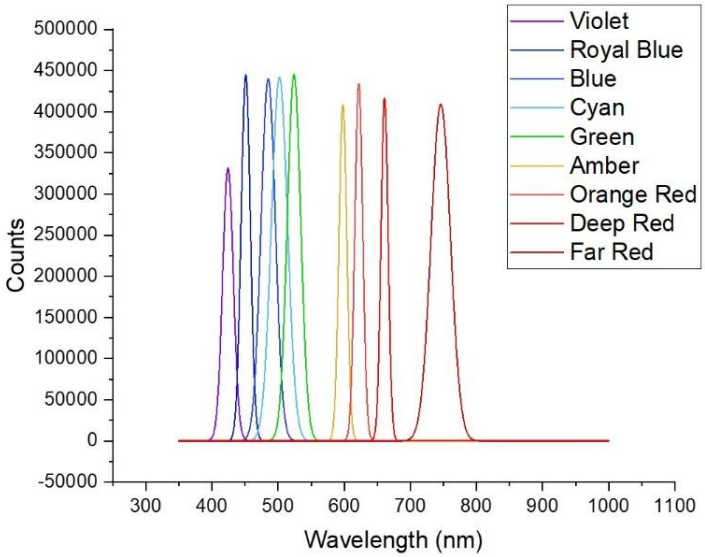

Figure 3.2: Spectral emission of each LED used as light source in the MultiSmart device.

The output power of the LEDs can be regulated, and including the effects of the polarized filters placed in front of them, the power value ranges from 3 to 10 mW per band on the surface of the target.

Fig. 3.2 shows that most of the LEDs (ranging from Violet to Green) cover the spectral region between 400 and 500 nm, where two major peaks of oxy-hemoglobin (HbO_2) and deoxy-hemoglobin (HHb) are present, as illustrated in **Fig. 3.3a**. These LEDs also partially cover the peaks between 500 and 600 nm (Green and Amber) (**Fig. 3.3a**). Although the spectral region beyond 600 nm may initially appear uninteresting and relatively flat, a closer examination (**Fig. 3.3b**) reveals significant differences between the spectra of HbO_2 and HHb, with a notable peak for HHb between 750 and 775 nm. Consequently, LEDs ranging from Orange Red to Far Red were selected to monitor this final region.

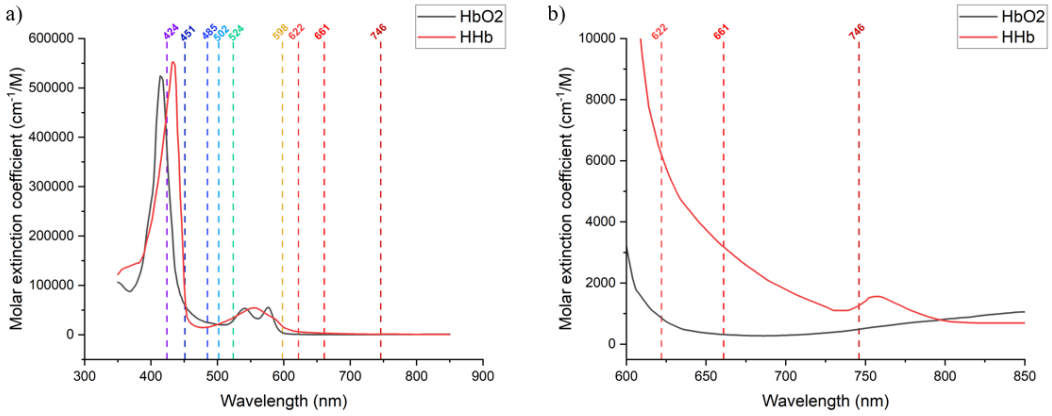

Fig. 3.3: a) Molar extinction coefficient spectra of HbO_2 (black line) and HHb (red line), reported with the central wavelength of each LED (dashed vertical lines). The rich region between 400 – 600 nm is almost entirely covered by the LEDs, from Violet to Amber. b) Close-up of the HbO_2 and HHb spectra between 600 – 850 nm. The LEDs between Orange Red and Far Red have been specifically selected to monitor this portion, targeting also the HHb peak.

3.2.3 Imaging characterization

The imaging capabilities of the MultiSmart system are thoroughly examined in the following paragraphs, with a particular focus on evaluating and quantifying its image quality and performance. Specifically, the assessment covers: (1) the FOV of the MultiSmart; (2) the system's spatial resolution; and (3) image contrast and signal-to-noise ratio (SNR) evaluation.

3.2.3.1 Field of view

The FOV of the MultiSmart was defined using common measuring tape, due to the large size of the acquired scene. The tape features 1 mm-distanced ticks and was illuminated with the 424 nm LED. The result is reported in Figure 3.4:

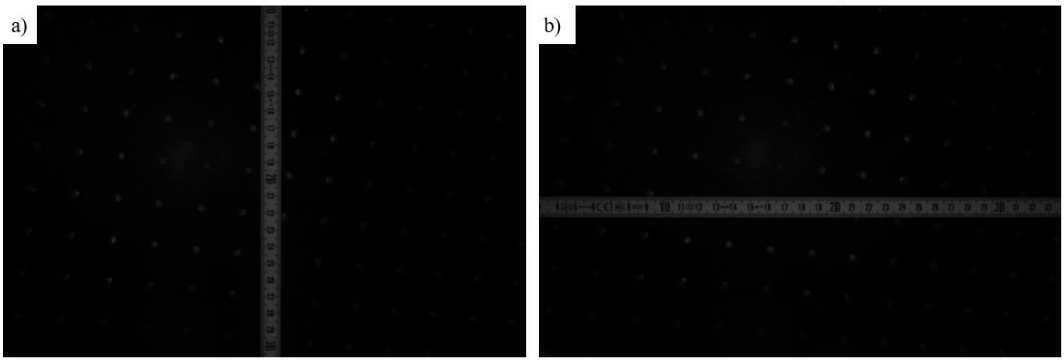

Fig. 3.4: Images of the measuring tape a) along the vertical axis and b) along the horizontal axis.

From **Fig. 3.4** it is possible to see that the FOV is equal to 17.3 cm x 27.7 cm (vertical x horizontal). This range of values were selected in order to easily image and analyze lesions of the skin that can potentially reach the size of several centimeters. Furthermore, since the effective area of the sensor of the CMOS camera is equal to 11.33 mm x 7.13 mm, and that the magnification can be calculated using **(2.3)** reported in **Sec. 2.4.3.3**, the resulting experimental value (reported as demagnification since the magnification is negative) equals to 29.2 along the horizontal axis and 29.4 along the vertical axis.

3.2.3.2 Spatial resolution

The spatial resolution of MultiSmart was assessed for each individual LED spectral band using a positive resolution test target (Thorlabs R2L2S1P1). This target functions similarly to the USAF 1951 targets mentioned in **Sec. 2.4.3.1** but is larger in size, making it suitable for imaging systems with lower spatial resolution capabilities. The target was illuminated by each LED, and the results are displayed in Figure 3.5.

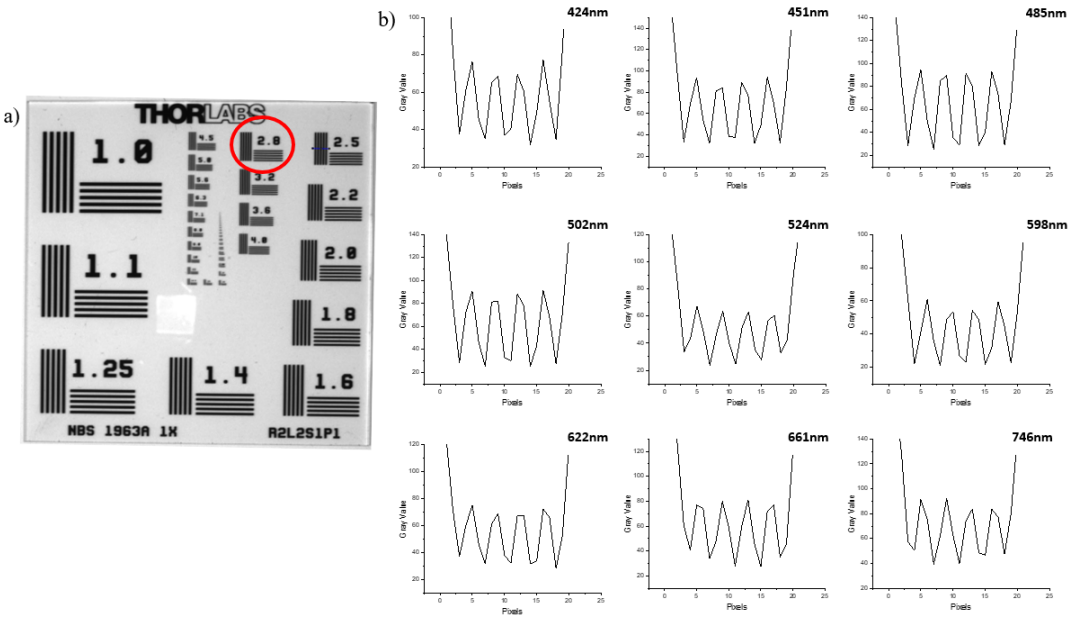

Fig. 3.5: Results of the spatial resolution analysis. a) The image shows the positive resolution target acquired using the 424 nm LED (Violet). The smallest element that MultiSmart can clearly resolve is circled in red, indicating a resolution of 2.8 line pairs per millimeter (LP/mm). b) The line profile analysis of the cross-section view of the selected element is presented. This analysis plots intensity versus pixels over the three lines of Element 2.8, as described in **Sec. 2.4.3.1**, for each LED.

Across all these imaging assessments, MultiSmart consistently demonstrated a spatial resolution of 2.8 LP/mm, which corresponds to a smallest resolvable detail of 357 µm. This shows that the system provides a spatial resolution that is maintained approximately stable across the whole spectral range and that is suitable for the analysis of skin lesions with dimensions of several centimeters.

3.2.3.3 Image contrast and SNR

An assessment of image contrast (C) and signal-to-noise ratio (SNR) has been conducted for each LED spectral band using the MultiSmart system. These measurements were performed on images of the same calibrated target, using the equations explained in **Sec. 2.4.3.2**. Image contrast C and SNR are calculated in specific ROIs for each of the spectral images. Two square ROIs are selected: a ROI located entirely on a darker region and a ROI located on a brighter region corresponding to the white background of the target. An example of the image of the target and the selected ROIs is reported in Figure 3.6:

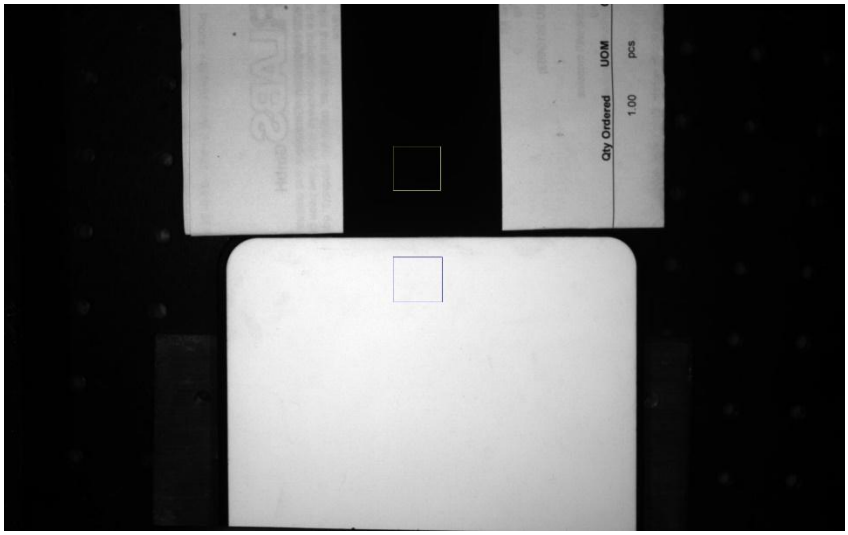

Fig. 3.6: The image shows the target used to assess contrast and SNR. It includes a white reference standard (Spectralon) to select a bright ROI (blue square) and a completely light-absorbent black paper to select a dark ROI (yellow square).

Contrast and SNR are calculated using **(2.1)** and **(2.2)** in **Sec. 2.4.3.2**. The results are reported in Table 3.3.

Wavelength (nm)	Contrast	SNR
424	0.99	81.3
448	0.99	57.3
485	0.99	80.3
502	0.99	78.7
530	0.99	96.0
598	1.00	50.0
623	0.99	55.5
658	0.99	59.8
740	0.99	46.3

Table 3.3: Contrast and SNR values for each LED.

The results reported in **Table 3.3** show that both the contrast and SNR values are quite high, providing a good imaging quality.

3.2.4 Acquisition times of MultiSmart

Based on the power output detailed in **Sec. 3.2.2**, the minimum integration time for the camera was estimated to be 25 ms when using a white calibration standard

(Labsphere, Spectralon® 5"). The maximum integration time, determined during the application of MultiSmart for the analysis of chronic skin ulcers, was calculated to be 75 ms. Given that the total number of images to collect is nine, the time required to acquire one dataset, considering only the camera's integration time, ranges from a minimum of 0.225 s to a maximum of 0.675 s. However, the switching rate from one LED to the other, which is approximately 1 s, must also be considered. This means that the switching rate primarily governs the total collection time for one dataset. Since there are nine LEDs, the total acquisition time is about 9-10 seconds per dataset.

3.2.5 Summary of the main technical characteristics of MultiSmart

An outline of the technical characteristics and features of MultiSmart is reported in Table 3.4:

Characteristics	
Illumination source:	9 LEDs
Spectral range:	424 – 740 nm
Average output power on target's surface:	3 – 10 mW
Type of detector:	CMOS
Sensor format:	1920 px x 1200 px
Pixel size:	5.86 μm x 5.86 μm
Spatial resolution:	357 μm
FOV:	11.33 mm x 7.13 mm
Typical acquisition time per dataset:	9-10 s

Table 3.4: Main characteristics of the MultiSmart device.

3.3 Calibration of MultiSmart with liquid blood optical phantoms

In this work, the use of the MultiSmart device is proposed for a more accurate monitoring of chronic skin ulcers, with the aim of reducing amputation rates and achieving successful healing outcomes. The first step towards an extraction of quantitative data is the calibration of the system. For this task, liquid optical phantoms composed of known concentrations of water, intralipid (IL), human blood and oxygen have been used in order to mimic all possible scenarios, ranging from

healthy skin to severely lesioned tissues. Liquid optical phantoms are widely used for the calibration procedures of novel spectroscopic systems thanks to their easy fabrication, availability of materials, and their ability to mimic the properties of biological tissues [76]. Data obtained from the analysis of the optical phantoms are then utilized for the construction of lookup tables (LUTs), which gather all possible reflectance values with the corresponding concentrations of blood and oxygen. Nine LUTs are created (one for each LED). The LUTs can then be used to analyze datasets acquired with MultiSmart on patients affected by skin ulcer to quantitatively extract important physiological values. In the following paragraphs, the calibration procedure based on the phantoms and LUT method is going to be thoroughly described.

3.3.1 Description of the optical liquid phantoms and data collection

Optical liquid phantoms are specially designed solutions or suspensions that mimic the optical properties of biological tissues [76,95]. They are widely used in biomedical optics to calibrate and validate imaging systems, ensuring accurate quantitative results in diagnostic and therapeutic applications [76,95]. Optical liquid phantoms are typically composed of three main elements: (1) a solvent, such as water or alcohol [76], (2) scattering agents (polystyrene beads, titanium dioxide, or lipid emulsions that scatter light similarly to biological tissues) [76], and (3) absorbing agents (dyes or inks like India ink or hemoglobin derivatives to absorb light at specific wavelengths) [76]. The primary purpose of optical liquid phantoms is to provide a controlled and reproducible environment to test and calibrate optical imaging systems. In fact, by comparing the system's response to the known properties of the phantom, any discrepancies can be identified and corrected. It is also an ideal method to develop and optimize imaging protocols: the imaging parameters can be adjusted and tuned using phantoms to achieve the best possible image quality and quantitative accuracy, without exposing patients to risk [76,95].

In this study, liquid optical phantoms have been developed using water, Intralipid-20% (IL), and fresh human blood provided by Dr. Bonaudo of the Azienda Ospedaliero-Universitaria Careggi in Florence. Authorization for the use of human blood samples (Studio ID: 23672 - 23672_BIO) was granted by the Ethical Committee of the Area Vasta Centro. The objective is to create a tissue-like phantom

that accurately mimics human skin properties, including both healthy tissue and lesions. By varying the concentration of blood within the phantom and adjusting its oxygen saturation levels (transitioning between oxygenated HbO_2 and deoxygenated HHb forms), it is possible to replicate the optical properties of healthy skin tissue as well as pathological lesions that deviate significantly from normal physiological conditions. This approach allows for the precise simulation of various skin conditions, particularly focusing on two important parameters used to define the health status of tissues: BVF and saturation (sO_2).

BVF refers to the proportion of the total volume of a tissue that is occupied by blood [31]. This parameter is crucial in biomedical optics and tissue imaging because it helps in assessing the perfusion and vascularization of tissues, which are important indicators of tissue health and function [31]. It is typically expressed as a percentage or a decimal. Mathematically, it can be defined as:

$$BVF = \frac{Vb}{Vt} \times 100 \tag{3.13}$$

Where *Vb* is the volume of blood within the tissue (or phantom), and *Vt* is the total volume of the tissue (or phantom). Typical BVF skin values measured on Caucasian subjects range from 2 to 5% [96].

Saturation (sO_2) refers to the oxygen saturation of hemoglobin, which is a measure of the percentage of hemoglobin molecules in the blood that are bound with oxygen [31]. This parameter is crucial for assessing the oxygenation status of tissues, as it provides insights into tissue perfusion and metabolic activity [31]. Saturation can be defined as:

$$sO_2 = \frac{HbO_2}{HbO_2 + HHb} \times 100 \tag{3.14}$$

In biomedical optical imaging, oxygen saturation is a key parameter for evaluating tissue health. It helps in diagnosing medical conditions such as hypoxia (low oxygen levels) or hyperoxia (high oxygen levels), and in general with understanding the blood supply to tissues [31]. It is also a valuable parameter for

assessing the oxygenation status of tissues during surgeries wound healing. Typical saturation skin values measured on Caucasian subjects range from 25 to 90% [97].

Table 3.5 reports the BVF and saturation values utilized for the phantom, and a picture of the experimental setup is reported in Figure 3.8.

Step	BVF (%)	sO_2 (%)
Baseline	0	0
1	2	0, 20, 40, 60, 80, 100
2	4	0, 20, 40, 60, 80, 100
3	6	0, 20, 40, 60, 80, 100
4	8	0, 20, 40, 60, 80, 100
5	10	0, 20, 40, 60, 80, 100

Table 3.5: Steps describing the various combinations of BVF and saturation used to modify the optical liquid blood phantom and mimic various situations of healthy and lesioned skin.

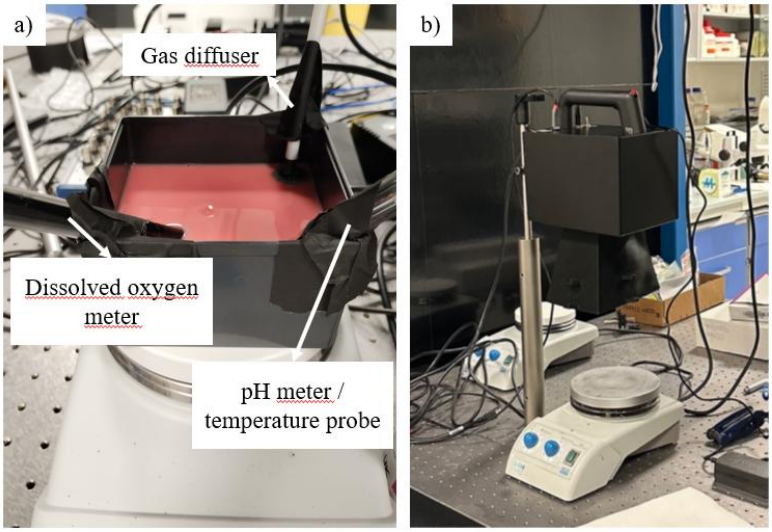

Fig. 3.8: Experimental setup for the optical liquid phantom analysis. a) Blood phantom contained in a 14 x 14 x 9 cm black plastic container. A gas diffuser equipped with air stones is used to flux oxygen gas from a tank when needed. Two sensors are used to constantly monitor the experimental parameters of the phantom: a pH meter (accuracy ±0.01 pH) for pH tracking which also serves as a temperature probe (accuracy ±0.5 °C), and a dissolved oxygen meter (accuracy mg/l Oxygen ±1.5%) to keep count of how much oxygen needs to be fluxed. b) A magnetic stirrer is used to heat the solution (constantly maintained at 36.5-37°C) and to stir it throughout the entire duration of the experiment.

The solvent used is a 50 mM aqueous solution of phosphate-buffered saline (PBS), which maintains the pH of the phantom at physiological levels (approximately 7). The total volume of the phantom is consistently maintained at 300 ml throughout the experiment.

As described in **Table 3.5**, the experiment begins with the collection of the baseline condition dataset, where no blood is added. This initial solution consists of 280 ml of PBS aqueous solution and 20 ml of IL. Since blood is not present, the saturation cannot be varied. In the next phase (Step 1), a known aliquot of 6 ml of human blood is added to achieve a BVF of 2%. To maintain the final volume of the phantom at 300 ml, 6 ml of the initial baseline solution is removed before adding the blood aliquot. During Step 1, the saturation is initially increased to 100% using the oxygen gas diffuser and then decreased to 0% by adding common brewer's yeast (up to 10 g). Data sets are collected each time the saturation decreases by 20%, resulting in a total of 6 data sets. This procedure is repeated for subsequent steps, with 6 ml of the solution removed before adding 6 ml of blood to incrementally increase the BVF by 2%. For each step, data sets are acquired at six different saturation levels (100%, 80%, 60%, 40%, 20%, and 0%), for a total of 36 datasets. No additional yeast is required after the initial addition, as it suffices for the entire experiment.

3.3.2 Data processing for the phantom datasets

Each dataset collected for the various combinations of BVF and saturation is analyzed to extract a mean average reflectance value for every combination. Regions of interest (ROIs) are selected for each dataset, and reflectance data cubes $R(x,y,\lambda)$ are reconstructed using the image processing procedure described in **Sec. 2.6.1**. The Labsphere Spectralon® 5" was used as a white calibration standard, and dark images were also acquired. An example of an image of the liquid blood phantom with the selected ROI is shown in Figure 3.9.

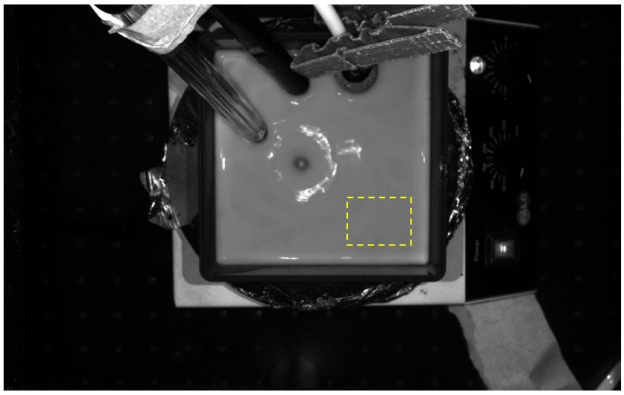

Fig. 3.9: Example of an image of the liquid blood phantom acquired using MultiSmart with the 485 nm LED, BVF = 2% and saturation = 20%. The yellow square represents the selected ROI, that must be chosen in a homogenous area without specular reflections and avoiding the vortex caused by the motion of the magnetic stirrer.

The above-mentioned procedure is applied to every image captured with each LED, for every combination of BVF and saturation.

3.3.3 Construction of Look Up Tables

The resulting reflectance values are used to construct intermediate LUTs, one for each LED. The initial LUTs are of 6 x 6 points each. An example is reported in Table 3.6.

BVF %	sO_2=0%	sO_2=20%	sO_2=40%	sO_2=60%	sO_2=80%	sO_2=100%
0	0.86093	0.86093	0.86093	0.86093	0.86093	0.86093
2	0.19133	0.18819	0.18950	0.17913	0.16242	0.15728
4	0.13123	0.12589	0.12476	0.11098	0.09716	0.10399
6	0.09769	0.09677	0.09798	0.08630	0.07810	0.07597
8	0.09059	0.07752	0.07702	0.08305	0.06373	0.06622
10	0.06965	0.06714	0.06307	0.05623	0.05081	0.04530

Table 3.6: An example of an intermediate LUT constructed for the 485 nm LED is shown. The LUT reports a reflectance value associated with each combination of BVF and saturation values. The first line (BVF = 0%) shows the same reflectance value for every saturation percentage because no blood is present, so variations in saturation cannot occur and do not affect the reflectance values. Similar LUTs are constructed for the other LEDs, yielding different reflectance results specific to their wavelengths.

The LUTs explained above are considered intermediate because a 6 x 6 grid is insufficient for thoroughly analyzing complex biological tissues, such as skin lesions, which often exhibit highly inhomogeneous characteristics and may contain areas with BVF above 10%. Therefore, two linear interpolation operations are performed for the following reasons: (1) to add intermediate points between the already selected saturation percentages, and (2) to add intermediate points for the BVF values. Additionally, a linear extrapolation is conducted to extend the LUT up to 20% of BVF. These procedures could not be performed experimentally due to the rapid changes in saturation and the insufficient availability of human blood samples to achieve such high BVF. The interpolation and extrapolation operations were carried out using OriginLab 2024 Software. The final expanded LUTs for each LED are of 26 x 51 points (saturation x BVF, and cannot be shown due to insufficient space). The BVF starts from 0% and ends at 20% with an incremental step of 0.4%, while the saturation goes from 0% to 100% with a step of 4%. By expanding the LUTs in this manner, they can be effectively applied to the analysis of skin ulcer images acquired using MultiSmart. This allows for the extraction of quantitative values of BVF and saturation in the area of the lesion with a high degree of detail.

3.4 Analysis and study of *in-vivo* chronic ulcers and skin lesions

The following paragraphs explain the analysis pipeline that has been developed for the *in-vivo* study of skin lesions. This includes the acquisition and imaging processing of patient datasets and the creation of a script for their analysis, based on the utilization of the LUTs described in the previous section.

3.4.1 Acquisition and image processing of patient datasets

The image processing procedure applied to patient datasets follows the same methodology as described in **Sec. 3.3.2** and **Sec. 2.6.1**. In summary, the steps include: selecting a ROI, normalizing the patient's dataset using a white reference datacube after subtracting dark counts from both the patient and white reference images. Additionally, these datasets must be weighed according to the ratios of their respective integration times of the camera used during acquisition. The white reference standard utilized is the Labsphere Spectralon® 5". An example of an image collected on a patient using MultiSmart is shown in Figure 3.10.

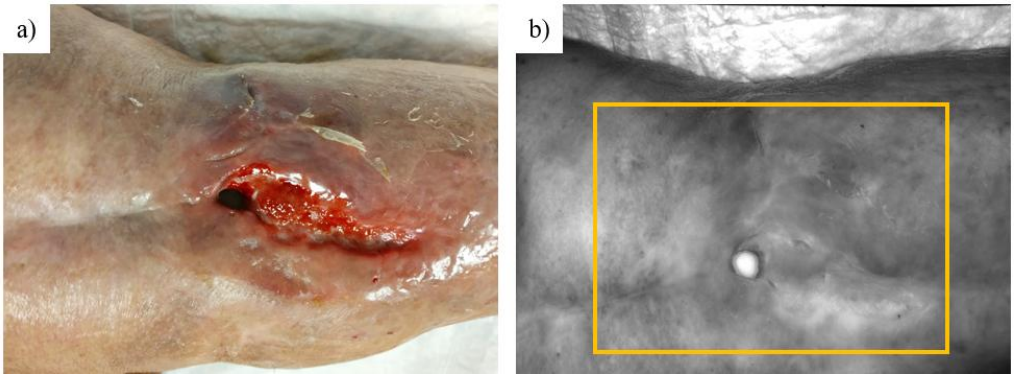

Fig. 3.10: A chronic ulcer affecting the knee of a patient, caused by an implanted prosthesis inside of it. a) RGB picture, taken with a cellphone. b) Example of an image collected with MultiSmart at 485 nm. The yellow square represents the selected ROI.

The image processing is done in MATLAB R2023a and the final reflectance dataset is exported as a group of 9 excel files with extension .xlsx (one file for each LED), which are necessary for the subsequent LUT analysis.

3.4.2 Development of a script for the analysis of skin lesions using the LUTs

The aim of the present step is the development of a cross-check algorithm to find the LUT reflectance value that is closest to each pixel in the patient's reflectance image. The script is written in MATLAB R2023a and is based on the use of the root mean square error (RMSE) function. The RMSE function is a standard measure used to quantify the difference between values predicted by a model or obtained from an experiment and the values observed or measured. It is widely used in various fields, including image processing, to compare datasets and assess the accuracy of models or simulations. The RMSE is defined as the square root of the average of the squared differences between the predicted or observed values and the actual values. Mathematically, it is expressed as:

$$RMSE = \sqrt{\frac{1}{n}\sum_{i=1}^{n} |LUT_i - S_i|^2} \tag{3.15}$$

where n is the number of observations, which is always equal to 9 (the number of LEDs). LUT is the LUT array and S is the array of the sample (in this case the patient ulcer) extracted from a certain pixel. The formula uses LUT arrays in the sense that for each couple of BVF and saturation values, a "predicted" spectrum

can be extracted from the LUTs: for example, considering an arbitrary combination of BVF=2% and saturation=4%, the LUT-predicted reflectance values are reported in Table 3.7.

λ (nm)	424	448	485	502	530	598	623	658	740
Refl.	0,02208	0,107898	0,190074	0,170093	0,13635	0,11457	0,37091	0,42354	0,5273

Table 3.7: Example of a spectrum array, reporting the reflectance values for each wavelength, extracted from the LUT for BVF=2% and saturation=4%.

The same type of array can be defined for each pixel of the patient's reflectance dataset. An example is shown in Table 3.8.

λ (nm)	424	448	485	502	530	598	623	658	740
Refl.	0,027025	0,083449	0,124086	0,095442	0,090771	0,098807	0,365784	0,42655	0,501854

Table 3.8: Example of a spectrum array, reporting the reflectance values for each wavelength, extracted from pixel in position (1;1) of a patient's dataset. A similar array can be extracted from each pixel of the dataset.

As explained at the beginning of the paragraph, the predicted array (*LUT*) reported in **Table 3.7** can be compared to the patient's array (*S*) shown in **Table 3.8** using (**3.15**), where *i* represents each wavelength, for a total *n*=9. The aim of the algorithm is to compare the patient's array *S* with every predicted array *LUT*, and store the values of BVF and saturation associated with the best-matching *LUT* array. Of course, the best result is given by the lowest possible value of RMSE. In fact, a low RMSE value means that the *LUT* array is very close to the values of *S*. This procedure is then repeated for every pixel of the patient's dataset. The script's execution times typically range from approximately 30 minutes for smaller fields of view (around 700 x 700 pixels) to 1 hour for larger fields of view (around 700 x 1400 pixels). The algorithm was executed on a system with an 11th Gen Intel(R) Core(TM) i7 processor and 32.0 GB of RAM. During execution, the algorithm utilized an estimated 6 GB of RAM.In summary, for each pixel of the patient's dataset, the algorithm runs the analysis using the following steps:

- Extraction of the reflectance array (*S(x,y)*) of the selected pixel of coordinates (x,y);
- Comparison of *S* with each predicted spectrum in the *LUT* array using the RMSE function.

- Recording the position of the *LUT* array which gives the lowest possible RMSE.
- Analysis of the entire patient dataset and retrievement of the coordinates of the best *LUT* arrays found for each pixel of the patient's image. The coordinates are associated with the corresponding BVF and saturation values.
- Creation of images displaying BVF and saturation values for each pixel, resulting in two different images: one BVF map and one saturation map for the patient.

3.5 Results of the analysis of skin lesions using MultiSmart

A quantitative analysis of skin lesions using the MultiSmart device is performed following the methodologies described in the previous paragraphs. Patients affected by skin ulcers that were recruited for data collection have signed a declaration of consent, in which it is stated that the device in question is non-invasive and does not interfere in any way with the Usual Care procedures. For this reason, the approval of an ethics committee is not required, as the followed procedure falls within the scope of usual care. The final output consists of two 2D maps: one displaying the BVF percentages for each pixel in the patient's dataset, and the other showing the saturation percentages. These maps are then superimposed onto the RGB images to enhance visualization and understanding of tissue perfusion, blood supply, and oxygenation. The superimposition is currently done manually, as the final software is still under development. Two example patients are shown in Figure 3.11.

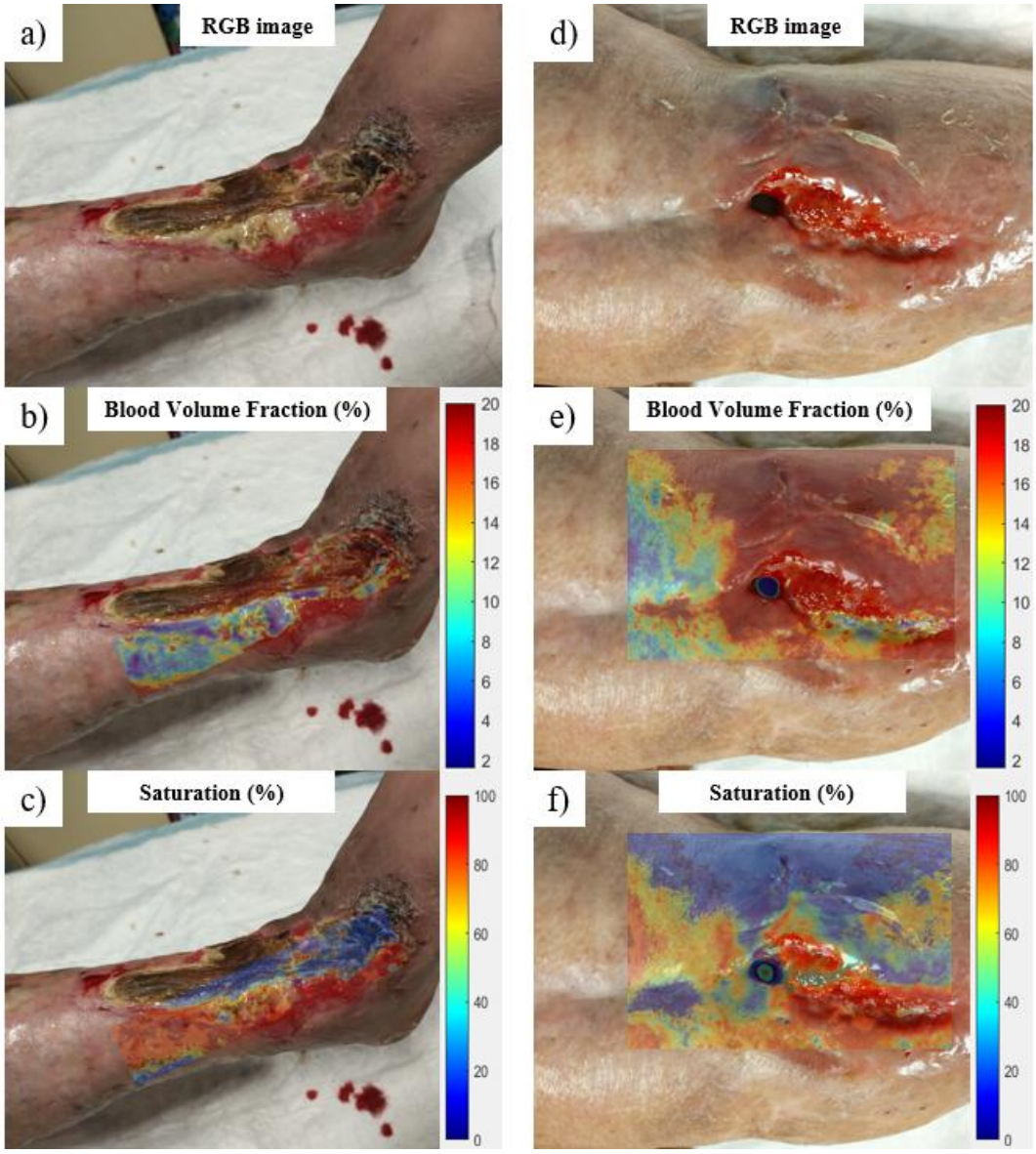

Fig. 3.11: Two different patients affected by chronic leg skin ulcers. a), d): RGB pictures of the leg ulcers of the patients. b), e): BVF colormaps, superimposed on the RGB pictures of the two ulcers. In this colormap, warmer colors represent higher values of BVF, while lower values are represented by colder colors. c), f): saturation colormaps, superimposed on the RGB pictures of the two ulcers. The color scale is the same as the one used for BVF maps. It is important to note that the MultiSmart device does not have the capability to acquire RGB images. The RGB images presented in the thesis were captured using a smartphone camera, carefully positioned to match the same FOV as the one imaged with MultiSmart. This approach ensured alignment between the RGB and MultiSmart images for effective comparison and visualization. Total FOV for images b), c): 337 x 1427. Total FOV for images e), f): 801 x 1371.

Fig. 3.11 illustrates the complexity of the analyzed lesions, which encompass various tissue types including tendons, necrotic tissue, and healthy tissue as one

moves away from the ulcer margins. In the BVF maps (**Fig. 3.11 b,e**), the areas of completely open tissue exhibit BVF percentages significantly higher than the physiological values typically observed in Caucasian skin, which range from 2 to 5% [96]. This suggests an abnormal accumulation of blood in the wounded areas, with the BVF gradually normalizing as the distance from the wound increases.

Fig. 3.11e is particularly noteworthy because it shows elevated BVF even in regions where the skin appears intact (located in the upper part of the map). Upon closer inspection of the RGB photograph (**Fig. 3.11d**), this area is identified as affected by hematoma, evident from the purplish discoloration of the skin. This indicates that the device can potentially detect subcutaneous blood effusions.

High BVF values correspond to low saturation levels (**Fig. 3.11 c,f**), suggesting that the abundant blood in these regions is predominantly deoxygenated (HHb), and these areas are not sufficiently oxygenated. Saturation levels approach more physiological values in regions less impacted by the ulcers, reflecting better tissue oxygenation in these areas.

3.6 Conclusions and summary of the MultiSmart project

MSI devices, such as the MultiSmart system, are advanced optical diagnostic tools used for non-invasive monitoring and characterization of various pathologies, including skin wounds and ulcers. These devices can track alterations in structural and physiological parameters like oxygenation and hemodynamics by observing changes in the optical properties of tissues across multiple spectral bands. The novel, compact, and transportable MultiSmart device utilizes LEDs and a CMOS camera, making it user-friendly and cost-effective. It targets specific wavelengths in the visible-NIR spectrum to monitor oxygenation and hemodynamics, crucial for assessing wound healing in chronic ulcers. The system's calibration involves using liquid optical phantoms, composed of water, intralipid, human blood, and oxygen, to replicate different tissue scenarios. Data from these phantoms are used to create Look-Up Tables (LUTs) that map reflectance values to blood volume fraction (BVF) and saturation levels. These LUTs enable the quantitative analysis of BVF and saturation in skin ulcer images acquired with the MultiSmart device. The analysis pipeline includes selecting regions of interest, normalizing patient datasets,

and employing a script to compare patient data with LUT values using the root mean square error (RMSE) function to identify the best matches. For each pixel, the algorithm extracts reflectance, compares it to the LUT spectra, records the lowest RMSE, and maps the corresponding BVF and saturation values. Findings indicate that BVF maps reveal high BVF in open wounds, suggesting abnormal blood accumulation that normalizes with distance from the wound. Elevated BVF in intact skin areas, such as those with hematomas, demonstrates the device's ability to detect subcutaneous blood. High BVF values are associated with low saturation levels, indicating deoxygenated blood in poorly oxygenated regions, with saturation improving in less affected areas. The overall results demonstrate that MSI devices, such as MultiSmart, have significant potential as powerful tools for the everyday monitoring of skin ulcers. These devices can assess critical features such as the severity of ulcers, the progression of healing, and the effectiveness of treatment protocols. However, important future developments are needed for MultiSmart, including enabling real-time analysis and display of saturation and BVF maps, detecting additional parameters such as microbial pathogens to preempt serious infections, and identifying species closely related to tissue metabolism, such as the oxidized (oxCCO) and reduced (redCCO) forms of cytochrome-c-oxidase (CCO). Achieving these goals will require increasing the number of LEDs to cover a broader spectrum and detect more chromophores. Other potential enhancements could include the integration of software capable of compensating for motion artifacts. Although the dataset acquisition times are relatively short (approximately 10 seconds per datacube), the possibility of patient movement during the process cannot be ruled out. This is particularly relevant as many patients experience pain from their lesions, making it difficult for them to remain still. Motion artifacts present a significant challenge, as the images collected at each wavelength must correspond to the exact same FOV to ensure accurate data analysis. This motion compensation software would be needed also for when the MSI device is used without a tripod, in handheld mode. Of course, it is impossible for the operator to stay completely still while holding the device, and some lesions are hard to image with the device mounted on the tripod. The motion compensation software would also be essential when the MSI device is operated in handheld mode without a

tripod. It is inherently difficult for the operator to maintain complete stability while holding the device, and certain lesions are challenging to image when the device is mounted on a tripod. Implementing such software would ensure consistent and accurate imaging, even under these conditions.

To enhance reproducibility, another valuable feature to consider adding is a system that monitors the distance between the MSI device and the target. This functionality would ensure consistent imaging of the same area and FOV, which is particularly important when capturing images of an ulcer before and after treatment or over a specific period to monitor healing progress. Such a system would improve the accuracy and reliability of longitudinal studies by maintaining consistency across imaging sessions.

Chapter 4: Conclusions and future outcomes

This dissertation presents a project based on two innovative research lines aimed at addressing critical healthcare challenges through the strategic use of spectral imaging technologies: (1) the development of a HSI system for rapid biochemical analysis of fresh brain tumor (glioma) biopsies, and (2) the creation of a MSI system for chronic skin ulcer monitoring. These systems exemplify the transformative potential of spectral imaging in improving clinical outcomes through non-invasive, real-time imaging modalities tailored to specific clinical needs.

The HSI system, called HyperProbe1, leverages a broad range of spectral bands to capture detailed biochemical and structural differences in glioma tissue samples. By differentiating the severity of gliomas through the quantification of key biomarkers such as oxyhemoglobin (HbO_2), deoxyhemoglobin (HHb), cytochrome-c-oxidase (CCO), and lipids, the system enhances tumor characterization and informs treatment planning without the need for tissue fixation or staining. The successful assembly, software development, dataset collection, and algorithm creation for HyperProbe1 have demonstrated its ability to provide quantitative biochemical analysis and mapping of surgical biopsies. Initial findings indicate its potential to distinguish between lower and higher-grade gliomas, suggesting a new methodology for tumor classification based on HSI.

The MSI system, named MultiSmart, is designed for non-invasive, quantitative monitoring of tissue oxygenation levels and blood concentration in chronic skin ulcers. The compact and portable device uses LEDs and a CMOS camera to capture changes in optical properties across multiple spectral bands. Calibration with liquid optical phantoms and the development of lookup tables enable the quantitative assessment of BVF and oxygen saturation in skin ulcer images. Results demonstrate the device's capability to track wound healing, detect abnormal blood accumulation, and identify poorly oxygenated regions, making it a powerful tool for everyday monitoring of chronic ulcers.

Both HyperProbe1 and MultiSmart showcase the versatility and potential of spectral imaging technologies in diverse medical fields. HyperProbe1 aims to revolutionize digital histology of *ex-vivo* tissue by providing rapid and quantitative

analysis, paving the way for *in-situ* histopathological screening during brain surgery. MultiSmart, on the other hand, offers a practical solution for continuous monitoring of chronic wounds, facilitating timely interventions and better management of wound healing processes.

Regarding the future outcomes, the promising results of this work open several avenues for future research and development. For HyperProbe1, future investigations will involve larger and more diverse cohorts of glioma biopsy samples, including comparisons with healthy cerebral tissue, to validate the initial findings and enhance the statistical robustness of the results. The ultimate goal is to translate this technology into a compact, cost-effective, and user-friendly device for real-time surgery guidance, potentially transforming current neurosurgical practices with an all-optical, quantitative imaging approach.

For MultiSmart, future developments will focus on enabling real-time analysis and display of saturation and BVF maps, detecting additional parameters such as microbial pathogens to preempt serious infections, and identifying species related to tissue metabolism, such as the oxidized and reduced forms of CCO. Expanding the number of LEDs to cover a broader spectrum will allow the detection of more chromophores, further enhancing the device's diagnostic capabilities.

In summary, this dissertation demonstrates the significant potential of HSI and MSI systems in improving clinical diagnostics and patient outcomes. By continuing to refine these technologies and explore new applications, spectral imaging can play a pivotal role in advancing medical imaging and healthcare practices.

Appendix

This appendix presents additional datasets of patients with chronic skin ulcers analyzed using the MultiSmart device, which were not included in Chapter 3. Notably, along with the BVF and saturation maps, RGB images of the ulcers are provided as a reference. However, the RGB images are not superimposed on the resulting maps due to the impracticality of manual alignment. Nevertheless, the results can still be compared with the RGB images without significant effort.

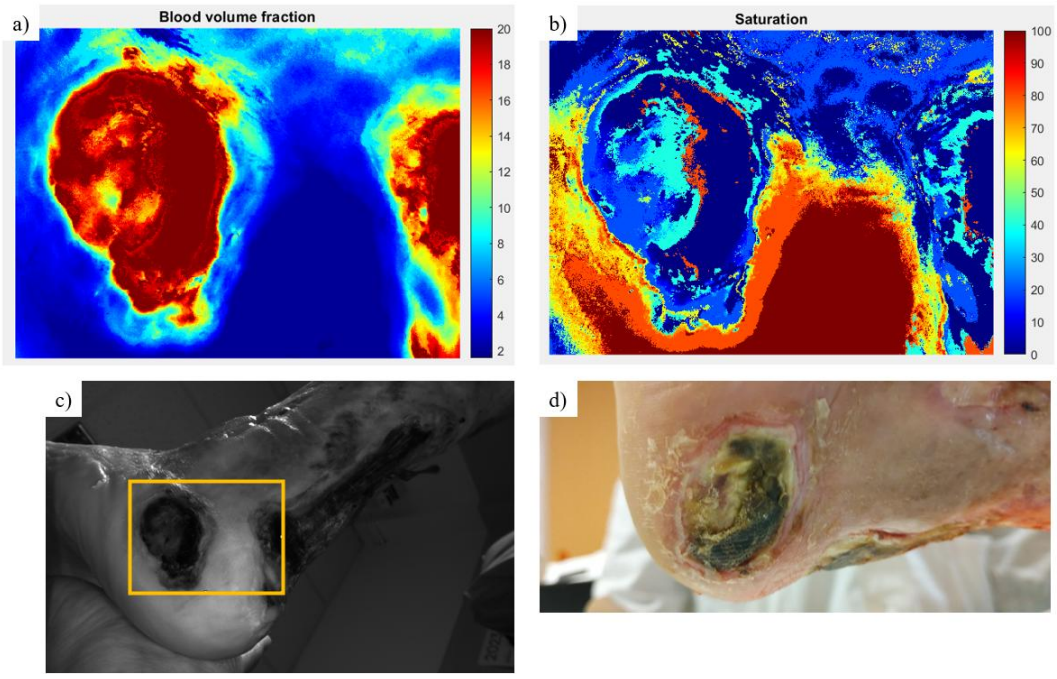

Fig. A.1: Patient affected by a chronic skin ulcer positioned on the inner part of the foot, below the ankle. a) BVF colormaps. In this colormap, warmer colors represent higher values of BVF, while lower values are represented by colder colors. b) Saturation coloramaps. The color scale is the same as the one used for BVF maps. c) Grey scale image collected with MultiSmart using the 502 nm LED. The yellow frame represents the area that was imaged. d) RGB picture of the ulcers of the patient. Total pixels of the FOV: 453 x 621.

In the case of the patient shown in Fig. A.1, it is evident that the dark portion of the lesion, particularly prominent in A.1.c, exhibits a high blood content. By cross-referencing this map with the saturation map, it becomes clear that this entire region is characterized by a very low oxygen saturation level, indicating that the blood is completely deoxygenated, which is consistent with the presence of necrotic (dead) tissue.

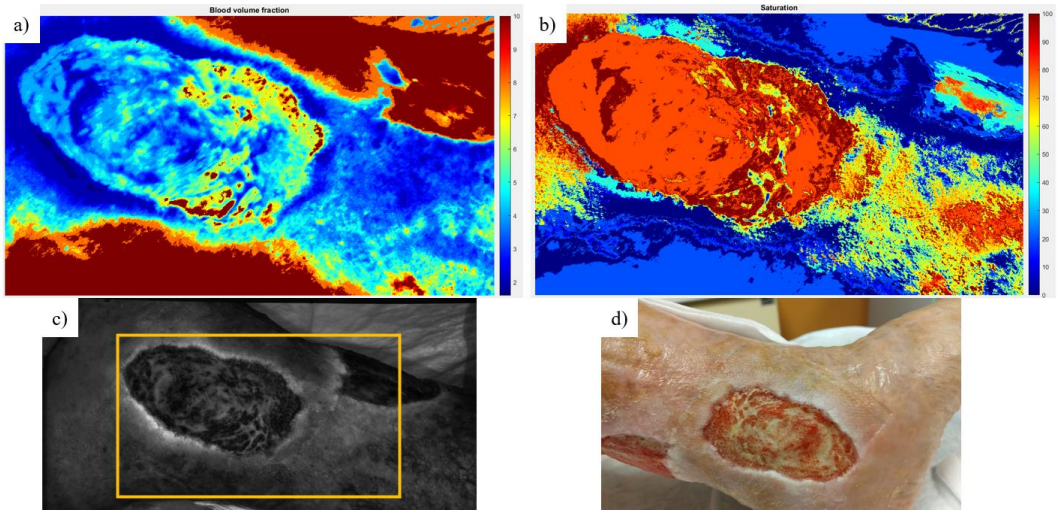

Fig. A.2: Patient affected by a chronic skin ulcer positioned on the outer part of the ankle. a) BVF colormaps. In this colormap, warmer colors represent higher values of BVF, while lower values are represented by colder colors. b) Saturation coloramaps. The color scale is the same as the one used for BVF maps. c) Grey scale image collected with MultiSmart using the 502 nm LED. The yellow frame represents the area that was imaged. d) RGB picture of the ulcers of the patient. Total pixels of the FOV: 717 x 1363.

In this case, the unhealthy region appears highly inhomogeneous, with small areas showing normal BVF levels, while other portions exhibit significantly elevated BVF, particularly in the regions with visible blood, as expected. The saturation within the lesioned area is relatively low (around 80%), indicating that the tissue is compromised but not yet necrotic.

Abnormal saturation and BVF levels are also observed in areas further from the lesion. This may be attributed to the imaging area's height, where the external regions are not on the same plane as the lesion's center on the ankle. Such discrepancies could result in focusing artifacts and erratic data. Reducing the field of view (FOV) during imaging could help address this issue by minimizing these artifacts.

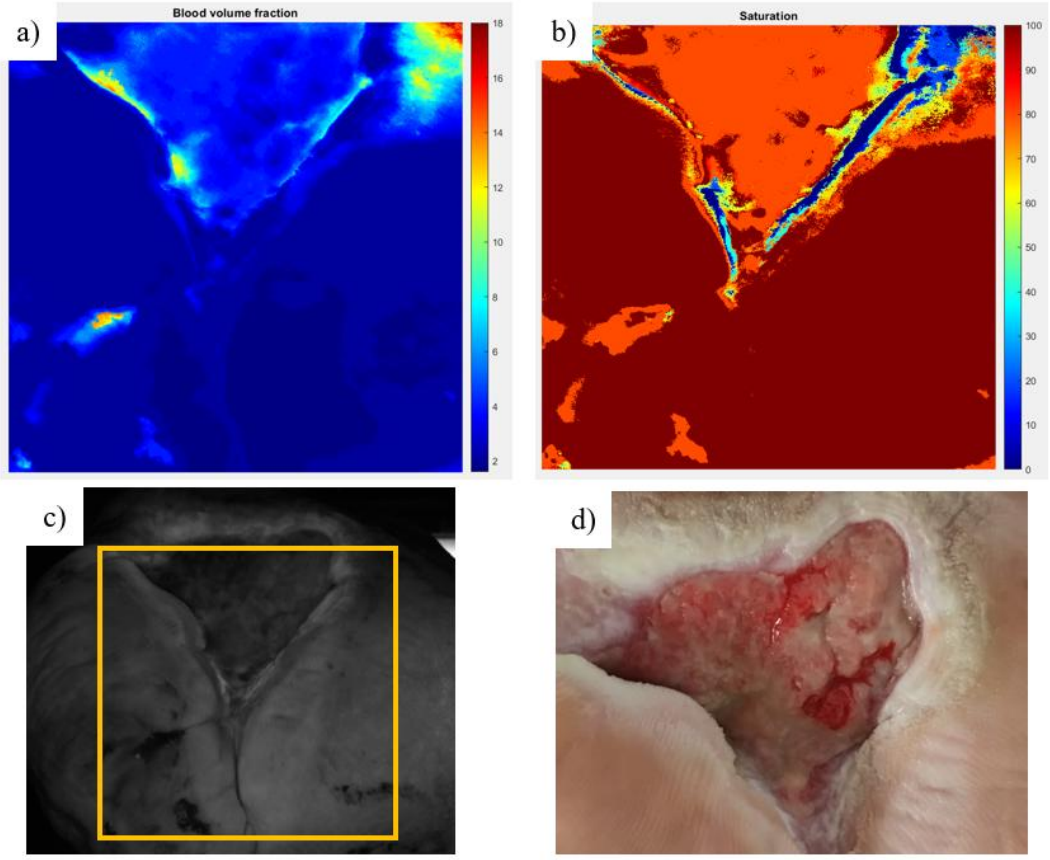

Fig. A.3: The presented patient is affected by a chronic pressure ulcer located on the lower part of the knee. This ulcer developed as a result of prolonged use of a prosthesis following the amputation of the portion of leg below the knee. a) BVF colormaps. In this colormap, warmer colors represent higher values of BVF, while lower values are represented by colder colors. b) Saturation coloramaps. The color scale is the same as the one used for BVF maps. c) Grey scale image collected with MultiSmart using the 502 nm LED. The yellow frame represents the area that was imaged. d) RGB picture of the ulcers of the patient. Pixels of the FOV: 767 x 773.

From Fig. A.3, it can be observed that BVF levels are slightly elevated in the area affected by the ulcer, while they decrease to physiological levels in the surrounding regions. This is further corroborated by the saturation levels, which are around 70–80% in the lesioned area and return to normal values in the healthier surrounding tissue, indicating that the tissue is compromised but not yet necrotic.

A very small region between the healthy and lesioned areas shows a saturation level of approximately 0%, likely due to focusing artifacts. This is evident in the RGB image, where the white regions of the tissue appear uneven and not flat.

References

1. Zhang, C. & Kovacs, J. M. The application of small unmanned aerial systems for precision agriculture: a review. *Precis. Agric.* **13**, 693–712 (2012).
2. Mulla, D. J. Twenty five years of remote sensing in precision agriculture: Key advances and remaining knowledge gaps. *Biosyst. Eng.* **114**, 358–371 (2013).
3. Govender, M., Chetty, K. & Bulcock, H. A review of hyperspectral remote sensing and its application in vegetation and water resource studies. *Water SA* **33**, (2009).
4. Clark, R. N. *et al.* Imaging spectroscopy: Earth and planetary remote sensing with the USGS Tetracorder and expert systems. *J. Geophys. Res. Planets* **108**, 2002JE001847 (2003).
5. Van Der Meer, F. D. *et al.* Multi- and hyperspectral geologic remote sensing: A review. *Int. J. Appl. Earth Obs. Geoinformation* **14**, 112–128 (2012).
6. Plaza, A. *et al.* Recent advances in techniques for hyperspectral image processing. *Remote Sens. Environ.* **113**, S110–S122 (2009).
7. Aasen, H., Burkart, A., Bolten, A. & Bareth, G. Generating 3D hyperspectral information with lightweight UAV snapshot cameras for vegetation monitoring: From camera calibration to quality assurance. *ISPRS J. Photogramm. Remote Sens.* **108**, 245–259 (2015).
8. Royo, S. & Ballesta-Garcia, M. An Overview of Lidar Imaging Systems for Autonomous Vehicles. *Appl. Sci.* **9**, 4093 (2019).
9. Liang, H. Advances in multispectral and hyperspectral imaging for archaeology and art conservation. *Appl. Phys. A* **106**, 309–323 (2012).
10. Martinez, K., Cupitt, J., Saunders, D. & Pillay, R. Ten years of art imaging research. *Proc. IEEE* **90**, 28–41 (2002).

11. Gowen, A., Odonnell, C., Cullen, P., Downey, G. & Frias, J. Hyperspectral imaging – an emerging process analytical tool for food quality and safety control. *Trends Food Sci. Technol.* **18**, 590–598 (2007).
12. Lu, G. & Fei, B. Medical hyperspectral imaging: a review. *J. Biomed. Opt.* **19**, 010901 (2014).
13. Karim, S., Qadir, A., Farooq, U., Shakir, M. & Laghari, A. A. Hyperspectral Imaging: A Review and Trends towards Medical Imaging. *Curr. Med. Imaging Former. Curr. Med. Imaging Rev.* **19**, 417–427 (2022).
14. Calin, M. A., Parasca, S. V., Savastru, D. & Manea, D. Hyperspectral Imaging in the Medical Field: Present and Future. *Appl. Spectrosc. Rev.* **49**, 435–447 (2014).
15. Manni, F. *et al.* Hyperspectral imaging for tissue classification in glioblastoma tumor patients: a deep spectral-spatial approach. in *Medical Imaging 2021: Image-Guided Procedures, Robotic Interventions, and Modeling* (eds. Linte, C. A. & Siewerdsen, J. H.) 33 (SPIE, Online Only, United States, 2021). doi:10.1117/12.2580158.
16. Giannoni, L. *et al.* Transportable hyperspectral imaging setup based on fast, high-density spectral scanning for in situ quantitative biochemical mapping of fresh tissue biopsies. *J. Biomed. Opt.* **29**, (2024).
17. Ortega, S. *et al.* Hyperspectral Imaging for the Detection of Glioblastoma Tumor Cells in H&E Slides Using Convolutional Neural Networks. *Sensors* **20**, 1911 (2020).
18. Leon, R. *et al.* Hyperspectral imaging for in-vivo/ex-vivo tissue analysis of human brain cancer. in *Medical Imaging 2022: Image-Guided Procedures, Robotic Interventions, and Modeling* (eds. Linte, C. A. & Siewerdsen, J. H.) 78 (SPIE, San Diego, United States, 2022). doi:10.1117/12.2611420.
19. Fabelo, H. *et al. In-Vivo* Hyperspectral Human Brain Image Database for Brain Cancer Detection. *IEEE Access* **7**, 39098–39116 (2019).

20. Ruiz, L. *et al.* Multiclass Brain Tumor Classification Using Hyperspectral Imaging and Supervised Machine Learning. in *2020 XXXV Conference on Design of Circuits and Integrated Systems (DCIS)* 1–6 (IEEE, Segovia, Spain, 2020). doi:10.1109/DCIS51330.2020.9268650.
21. Puustinen, S. *et al.* Hyperspectral Imaging in Brain Tumor Surgery—Evidence of Machine Learning-Based Performance. *World Neurosurg.* **175**, e614–e635 (2023).
22. Leon, R. *et al.* Hyperspectral imaging benchmark based on machine learning for intraoperative brain tumour detection. *Npj Precis. Oncol.* **7**, 119 (2023).
23. Frykberg, R. G. & Banks, J. Challenges in the Treatment of Chronic Wounds. *Adv. Wound Care* **4**, 560–582 (2015).
24. Dorra Nouri, Yves Lucas, Sylvie Treuillet, R. Jolivot, & F. Marzani. Colour and multispectral imaging for wound healing evaluation in the context of a comparative preclinical study. in vol. 8669 866923 (2013).
25. Lin, C.-L. *et al.* Multispectral Imaging-Based System for Detecting Tissue Oxygen Saturation With Wound Segmentation for Monitoring Wound Healing. *IEEE J. Transl. Eng. Health Med.* **12**, 468–479 (2024).
26. Squiers, J. J. *et al.* Machine learning analysis of multispectral imaging and clinical risk factors to predict amputation wound healing. *J. Vasc. Surg.* **75**, 279–285 (2022).
27. Philimon, S. P., Huong, A. K. C., Ong, P. E. & Ngu, X. T. I. Multispectral imaging system for clinical assessment of superficial wound tissue oxygenation. in *2016 IEEE EMBS Conference on Biomedical Engineering and Sciences (IECBES)* 9–12 (IEEE, Malaysia, 2016). doi:10.1109/IECBES.2016.7843405.
28. Basiri, A. *et al.* Use of a multi-spectral camera in the characterization of skin wounds. *Opt. Express* **18**, 3244 (2010).
29. Noordmans, H. J., De Roode, R. & Verdaasdonk, R. Fast interactive registration tool for reproducible multi-spectral imaging for wound healing and treatment evaluation. in (ed. Azar, F. S.) 64310O (San Jose, CA, 2007). doi:10.1117/12.698874.

30. Atkins, P. *Atkins' Physical Chemistry*. (Oxford University Press, Oxford).
31. Jacques, S. L. Optical properties of biological tissues: a review. *Phys. Med. Biol.* **58**, R37–R61 (2013).
32. Kim, A. D. & Keller, J. B. Light propagation in biological tissue. *J. Opt. Soc. Am. A* **20**, 92 (2003).
33. Oshina, I. & Spigulis, J. Beer–Lambert law for optical tissue diagnostics: current state of the art and the main limitations. *J. Biomed. Opt.* **26**, (2021).
34. Zhov, I. V. E. *et al.* Shallow learning enables real-time inference of molecular composition changes from broadband-near-infrared spectroscopy of brain tissue. in (2023).
35. Hecht, E. *Optics*. (Reading, Mass. : Addison-Wesley, 2002).
36. Hoggarth, A. R. *et al.* Clinical Theranostics in Recurrent Gliomas: A Review. *Cancers* **16**, 1715 (2024).
37. Titford, M. A Short History of Histopathology Technique. *J. Histotechnol.* **29**, 99–110 (2006).
38. Sanai, N. & Berger, M. S. Surgical oncology for gliomas: the state of the art. *Nat. Rev. Clin. Oncol.* **15**, 112–125 (2018).
39. Kleihues, P., Soylemezoglu, F., Schäuble, B., Scheithauer, B. W. & Burger, P. C. Histopathology, classification, and grading of gliomas. *Glia* **15**, 211–221 (1995).
40. Weller, M. *et al.* Glioma. *Nat. Rev. Dis. Primer* **1**, 15017 (2015).
41. Tarsitano, A., Pizzigallo, A., Gessaroli, M., Sturiale, C. & Marchetti, C. Intraoperative Biopsy of the Major Cranial Nerves in the Surgical Strategy for Adenoid Cystic Carcinoma Close to the Skull Base. *Oral Surg. Oral Med. Oral Pathol. Oral Radiol.* **113**, 214–221 (2012).
42. Louis, D. N. *et al.* The 2021 WHO Classification of Tumors of the Central Nervous System: a summary. *Neuro-Oncol.* **23**, 1231–1251 (2021).

43. Wen, P. Y. & Packer, R. J. The 2021 WHO Classification of Tumors of the Central Nervous System: clinical implications. *Neuro-Oncol.* **23**, 1215–1217 (2021).
44. Altinay, S. Role of Pathologist in Driver of Treatment of CNS Tumors. in *New Approaches to the Management of Primary and Secondary CNS Tumors* (ed. Morgan, L. R.) (InTech, 2017). doi:10.5772/65911.
45. Jöbsis, F. F. Noninvasive, Infrared Monitoring of Cerebral and Myocardial Oxygen Sufficiency and Circulatory Parameters. *Science* **198**, 1264–1267 (1977).
46. Ayaz, H. *et al.* Optical imaging and spectroscopy for the study of the human brain: status report. *Neurophotonics* **9**, (2022).
47. Steiner, G. *et al.* A new approach for clinical translation of infrared spectroscopy: exploitation of the signature of glioblastoma for general brain tumor recognition. *J. Neurooncol.* **161**, 57–66 (2023).
48. Fabelo, H. *et al.* An Intraoperative Visualization System Using Hyperspectral Imaging to Aid in Brain Tumor Delineation. *Sensors* **18**, 430 (2018).
49. Ma, Y. *et al.* Wide-field optical mapping of neural activity and brain haemodynamics: considerations and novel approaches. *Philos. Trans. R. Soc. B Biol. Sci.* **371**, 20150360 (2016).
50. Hillman, E. M. C. Optical brain imaging in vivo: techniques and applications from animal to man. *J. Biomed. Opt.* **12**, 051402 (2007).
51. Scholkmann, F. *et al.* A review on continuous wave functional near-infrared spectroscopy and imaging instrumentation and methodology. *NeuroImage* **85**, 6–27 (2014).
52. Fantini, S. & Sassaroli, A. Frequency-Domain Techniques for Cerebral and Functional Near-Infrared Spectroscopy. *Front. Neurosci.* **14**, 300 (2020).
53. Dehghani, H. *et al.* Near infrared optical tomography using NIRFAST: Algorithm for numerical model and image reconstruction. *Commun. Numer. Methods Eng.* **25**, 711–732 (2009).

54. Arridge, S. R. Optical tomography in medical imaging. *Inverse Probl.* **15**, R41–R93 (1999).

55. Paulmurugan, K., Vijayaragavan, V., Ghosh, S., Padmanabhan, P. & Gulyás, B. Brain–Computer Interfacing Using Functional Near-Infrared Spectroscopy (fNIRS). *Biosensors* **11**, 389 (2021).

56. Zeppa, P. *et al.* Fluorescence-Guided Surgery in Glioblastoma: 5-ALA, SF or Both? Differences between Fluorescent Dyes in 99 Consecutive Cases. *Brain Sci.* **12**, 555 (2022).

57. Chirizzi, C. *et al.* Next-generation agents for fluorescence-guided glioblastoma surgery. *Bioeng. Transl. Med.* **9**, e10608 (2024).

58. Zhang, Y. *et al.* Raman spectroscopy: A prospective intraoperative visualization technique for gliomas. *Front. Oncol.* **12**, 1086643 (2023).

59. Liu, J. *et al.* Current research status of Raman spectroscopy in glioma detection. *Photodiagnosis Photodyn. Ther.* **50**, 104388 (2024).

60. Giannoni, L., Bonaudo, C., Marradi, M., Della Puppa, A. & Pavone, F. S. Optical characterisation and study of ex vivo glioma tissue for hyperspectral imaging during neurosurgery. in *Diffuse Optical Spectroscopy and Imaging IX* (eds. Contini, D., Hoshi, Y. & O'Sullivan, T. D.) 81 (SPIE, Munich, Germany, 2023). doi:10.1117/12.2670854.

61. Giannoni, L. *et al.* HyperProbe consortium: innovate tumour neurosurgery with innovative photonic solutions. in *Diffuse Optical Spectroscopy and Imaging IX* (eds. Contini, D., Hoshi, Y. & O'Sullivan, T. D.) 47 (SPIE, Munich, Germany, 2023). doi:10.1117/12.2670764.

62. Giannoni, L., Lange, F. & Tachtsidis, I. Hyperspectral imaging solutions for brain tissue metabolic and hemodynamic monitoring: past, current and future developments. *J. Opt.* **20**, 044009 (2018).

63. Caixeiro, S., Wijesinghe, P., Dholakia, K. & Gather, M. C. Snapshot hyperspectral imaging of intracellular lasers. *Opt. Express* **31**, 33175 (2023).
64. Ding, K. *et al.* Snapshot spectral imaging: from spatial-spectral mapping to metasurface-based imaging. *Nanophotonics* **13**, 1303–1330 (2024).
65. Ezhov, I. *et al.* Learnable real-time inference of molecular composition from diffuse spectroscopy of brain tissue. *J. Biomed. Opt.* **29**, (2024).
66. Bale, G., Elwell, C. E. & Tachtsidis, I. From Jöbsis to the present day: a review of clinical near-infrared spectroscopy measurements of cerebral cytochrome-c-oxidase. *J. Biomed. Opt.* **21**, 091307 (2016).
67. The Cancer Genome Atlas Research Network. Comprehensive, Integrative Genomic Analysis of Diffuse Lower-Grade Gliomas. *N. Engl. J. Med.* **372**, 2481–2498 (2015).
68. Motomura, K. *et al.* Clinical characteristics and radiological features of glioblastoma, IDH-wildtype, grade 4 with histologically lower-grade gliomas. *Brain Tumor Pathol.* **40**, 48–55 (2023).
69. Kou, Y., Geng, F. & Guo, D. Lipid Metabolism in Glioblastoma: From De Novo Synthesis to Storage. *Biomedicines* **10**, 1943 (2022).
70. Verdugo, E., Puerto, I. & Medina, M. Á. An update on the molecular biology of glioblastoma, with clinical implications and progress in its treatment. *Cancer Commun.* **42**, 1083–1111 (2022).
71. Persano, L., Rampazzo, E., Della Puppa, A., Pistollato, F. & Basso, G. The Three-Layer Concentric Model of Glioblastoma: Cancer Stem Cells, Microenvironmental Regulation, and Therapeutic Implications. *Sci. World J.* **11**, 1829–1841 (2011).
72. Markwell, S. M., Ross, J. L., Olson, C. L. & Brat, D. J. Necrotic reshaping of the glioma microenvironment drives disease progression. *Acta Neuropathol. (Berl.)* **143**, 291–310 (2022).
73. Monteiro, A., Hill, R., Pilkington, G. & Madureira, P. The Role of Hypoxia in Glioblastoma Invasion. *Cells* **6**, 45 (2017).

74. Domènech, M., Hernández, A., Plaja, A., Martínez-Balibrea, E. & Balañà, C. Hypoxia: The Cornerstone of Glioblastoma. *Int. J. Mol. Sci.* **22**, 12608 (2021).
75. Caldwell, M. *et al.* Modelling Blood Flow and Metabolism in the Preclinical Neonatal Brain during and Following Hypoxic-Ischaemia. *PLOS ONE* **10**, e0140171 (2015).
76. Pogue, B. W. & Patterson, M. S. Review of tissue simulating phantoms for optical spectroscopy, imaging and dosimetry. *J. Biomed. Opt.* **11**, 041102 (2006).
77. Marradi, M. *et al.* Development of a novel, compact, and transportable multispectral imaging device for wound healing monitoring. in *Translational Biophotonics: Diagnostics and Therapeutics III* (eds. Lilge, L. D. & Huang, Z.) 84 (SPIE, Munich, Germany, 2023). doi:10.1117/12.2670869.
78. Bergan, J. J. *et al.* Chronic Venous Disease. *N. Engl. J. Med.* **355**, 488–498 (2006).
79. Armstrong, D. G., Boulton, A. J. M. & Bus, S. A. Diabetic Foot Ulcers and Their Recurrence. *N. Engl. J. Med.* **376**, 2367–2375 (2017).
80. Guest, J. F. *et al.* Health economic burden that different wound types impose on the UK ’s National Health Service. *Int. Wound J.* **14**, 322–330 (2017).
81. Järbrink, K. *et al.* The humanistic and economic burden of chronic wounds: a protocol for a systematic review. *Syst. Rev.* **6**, 15 (2017).
82. Saiko, G. *et al.* Hyperspectral imaging in wound care: A systematic review. *Int. Wound J.* **17**, 1840–1856 (2020).
83. Cao, P. *et al.* Chapter II: Diagnostic Methods. *Eur. J. Vasc. Endovasc. Surg.* **42**, S13–S32 (2011).
84. Leenstra, B. *et al.* Applicability of Transcutaneous Oxygen Tension Measurement in the Assessment of Chronic Limb-Threatening Ischemia. *Angiology* **71**, 208–216 (2020).

85. Aliahmad, B. *et al.* Is Thermal Imaging a Useful Predictor of the Healing Status of Diabetes-Related Foot Ulcers? A Pilot Study. *J. Diabetes Sci. Technol.* **13**, 561–567 (2019).

86. Schuh, S. *et al.* Dynamic optical coherence tomography for imaging acute wound healing. *Int. Wound J.* **21**, e70015 (2024).

87. Ghosh, B., Mandal, M., Mitra, P. & Chatterjee, J. Attenuation CORRECTED-OPTICAL coherence tomography for quantitative assessment of skin wound healing and scar morphology. *J. Biophotonics* **14**, e202000357 (2021).

88. Andersen, C., Reiter, H.-C. J. & Marmolejo, V. L. Redefining Wound Healing Using Near-Infrared Spectroscopy. *Adv. Skin Wound Care* **37**, 243–247 (2024).

89. Gioux, S., Mazhar, A. & Cuccia, D. J. Spatial frequency domain imaging in 2019: principles, applications, and perspectives. *J. Biomed. Opt.* **24**, 1 (2019).

90. Jones, J. D., Ramser, H. E., Woessner, A. E., Veves, A. & Quinn, K. P. Quantifying Age-Related Changes in Skin Wound Metabolism Using *In Vivo* Multiphoton Microscopy. *Adv. Wound Care* **9**, 90–102 (2020).

91. Kelso, M. R. & Jaros, M. Improving Wound Healing and Infection Control in Long-term Care with Bacterial Fluorescence Imaging. *Adv. Skin Wound Care* **37**, 471–479 (2024).

92. Pan, C.-P. *et al.* Wound healing monitoring using near infrared fluorescent fibrinogen. *Biomed. Opt. Express* **1**, 285 (2010).

93. Orkin, R., Sharma, A., John, J. V. & Armstrong, D. G. Current and Future Directions in Fluorescence Imaging-Guided Debridement. *Adv. Wound Care* wound.2024.0067 (2024) doi:10.1089/wound.2024.0067.

94. Li, H., Li, G., Ye, Y. & Lin, L. A high-efficiency acquisition method of LED-multispectral images based on frequency-division modulation and RGB camera. *Opt. Commun.* **480**, 126492 (2021).

95. Gorpas, D., Wabnitz, H. & Pfefer, T. J. Special Section Guest Editorial: Tissue Phantoms to Advance Biomedical Optical Systems. *J. Biomed. Opt.* **27**, (2022).
96. Van Gemert, M. J. C., Jacques, S. L., Sterenborg, H. J. C. M. & Star, W. M. Skin optics. *IEEE Trans. Biomed. Eng.* **36**, 1146–1154 (1989).
97. Meglinsky, I. V. & Matcher, S. J. Modelling the sampling volume for skin blood oxygenation measurements. *Med. Biol. Eng. Comput.* **39**, 44–50 (2001).